UNIVERSITY OF MARYLAND

Technical Note BN-582 December 1968

Single-Electron Capture by Multiply-Charged Carbon Ions at Energies below 40 kev†

by

H. Jay Zwally

University of Maryland
College Park, Maryland

THE INSTITUTE FOR FLUID DYNAMICS *and* APPLIED MATHEMATICS

Technical Note BN-582 December 1968

Single-Electron Capture by Multiply-Charged Carbon Ions at Energies below 40 kev[†]

by

H. Jay Zwally

University of Maryland

College Park, Maryland

[†]Research supported by the National Aeronautics and Space Administration Grant NsG-283, the National Science Foundation Grant NSF GP-8325, and the Board of Regents of the University of Maryland.

ABSTRACT

Title of Thesis: Single-Electron Capture by Multiply-Charged Carbon Ions at Energies below 40 kev.

H. Jay Zwally, Doctor of Philosophy, 1968

Thesis Directed by: Research Associate Professor, David W. Koopman

Total cross sections for single-electron capture by C^{4+} from the target gases of He, Ne and Ar have been measured at laboratory energies below 40 kev. The relative velocities of collision were in the "near adiabatic" range of $1 - 8 \times 10^7$ cm/sec. Cross sections have also been measured for C^{2+} on He, Ne , and Ar and Kr^{3+} on He . The experimental method was to pass an ion beam through a thin gas target under single collision conditions and to separate and measure the fast collision products according to their charge state.

The results are interpreted in terms of the pseudo-crossing of the adiabatic potential energy curves for the initial and the final states. A comparison is made with a cross-section function, σ^{LZ} , derived from the limited Landau-Zener theory using an empirical value of the interaction matrix element that is based on previous theoretical and experimental results. Possible contributions to the cross sections caused by transitions that occur away from the pseudo-crossing region as described by the numerical solution of the two-state, semi-classical approximation by Bates, Johnson and Stewart are also considered. The

measured cross sections for $C^{4+} + He$, $C^{4+} + Ne$, and $C^{2+} + Ne$ increase toward a possible "second maximum" at much higher velocities than those at which the σ^{LZ} function is a maximum; the increase occurs at successively higher velocities for processes with pseudo-crossings at successively larger values of the internuclear separation. These characteristics are consistent with the BJS calculated results which give a second maximum for the process $Mg^{2+} + H$ that also has a distant crossing point. Electron capture with an Auger-type ionization of the target is energetically possible for $C^{4+} + Ne$ and $C^{4+} + Ar$ and is considered as an explanation of the large and slowly varying cross section that is measured for $C^{4+} + Ar$.

The C^{4+} ion was produced in a pulsed-discharge ion source that is similar to the washer-type hydrogen plasma gun in design. The pulsed-discharge ion source, an ion beam apparatus with a double-focusing mass spectrometer, and a system for ion detection and signal recording have been developed to enable the measurement of the cross sections for C^{4+} ions, which were previously inaccessible for beam-type collision measurements.

ACKNOWLEDGEMENTS

I express my appreciation to my thesis advisor Dr. D. W. Koopman for his helpful advice and guidance during the course of this research program and to Dr. T. D. Wilkerson for advice, encouragement and financial support. In particular, Dr. Wilkerson suggested using the pulsed plasma source as an ion source for collision measurements. I also thank Dr. P. G. Cable and Dr. K. W. Ogilvie for many helpful discussions during the initial stages of this research.

The staff of the shop under Mr. E. Grossenbacher are gratefully acknowledged for their craftsmanship and perseverance in fabricating the many stainless steel components of the appartus. Invaluable suggestions about the design of the precision parts were made by Mr. E. Grossenbacher.

My thanks are expressed to Mrs. M. Mills for her skilled typing and to my wife Jo Ann for her editorial assistance. Special appreciation is due Jo Ann for her patience and encouragement during the many years of my graduate work.

During the course of this work I was the recipient of a NASA Traineeship for which I am very grateful.

This research was supported primarily by the Office of Space Sciences and Applications of the National Aeronautics and Space Administration under Grant NsG-283 monitored by Dr. Albert Opp, and by the National Science Foundation Grant NSF GP-8325. Special equipment was provided through grants from the Board of Regents of the University of Maryland.

TABLE OF CONTENTS

CHAPTER I

INTRODUCTION

Studies of binary atomic collision processes have been motivated by two factors: their inherent interest as physical processes and their importance as part of other physical phenomena.[1] The basic force in atomic collisions at relatively low velocities is due to the electrostatic interaction of charged particles, and nuclear interactions are negligible. Although the motions of point charges in binary collisions can be described, atomic collisions are complicated because the colliding atoms are actually systems of charged particles. Therefore, the problem is not a two-body problem and approximations must be made to a complete, quantum-mechanical description.

The specific process studied in this experiment is the exchange of an electron between colliding atomic systems, from a neutral target-atom to a multiply-charged atom of a different element. This process of electron capture is in the general class of rearrangement collisions which involve an exchange of particles. Energy and momentum can also, in general, be transferred. If there is also a conversion of internal potential energy to kinetic energy of relative motion (or vice-versa), then the collision is inelastic.

Collisions of heavy particles at low velocities can be described in terms of the adiabatic potential-energy curves of the quasi-molecule formed by the colliding atoms, as a function of inter-nuclear separation (R). The criterion for low velocities is that the velocity of relative approach be small compared to the orbital

velocity of the internal electron motion (of order 10^8 cm/sec); but also large enough ($> 10^5/(\text{reduced mass})^{\frac{1}{2}}$ cm/sec)^2 so that motion of the atomic centers is essentially classical. This region of velocities is usually termed "near-adiabatic" (cf. Ref. 3,4). Single-electron capture collisions between multiply-charged ions and neutral atoms are interesting because they illustrate a class of processes that occur at low velocities as a result of a pseudo-crossing of the adiabatic potential curves.

In the following chapters a review of some of the applicable theory, a description of the pulsed-discharge ion source and other apparatus, a description of the experimental methods, and the graphs of the experimental data and the interpretation of the results are presented.

A. Multiply-Charged Ion-Atom Collisions

The typical process that is considered is single-electron capture of multiply-charged ions from neutral atoms,

$$A^{z+} + B \rightarrow A^{(z-1)+} + B^{+} + \Delta E \qquad (1.A.1)$$

where ΔE is the difference between the potential energy of the initial and final configurations at large R. The electrons surrounding the nucleus of each ion or atom are in one of the many bound energy levels. As the ion approaches the atom, the combined system becomes quasi-molecular in nature and the positions of the various levels

continuously change. Radiationless transitions of electrons between levels become possible.

A basic assumption in theoretical treatments of atomic collisions at low velocities is that the electronic motion and the relative motion of the atomic centers can be separated, and that the motion of the atomic centers can be classically described. If the atoms approach adiabatically from infinity, then the potential energy of a given state of the quasi-molecule can be defined as a function of internuclear separation, R . This potential energy as a function of R is termed the adiabatic potential.[5] Theoretical treatments of atomic collisions in this near-adiabatic range of velocities are given in references (eg. 2, 4, 6).

The probability of an ultimate transition between states depends on the duration of the collision. At each fixed internuclear separation, R , there is a mixing of initial and final states; the amount of mixing is dependent on the energy difference of the states. During a collision this mixing is effectively turned on and off as a function of time, and there is some probability that the final state will be different than the initial state. Time-dependent perturbation theory can be used in some approximations to determine the coefficients of the final states after the collision $(t = +\infty)$.

The energy definition of a given state can be approximately related to the time interval (Δt) of the encounter by the uncertainty principle $(\Delta E_u \sim \hbar/\Delta t)$. Thus, it can be seen that for short

collision times, states that are separated by approximately the uncertainty ΔE_u overlap, and ultimate transitions are possible. The well-known "adiabatic criterion" of Massey[3] and subsequent applications of it by Hasted et al (cf. Ref. 7) to collisions where the energy separation, ΔE, between the initial and final states is approximately constant during the collision, indicates a maximum of the cross section for the transition at the velocity

$$v_m \approx \ell \Delta E/\hbar \qquad (1.A.2a)$$

$$v_m(10^7 \text{ cm/sec}) \approx .13\, \ell(a_o)\Delta E(\text{ev}) \qquad (1.A.2b)$$

where ℓ is the estimated length of the encounter.

Equation (1.A.2) can be derived[8] from the Born approximation and applies for the condition that ΔE is a small fraction of the bound energy of the electron in its initial state; if ΔE is of order this bound energy, then $v_m \propto \Delta E^{\frac{1}{2}}$ (Ref. 8). For the multiply-charged ion collision Eq. (1.A.1) it is well-known that Eq. (1.A.2) is not directly applicable[3,7], since ΔE is a strong function of R as discussed in the following paragraphs. However, the Landau-Zener formula (discussed below) for the probability of a transition for the exothermic case of Eq. (1.A.1) can be shown[9] to be equivalent to Eq. (1.A.2), if an average of ΔE in the crossing region (defined below) and the estimated length of the crossing region for the value of ℓ are used.

The adiabatic condition, Eq. (1.A.2), must be used with caution; it is only a qualitative formula for estimating the velocity region where transitions may occur between levels that are closely spaced during all or part of the collision.

Returning to a general consideration of the process given in Eq. (1.A.1), we note that all three of the following complications must be considered for multiply-charged ions: 1) for most systems, there is more than one possible pair of initial and final states with a corresponding ΔE; 2) in multi-electron systems, two or more electrons might together undergo a transition; 3) ΔE is a strong function of internuclear separation, R, as a result of the Coulomb potential energy term between the final ions. The latter is the essential difference between multiply-charged and singly-charged ion-atom collisions.

Restricting consideration at this point to the exchange of one electron between only one possible pair of states, one initial state and one final state, the system can then be described by two adiabatic, inter-atomic, potential energy curves. Typical, initial and final curves for process (1.A.1), for the exothermic case ($\Delta E > 0$), are shown in Fig. 1.A.1. The final potential curve decreases approximately as $1/R$ due to the Coulomb repulsion between the final ions, and it is lower than the initial curve by the exothermic energy detect. These curves would classically cross each other at R_x (hereafter called the crossing point). However, as a result of quantum-mechanical effects, adiabatic potential curves of the same symmetry cannot cross, as stated by von Neumann and Wigner[10]. Therefore, the

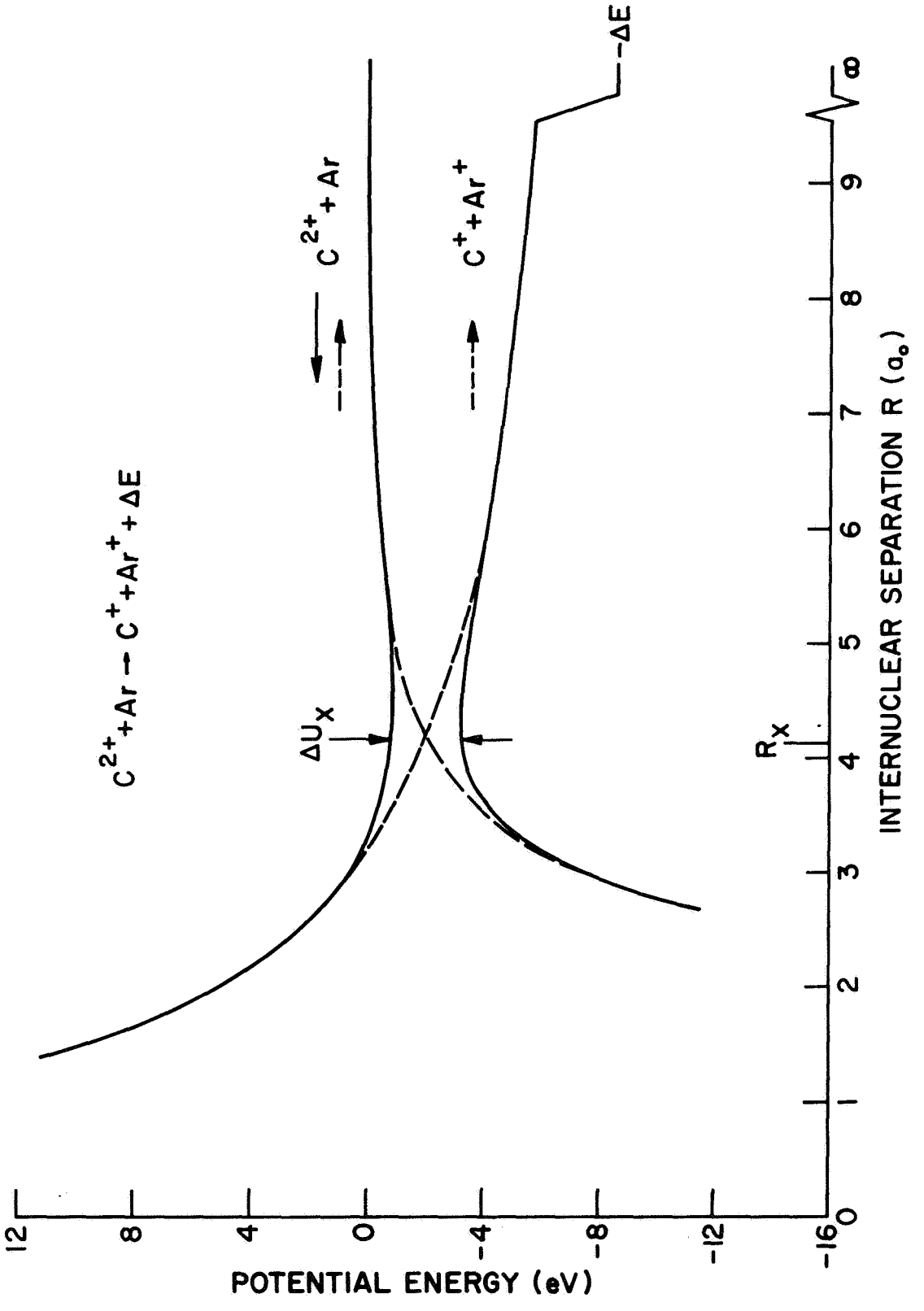

Fig. 1.A.1. Initial and Final Adiabatic Potential Energy Curves. (showing pseudo-crossing point, for C^{2+} + Argon).

curves in this adiabatic representation do not cross, but have a minimum separation near the crossing point due to the interaction of the two states.

The probability of a transition between states in the region of the crossing point due to the interaction or mixing of the initial and the final states was first considered by Stueckelberg[11], Landau[12], and Zener[5]. Their methods of derivation are not the same, but basically they use a semiclassical approximation and a two-state approximation; Landau and Zener use time-dependent perturbation theory. The formula for the probability of an ultimate transition is called the Landau-Zener (LZ) formula, and its derivation and limitations are reviewed in chapter 2A. Its use as an empirical formula with limited value as a qualitative guide is discussed in Chapter 2B. An improved treatment that also includes transitions outside of the region of the crossing point has been made by Bates, Johnson, and Stewart[13] and is reviewed in chapter 2C.

Although the precise characteristics of the cross sections for single-electron capture in multiply-charged ion-atom collisions in the near-adiabatic region of velocities are uncertain, some features can be noted: 1) if the process is endothermic ($\Delta E < 0$), the curves become more widely separated at moderate internuclear separations and transitions are unlikely to occur; 2) if the energy defect is very small ($\Delta E \sim 0$), the process would be near resonant if ΔE were not a function of internuclear separation, but again transitions are unlikely to occur; 3) if the process is exothermic ($\Delta E > 0$), there is a crossing point, and for some values of R_x the transition

probability is quite large, giving cross sections of order $1 - 40\ A^{\circ 2}$ at relatively low velocities of order 10^7 cm/sec.

B. Experimental Measurements of Electron Capture of Multiply-Charged Ions

The general process to be considered for the collision of a multiply-charged ion with a neutral target atom is described by

$$A^{z+} + B \rightarrow A^{(z+s-c)} + B^{(i+c)} + (i + s)e + \Delta E \qquad (1.B.1)$$

where $z \geq 2$, and

z = No. of charges on projectile ion initially

c = No. of electrons captured by projectile

s = No. of electrons stripped from projectile

i = No. of electrons from ionization of target

Also, the ions can in general be in excited states. A complete measurement of all the possible combinations would require coincidence detection of all final particles and a determination of the electronic state of all particles. Other parameters to be measured for a complete description are the angular scatter and the energy of the final particles as a function of the initial relative velocity. Usually, an assumption about which specific process (sub-class of 1.B.1) is most probable, in a particular range of velocity, can be made and tested to reduce the parameters to a reasonable number. In most collision

experiments either the fast collision products (projectile) are analyzed and measured, or the slow collision products (target) and electrons are analyzed and measured. For a review of these two basic methods see reference 14.

The measurements of cross sections for electron-capture of multiply-charged ions in this experiment have been made under single-collision conditions so that cascade processes are negligible. The basic technique (cf. Chap. 4) is similar to that of Flaks and Filippenko,[15] for example. The projectile ions are separated according to charge state after collision. The total cross section for single-electron capture ($c = 1$) that is measured is

$$\sigma_{z,z-1} \propto \frac{\text{Intensity of } A^{(z-1)+}}{\text{Incident intensity of } A^{z+}} \qquad (1.B.2)$$

In addition to the single-electron process of single-electron capture, the measured cross section includes contributions, if any, from the two-electron processes of single-electron capture with target excitation and single-electron capture with target ionization. The stripping process is not included in the measured cross section, nor is the process of multiple-electron capture. The laboratory energy range of the incident ions in this experiment is approximately 100 ev to 10 Kev per unit charge (z) ; for Carbon (4+) the relative velocity range is $1.5 - 8 \times 10^7$ cm/sec. This velocity range is within, and extends close to, the upper limit of the "near-adiabatic" range of velocities.

Previous experimental studies of multiply-charged ions have been made with ions (e.g. C^{2+}, Ar^{3+}, Kr^{4+}, Xe^{4+}) that can be

produced in an electron-impact type of ion source. Some of these studies (16, 17, 18) have been directed toward investigation of processes due to curve crossing. The gases that are stable and monoatomic are the inert gases, and the target atoms used in previous experiments and this experiment have been limited to Helium, Neon, Argon, Krypton and Xenon; crossed-beam experiments using multiply charged ions and unstable species such as atomic hydrogen have not been performed.

In the present experiment, ions are extracted from the hot plasma of a pulsed, washer-type plasma gun. Graphite electrodes are used, and Carbon ions up to $z = 4$ have been produced in sufficient quantity for a collision experiment. Cross sections for single-electron capture have been measured for Carbon (4+) on Helium, Neon and Argon. Additional ions of other light elements, that are difficult to ionize or obtain in gaseous form, can probably be produced and studied by adaptation of the techniques used in the experiment.

CHAPTER II

THEORETICAL BACKGROUND

A discussion of theory that is applicable to the electron-capture processes described in Chap. 1.A is given in this chapter as a basis for understanding the experimental results. The derivation of the Landau-Zener (L - Z) formula, which is based on the two-state, semi-classical approximation, and the limitations of this formula, as discussed by Bates[19], are reviewed in Sec. A. The experimental and theoretical applications of the L - Z formula to specific systems are reviewed in Sec. B. An empirical cross-section function, σ^{LZ}, is defined in terms of previous theoretical and experimental results; this treatment will serve as a rough qualitative guide for estimating the cross-section function that is expected on the basis of the L - Z theory.

An improved treatment of the two-state, semi-classical approximation with a numerical solution of the coupled equations by Bates, Johnson, and Stewart[13] (BJS) is discussed in Sec. C. Of particular importance to this experiment is their prediction of a second maximum in cross-sections for interactions which have a curve-crossing point at large inter-nuclear separations. Collisions involving a change of state of two electrons are discussed in Sec. D.

A. Landau-Zener Approximation

Consider the transfer of an electron from the state n of an atomic system A to the state m of an atomic system B.

$$(A + e)_n + B \rightarrow A + (B + e)_m \qquad (2.A.1)$$

The basic assumptions to be made are that the motion of the nuclei can be classically described and that there are only two states (n and m) of internal motion. The details of the various derivations can be obtained by reference to Bates,[19] Mott and Massey[9] and the original papers[11,12,5] of Stueckelberg, Landau and Zener. Other similar treatments and discussions are in the literature, for example Refs. 20-23.

A review of the basic features of the derivation of the L - Z formula as given by Bates[19] is presented here. A basic assumption is that the velocity of relative approach is slow enough to permit the description of the system by adiabatic potential energy curves. The L - Z formula was derived for systems where, in the zero-order approximation of the wave functions, the initial curve crosses the final curve. In higher order, the interaction of the initial state with the final state is considered as a perturbation which makes the transition between the states possible.

Time-dependent perturbation theory is used to derive coupled differential equations for the amplitudes of each state. The exact electronic eigenfunctions for the respective quasi-molecular states are denoted as $\psi_n(\underline{r}|\underline{R})$ and $\psi_m(\underline{r}|\underline{R})$, where $\underline{r}$ is the position vector of the active electron with respect to the mid-point of the two nuclei, and the relative nuclear coordinate $\underline{R}$ is a parameter. The respective eigenenergies are $E_n(\underline{R})$ and $E_m(\underline{R})$ and depend only on $\underline{R}$. As a crossing region is traversed, the eigenfunctions $\psi_n(\underline{r}|\underline{R})$ and $\psi_m(\underline{r}|\underline{R})$ interchange their forms and the systems they describe (cf. Fig. 2.A.1).

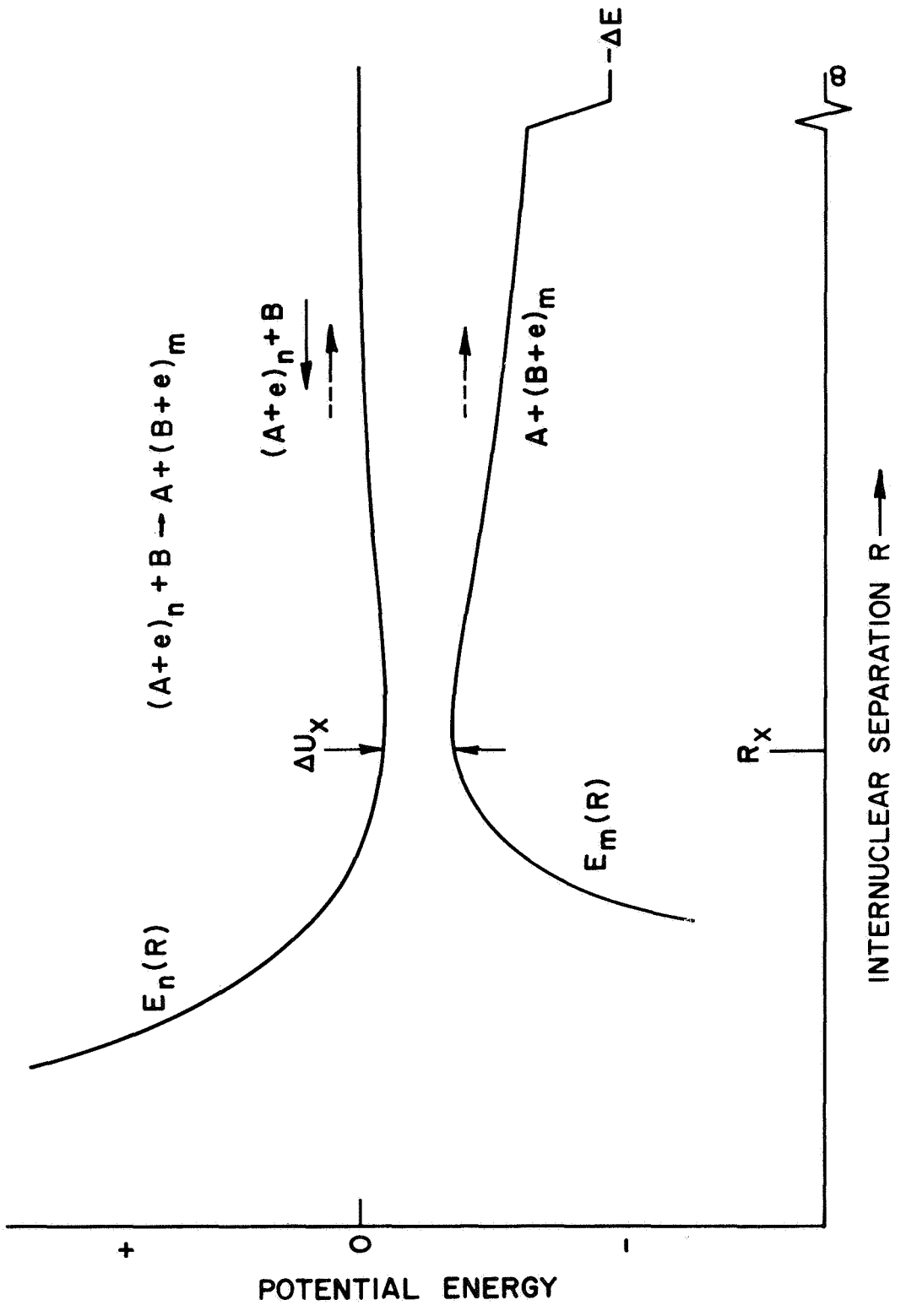

Fig. 2.A.1. Adiabatic Potential Energy Curves.
(Eigenenergies of $\psi_n(r|R)$ and $\psi_m(r|R)$) .

New functions $\phi_n(\underline{r}|\underline{R})$ and $\phi_m(\underline{r}|\underline{R})$ are defined as orthogonal linear combinations of $\psi_n(\underline{r}|\underline{R})$ and $\psi_m(\underline{r}|\underline{R})$ so that they do not change form as R changes and will describe respectively the left and right side of Eq. 2.A.1 for <u>all</u> internuclear distances, R.

The relative velocity, $\underline{v}$, of the nuclei is assumed to be constant and equal to its value at the crossing point and

$$z \equiv \underline{R}\cdot\hat{v} = vt \ . \tag{2.A.2}$$

where $\hat{v}$ is the unit vector and v is the radial component of $\bar{v}$ at R_x. A perturbation calculation gives the differential equations for the respective amplitudes $c_n(z)$ and $c_m(z)$ for the states $\phi_n(\underline{r}|\underline{R})$ and $\phi_m(\underline{r}|\underline{R})$. <u>These amplitudes are functions of the impact parameter as well as the time</u>. The results are

$$i\hbar v \frac{\partial c_n(z)}{\partial z} = h_{nm}(R)\ c_m(z)\ \exp\left\{-\frac{i}{\hbar v}\int^z (h_{mm}(R) - h_{nn}(R))dz\right\} \tag{2.A.3}$$

and

$$i\hbar v \frac{\partial c_m(z)}{\partial z} = h_{mn}(R)\ c_n(z) \exp\left\{\frac{i}{\hbar v}\int^z (h_{mm}(R) - h_{nn}(R))dz\right\} \tag{2.A.4}$$

where

$$h_{nm} = \int \phi_n^*(\underline{r}|\underline{R}) H \phi_m(\underline{r}|\underline{R})d\underline{r} \tag{2.A.5}$$

and H is the Hamiltonian. The crossing distance, R_x, is by definition the point where the curves $h_{nn}(R)$ and $h_{mm}(R)$ cross (cf. Fig. 2.A.2).

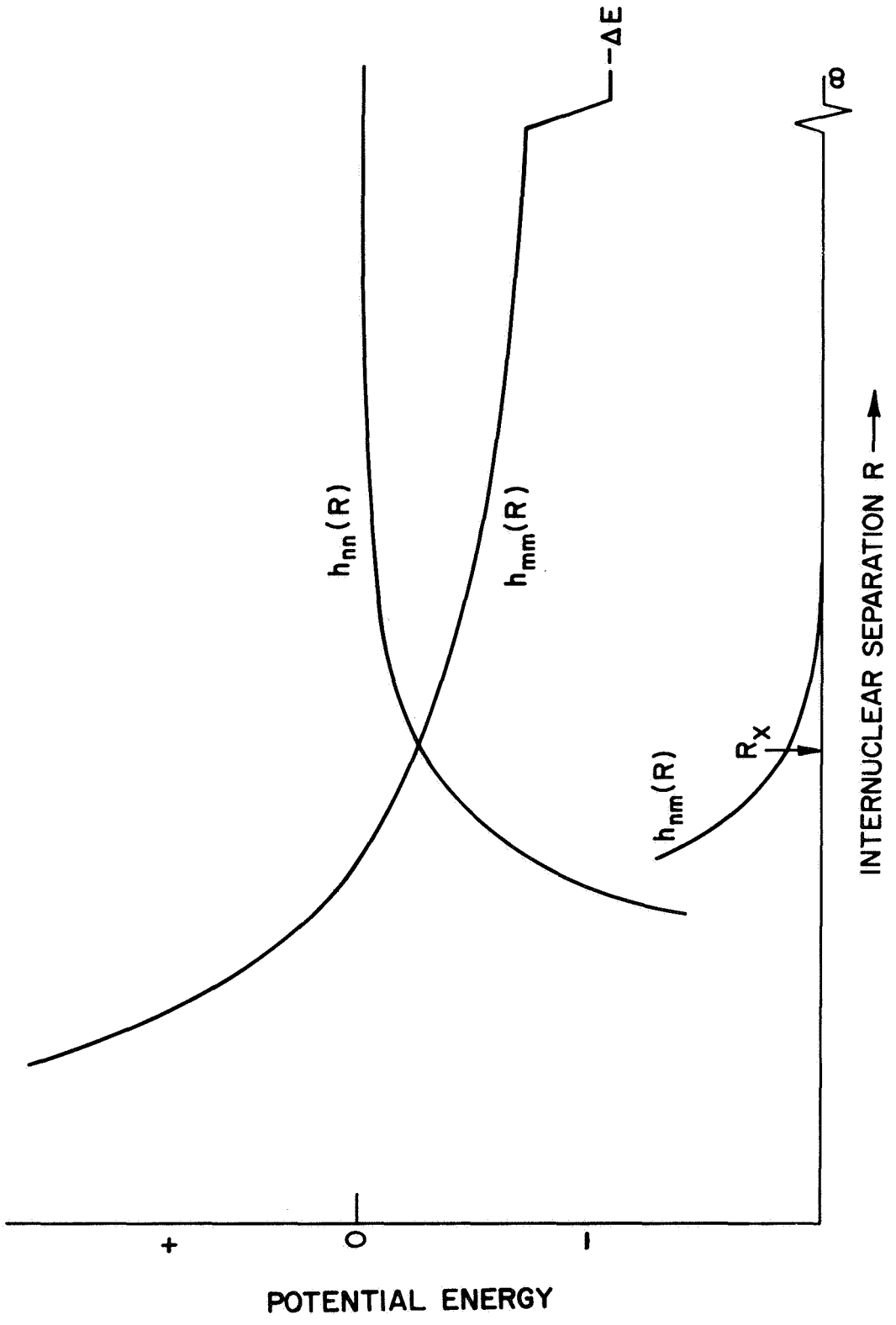

Fig. 2.A.2. Matrix Elements between $\phi_n(r|R)$ and $\phi_m(r|R)$.

The boundary conditions are

$$|c_n(-\infty)|^2 = 1 \quad \text{and} \quad |c_m(-\infty)|^2 = 0 \ . \tag{2.A.6}$$

In order to solve (2.A.3) and (2.A.4) analytically, a model must be introduced. One such model is that of Landau and Zener. It is assumed that the probability of a transition occurring is appreciable only in a very narrow region near the crossing point. The matrix elements are then assumed to be

$$h_{nm}(z) = h_{mn}(z) = \frac{1}{2}\,\Delta U(R_x) = \text{constant} \tag{2.A.7}$$

and

$$h_{nn}(z) - h_{mm}(z) = \alpha(z - z_x) \ ; \quad \alpha = \text{constant}. \tag{2.A.8}$$

The asymptotic amplitudes of the solutions can then be obtained. The probability, P, that for a single transit of the crossing point the system will remain in state n (i.e. remain on $h_{nn}(R)$ or equivalently jump from $E_n(R)$ to $E_m(R)$, see Figs. 2.A.1 and 2.A.2) is

$$P = |c_n(\infty)|^2 = e^{-w} \tag{2.A.9}$$

where

$$w = \frac{2\pi}{\hbar} \left[\frac{h_{nm}^2(z)}{v(h'_{nn}(z) - h'_{mm}(z))} \right]_{z=z_x} \tag{2.A.10}$$

and

$$1 - P = |c_m(\infty)|^2 \ . \tag{2.A.11}$$

The total probability of an ultimate transition from $n \rightarrow m$ (subscript 1 indicates the ingoing transit and 2 the outgoing transit) is

$$P_{nm} = P[n \rightarrow n]_1 \, P[n \rightarrow m]_2 + P[n \rightarrow m]_1 \, P[m \rightarrow m]_2 = P(1 - P) + (1 - P)P$$

or

$$P_{nm} = 2P(1 - P) \ . \tag{2.A.12}$$

Equation (2.A.12) is called the Landau-Zener formula.

In order to obtain a cross section as a function of the relative velocity of motion the transition probability, P_{nm}, must be integrated over the impact parameter. P_{nm} has an implicit dependence on the impact parameter, ρ, because the value of v in Eq. 2.A.10 is the radial component of the relative velocity at the crossing point.[24] Therefore, v is a function of R_x and of the relative velocity, V_{REL}, at infinite separation. The cross section is then

$$\sigma_{nm}(v_{REL}) = 2\pi \int_0^{R_x} P_{nm}(\rho, R_x, v_{REL}, \text{ Matrix elements}) \rho d\rho \ . \tag{2.A.13}$$

The limitations of the L - Z formula, as discussed by Bates, are of two types, those which are due to assumptions imposed to derive Eqs. (2.A.3) and (2.A.4) and those which are imposed by the model that is chosen to solve these equations. Discussing first the limitations inherent to equations (2.A.3) and (2.A.4), a lower limit of applicability is imposed by the assumption that the energy of relative motion be

$$E_r >> 2|h_{nm}| \quad . \tag{2.A.14}$$

This is not very restrictive, since usually $h_{nm} < 5$ ev and is very small if R_x is large. An upper limit is imposed by ignoring the effects of the change in the translational motion of the active electron when it is transferred between systems. According to Bates this is unjustified for

$$E_r \gtrsim 25\ M/\ell^2 \quad \text{k ev} \tag{2.A.15}$$

where M is the reduced mass and ℓ (atomic units) is a measure of the linear extent of the more compact of the two eigenfunctions. The most severe limitation arises if the eigenfunctions ϕ_n and ϕ_m are not spherically symmetric. This restricts the applicability to $s - s$ transitions. Otherwise, for example, if the inital electron state is a p state and the final state is an s state, additional rotational terms must be considered. Bates states that these terms cannot be neglected at high velocities, but that the velocity above which serious error occurs is difficult to estimate. As will be seen in section C, most of the transitions that have been experimentally studied and to which the $L - Z$ formula has been applied are not $s - s$ transitions.

The other limitations are due to the L - Z model that is chosen for the matrix elements. The basic assumption of this model that transitions only occur near the crossing is contradicted because the oscillations of the exponential functions in (2.A.3) and (2.A.4) are not sufficiently rapid away from the region of the crossing point to produce cancellation. Bates gives an expression for the width of the transition zone in which the oscillations do not cancel as

$$\Delta z \approx \left(\frac{4\pi h}{\alpha}\right)^{\frac{1}{2}} v^{\frac{1}{2}} \quad .$$

Bates estimates that the transition zone can be of order R_x even at relatively low velocities. If the transition zone is quite wide, the choice of a constant interaction energy $h_{nm}(R_x)$ is not justified.

Bates presents two qualitative corrections to the probability vs. velocity curve. One is the shift of the normal peak to higher velocities, which appears to be inconsistant with his more recent results (cf. Sec. C). The other is the prediction of a second maximum at higher velocities for crossings at large separations for which the first maximum is at very low velocities.

B. Empirical Use of Landau-Zener Formula

From the L - Z formula (Eq. 2.A.12), Bates and Moiseiwitsch deduce the following expression for the cross section for the process (1.A.1) :

$$\sigma = 4\pi R_x^2 \, I(\eta) \, \{(1 + \lambda)p\} \tag{2.B.1}$$

where

$$I(\eta) = \int_1^\infty \exp(-\eta x) \, \{1 - \exp(-\eta x)\} \, x^{-3} dx \tag{2.B.2}$$

and

$$\eta = 247.2 \left\{\frac{\sqrt{2}}{v_{REL}}\right\} \left\{\frac{\Delta U_x}{\Delta E}\right\}^2 \frac{(Z - 1)}{(1 + \mu)(1 + \lambda)^{\frac{1}{2}}} \tag{2.B.3}$$

and p is the probability that the particles approach along the specified potential energy curve ($p = 1$ for process 1.A.1), v_{REL} is the velocity of relative motion, ΔE is the energy defect (equal to the separation of the curves at $R = \infty$), ΔU_x is the separation of the curves at the crossing point and

$$\Delta U_x = 2\left|h_{nm}(R_x)\right| \quad . \tag{2.B.4}$$

The terms λ and μ are usually small compared to unity and are given by

$$\lambda = \{U_i(\infty) - U_i(R_x)\}/E_{REL} \tag{2.B.5}$$

and

$$(1 + \mu) = \frac{(Z - 1)e^2}{\Delta E^2} \left| \frac{d}{dR} \ (U_i^\circ - U_f^\circ) \right|_{R_x} \tag{2.B.6}$$

where the initial and final, adiabatic potential curves are denoted by $U_i(R)$ and $U_f(R)$, and a zero superscript denotes the pseudo-crossing, non-interacting curves. The integral, $I(\eta)$, has been calculated[25] and has a maximum value of .113 at $\eta = .424$. We also note that the relative velocity is

$$v_{REL} = \left\{\frac{2E_{REL}}{M}\right\}^{\frac{1}{2}} = \left\{\frac{2E_{LAB}}{M_A}\right\}^{\frac{1}{2}} \tag{2.B.7}$$

where M is the reduced mass, E_{REL} is the energy of relative motion, M_A is the projectile mass and E_{LAB} is the laboratory energy.

A value of R_x can be obtained by calculating the intersection of the approximate, pseudo-crossing potential energy curves which include terms representing the polarizability interaction and the final Coulomb repulsion. The implicit equation for R_x is

$$e^2 \left\{\frac{(Z - 1)}{R_x} + \frac{A}{R_x^4}\right\} = \Delta E \tag{2.B.8}$$

where

$$A \equiv \frac{1}{2} \{Z^2\alpha(B) - (Z - 1)^2\alpha(B^+) - \alpha(A^{(Z-1)+})\} \tag{2.B.9}$$

and the α's are the polarizabilities. Also, substitution of the potential terms in (2.B.5) and (2.B.6) yields

$$\lambda = \frac{e^2}{E_{REL}} \left\{ \frac{A}{R_x^4} \right\} \qquad (2.B.\ 10)$$

and

$$(1 + \mu) = \frac{e^4(Z - 1)}{\Delta E^2} \left\{ \frac{(Z - 1)}{R_x^2} + \frac{4A}{R_x^5} \right\} \quad . \qquad (2.B.11)$$

If the polarization terms in the potentials are neglected, then both μ and λ equal zero.

The L - Z cross section for a given energy defect, ΔE, and given Z is a function of three variables by Eqs. 2.B.1 through 2.B.10 i.e.

$$\sigma = \sigma(R_x, \Delta U_x, v_{REL}) \qquad (2.B.11)$$

The value of R_x is calculated as described in the previous paragraph; v_{REL} remains as a parameter; ΔU_x must be calculated from the matrix elements using the appropriate wave functions (cf. Egs. 2.A.5 and 2.B.4). The maximum value of the cross section (assuming $\lambda = 0$) occurs at $I(.424) = .113$ and is determined by the value of R_x, i.e.

$$\sigma_{max}^{LZ} = .45\ \pi R_x^2 \qquad (2.B.12)$$

The velocity (or energy) corresponding to a particular value (e.g. the maximum value) of the cross section is determined by Eq. 2.B.3 which is

$$\eta = \eta(R_x, \Delta U_x, v_{REL}) \tag{2.B.13}$$

For given values of ΔE and Z, and since R_x enters only in the small terms, λ and μ, we have approximately

$$\eta \propto \frac{\Delta U_x^2}{v_{REL}} \propto \frac{\Delta U_x^2}{E_{REL}^{1/2}} \tag{2.B.14}$$

which shows that η is a much more sensitive function of ΔU_x than of v_{REL} or E_{REL}. In fact, for a fixed value of η (e.g. $\eta = .113$)

$$\frac{\Delta(E_{REL})}{E_{REL}} = 2\,\frac{\Delta(v_{REL})}{v_{REL}} = 4\,\frac{\Delta(\Delta U_x)}{\Delta U_x} \tag{2.B.15}$$

Hence, the velocity and the energy corresponding to a particular value (e.g. the maximum value) of the cross section are very sensitive to the value of ΔU_x; a fractional shift in ΔU_x produces twice that shift in v_{REL} and four times that shift in E_{REL}. This sensitivity was noted by Bates and Moiseiwitsch[24] who also noted that the L - Z theory should therefore be more reliable for determining the magnitude of the cross section than for determining the energy position of the maximum of the cross section.

Equations for the energy and the velocity at which the L - Z cross section is a maximum are included for reference.

$$E_{LAB}^{max} = 34.0 \times 10^3\ (Z - 1)^2 (M_A) \left(\frac{\Delta U_x}{\Delta E}\right)^4 (1 + \mu)^{-2} \quad (ev) \tag{2.B.16}$$

and

$$v_{REL}^{max} = 81.0\ (Z - 1)\left(\frac{\Delta U_x}{\Delta E}\right)^2\ (1 + \mu)^{-1}\quad (10^7\ \text{cm/sec}) \tag{2.B.17}$$

(The $(1 + \lambda)$ term was dropped since $\lambda(E_R) << 1$ at energies above several hundred ev).

The following methods of comparison of theory with experiment are noted by Hasted, Lee, and Hussain:

1. Comparison of the form of the experimental cross section function with $I(\eta)$ normalized at the maximum of the cross section.

2. Comparison of the maximum value of the experimental cross section with Eq. 2.B.12.

3. Calculation of the value of ΔU_x from Eq. 2.B.3 using $\eta = .424$ and the relative velocity for which the experimental cross section is a maximum; comparison of these ΔU_x values for several collision processes as a function of other collision parameters, such as R_x.

4. Comparison of the values of ΔU_x calculated as in method 3 with values of ΔU_x from a quantum mechanical calculation of the matrix element, h_{nm}.

A number of quantum mechanical calculations of ΔU_x were made[24,27,28] for relative simple atomic systems composed of either an atomic hydrogen or a helium target and projectiles of various multiply-charged light elements. Calculations of ΔU_x were also made[29,30] for simple ionic recombination between H^- ions and various positive ions. These calculated ΔU_x appeared to be primarily a function of R_x[28,30].

A number of experimental values of ΔU_x were obtained as in method 3 above by Hasted and Chong from their experimental data and from previous data of Hasted and Smith[31]. These theoretical values of ΔU_x and the experimental values of ΔU_x were plotted[16] as a function of R_x with a smooth curve drawn through the points. The values of ΔU_x range from 2.3×10^{-8} ev at $R_x = 20.2\ a_o$ for one process[28] to 5.2 ev at $R_x = 3.3\ a_o$ for another process[27]. There is a considerable scatter of both the theoretical and the experimental points around the smooth curve. There has been some attempt to relate the deviations from the curve to other factors,such as the atomic number of the target[30].

Some more approximate, quantum mechanical calculations of ΔU_x were made[17,26,18] for more complex atomic systems, such as $Kr^{3+} + He$, for which experimental measurements of the cross sections were also made (same refs.). The method of comparison is as described in method 4 and is a direct comparison of the experimental and the theoretical ΔU_x for each process. Some values agree well, but there are also large differences[18].

If the value of ΔU_x were only a function of R_x, it would be possible on the basis of the empirical curve of ΔU_x vs. R_x and the L - Z formula to predict a cross section function for a process from the value of the crossing point, R_x. As discussed previously the <u>magnitude</u> of the predicted cross section would be more accurate than its <u>velocity position</u>. The scatter of the ΔU_x points about the smooth empirical curve varies from several factors for some

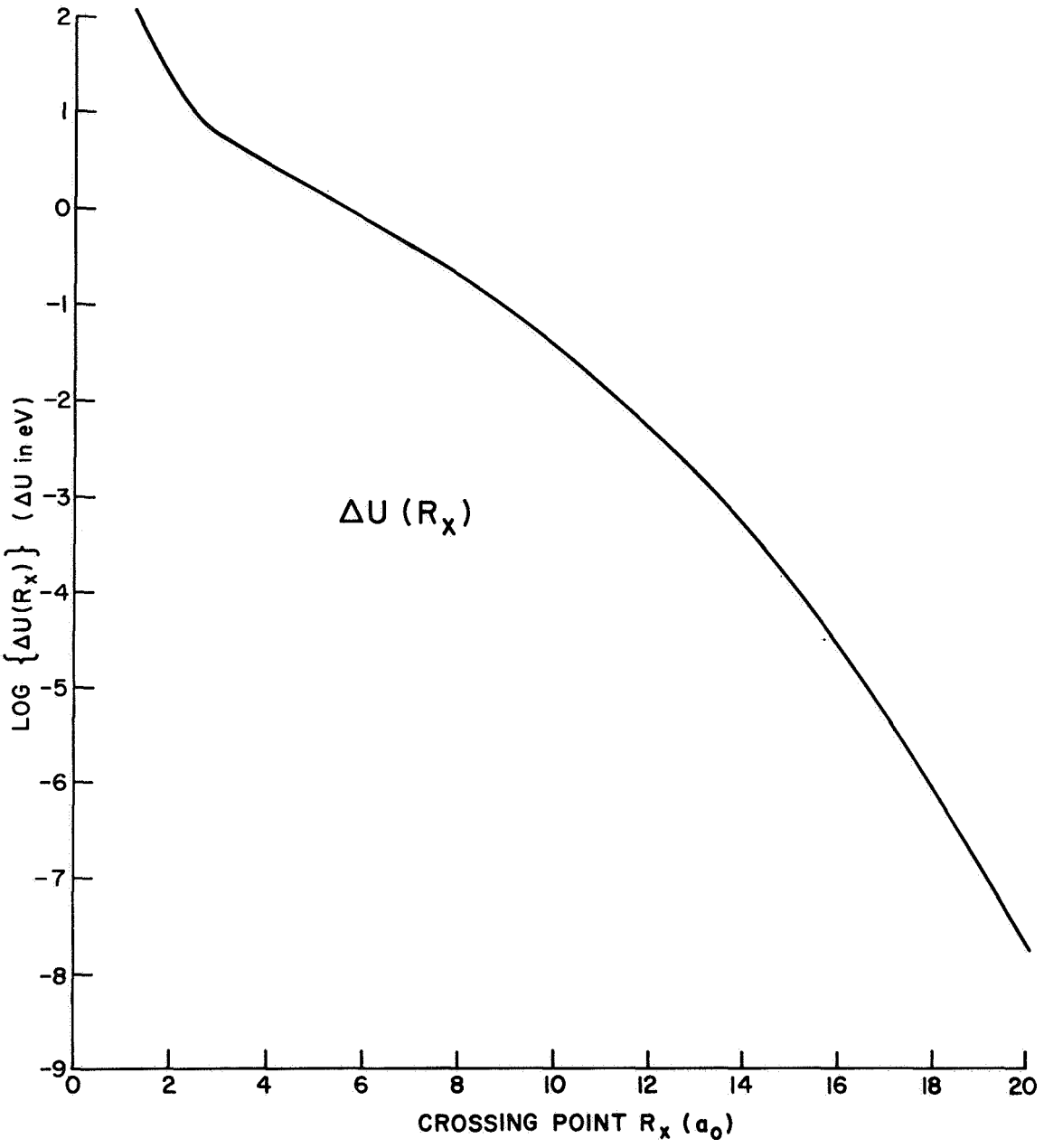

Fig. 2.B.1. Empirical $\Delta U(R_x)$ Function.
(Defined to be smooth curve of Hasted and Chong[16]).

points to orders of magnitude for other points. Nevertheless, without regard to the accuracy of the points or the precision of the curve fit, we define the function $\Delta U(R_x)$ to be the smooth curve of Hasted and Chong[16] (reproduced in Fig. 2.B.1), and define the Landau-Zener cross section function

$$\sigma^{LZ} = \sigma^{LZ}(\Delta E, Z, R_x, \Delta U(R_x), V_{rel}) \qquad (2.B.18)$$

The calculation of σ^{LZ} is performed by a computer routine requiring the input of the values of ΔE, Z, and the polarizabilities. The atomic masses are required only to compute the small quantity λ. Only the initial polarizability of the target is usually included. The value of R_x is primarily a function of $\Delta E/(Z - 1)$, and the polarizability is significant only at small R_x. The factor μ can be significant ($\sim .4$) for small R_x and/or for the targets with large atomic numbers and is included in the calculations. The factor $(Z - 1)$ enters in Eq. 2.B.3 for η in proportion to the velocity, so that, with all other quantities being equal, the cross section maximum is at smaller velocities for the more highly charged projectiles. A series of σ^{LZ} functions are plotted in Fig. 2.B.2 as a function of the relative velocity for a series of R_x values, for a $Z = 2$ projectile and for a target polarizability of Neon. These curves can be approximately applied to a particular process by taking the appropriate

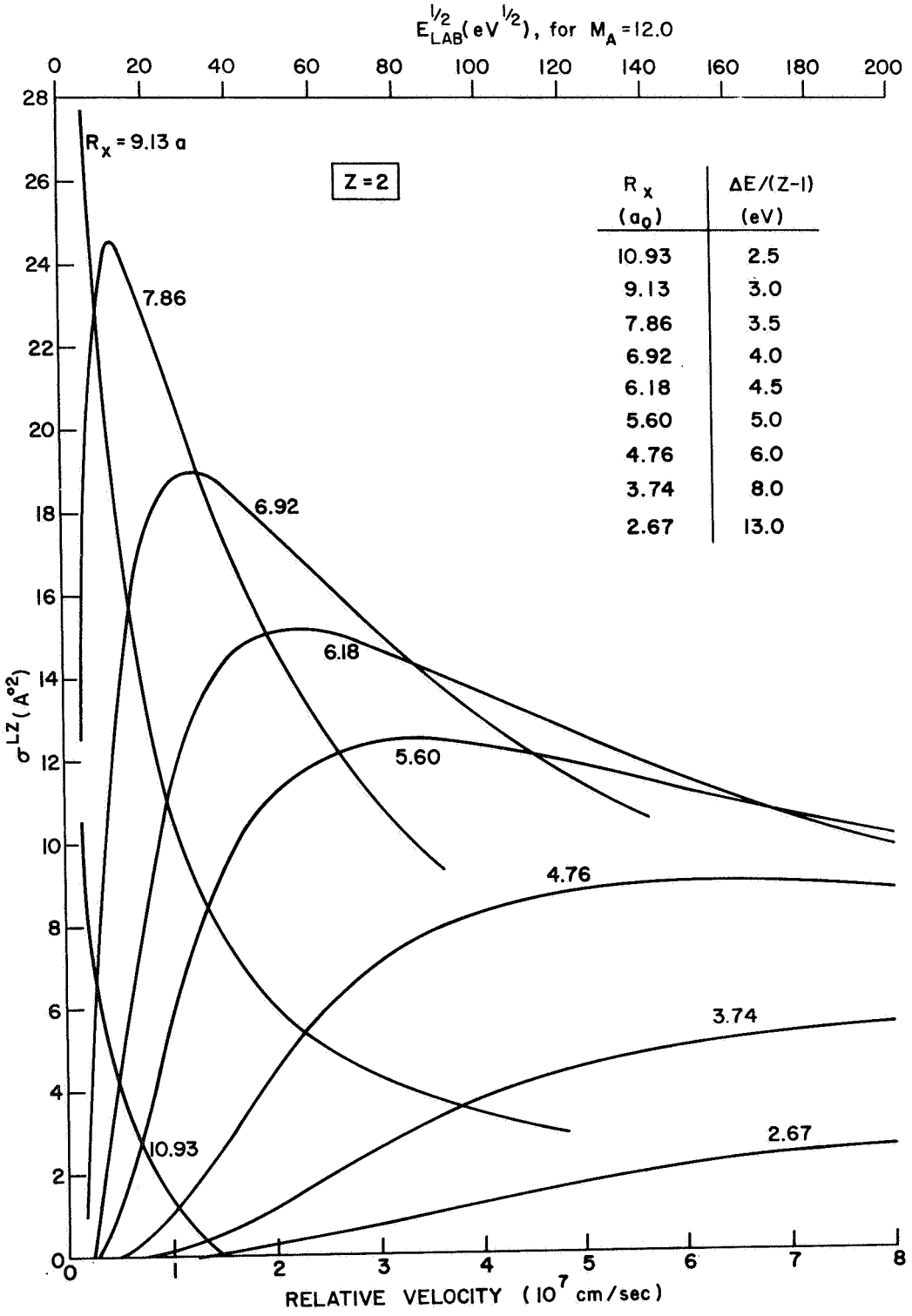

Fig. 2.B.2. Cross Section Function $\sigma^{LZ}(R_x, \Delta U(R_x), v_{REL})$.
(Defined in text, Eq. 2.B.16, for a given ΔE and Z).

$\Delta E/(Z - 1)$ value which gives a value of R_x ; the velocity scale must be divided by $(Z - 1)$.

The empirical application of the L - Z theory described above is subject, of course, to the validity of the $\Delta U(R_x)$ function as defined from the empirical curve and to the validity of the L - Z theory itself. However, the σ^{LZ} function as defined provides a rapid means of determining what cross section might be expected on the basis of the L - Z theory with all its implicit limitations.

C. BJS Solution of Two-State Approximation

1. BJS Formula

Coupled differential equations similar to (2.A.3) and (2.A.4) were derived by Bates, Johnson and Stewart[13] (BJS) and solved in a manner that considers the oscillatory nature of the transition probability and includes the effect of transitions away from the classical crossing point. These coupled equations are expressions for the complex coefficients, $c_n(z)$ and $c_m(z)$, corresponding to the two states, n and m, in terms of the matrix elements between the states; the complete electronic wave function is expressed as a combination of the atomic eigenfunctions that are taken to be spherically symmetrical, so therefore the applicability of the results is limited to $s - s$ transitions. BJS derive from these equations an expression for the probability of an ultimate transition from state n to state m as

$$P_{nm} = |c_m(\infty)|^2 = 4r_m(0)^2 \{1 - r_m(0)^2\} \sin^2\eta(0) \qquad (2.C.1)$$

where $r_p(z)$ is due to the expression of the coefficients in polar form, i.e.

$$c_n(z) = r_n(z) \exp\{i\theta_n(z)\}\ , \quad c_m = r_m(z) \exp\{i\theta_m(z)\} \qquad (2.C.2)$$

with $\eta(z)$ being a function of $\theta_n(z)$, $\theta_m(z)$, and an integral over a function of the matrix elements. The probability given by

Eq. 2.C.1 is in terms of the values of $r_n(z)$ and $\eta(z)$ at $z = 0$ where the colliding atoms are closest. The coupled equations are replaced by real equations for $r_n(z)$ and $\eta(z)$. Finally the BJS differential equations to be solved are

$$v \frac{dr_n(z)}{dz} = -\left\{1 - r_n(z)^2\right\}^{\frac{1}{2}} - \bar{K}(R) \sin \eta(z) \qquad (2.C.3)$$

and

$$v \frac{d\eta(z)}{dz} = -g(R) + \frac{2r_n(z)^2 - 1}{r_n(z)\left\{1 - r_n(z)^2\right\}^{\frac{1}{2}}} \bar{K}(R) \cos \eta(z) \qquad (2.C.4)$$

with the boundary conditions

$$r_n(-\infty) = 1 \ , \quad \eta(-\infty) = 0 \qquad (2.C.5)$$

and $\bar{K}(R)$ is a function of the matrix elements. The probability, P_{nm} , is a parametric function of the impact parameter, ρ , and the total transition cross section is thus given by

$$\sigma_{nm} = 2\pi \int_o^\infty P_{nm}(\rho)\rho d\rho \ . \qquad (2.C.6)$$

2. L - Z Model

Unfortunately, the equations of the last section are still rather far from a form that would permit one to see how the cross-sections vary as a function of various parameters such as velocity or R_x . Models given in terms of several parameters are designed to provide such insight; however, accuracy is usually traded for the gain in simplicity. This is certainly true for the Landau-Zener model, which treats the two (ingoing and outgoing) crossing points separately and assumes a particular form for the interaction matrix elements (cf. Sec. A).

Comparison of the L - Z probability, $P_{nm}^{LZ} = 2P(1 - P)$, with the BJS formula (2.C.1), reveals the association between $r_n(0)^2$ and P . The difference is that the BJS formula is oscillatory, whereas in the L - Z formula the separate probabilities were assumed to be additive. BJS point out that the $r_n(0)^2$ obtained by using L - Z type matrix elements would be identical with the L - Z probability P , if the crossing points are infinitely far apart. In this case, they also note that the respective cross-sections are approximately the same, since the phase angle, $\eta(0)$, is then random ($\sin^2\eta(0)$ averages to $\frac{1}{2}$) .

In order to demonstrate the oscillatory effects on the probability, BJS adopt the L - Z model for the interaction matrix elements (but not the L - Z addition of probabilities) and then numerically solve the Eqs. 2.C.3 and 2.C.4 . The oscillations in both $r_n(z)$ and $\eta(z)$ combine to produce complicated oscillations in the

total probability as given by the BJS formula. Solutions of the equations by BJS for various values of a parameter ω (a function of velocity, impact parameter, and the constants of the matrix element model) provide some insight into the nature of the process, and they show the importance of transitions away from the crossing point and the interference between the oscillatory terms. The utility of a numerical solution of the equations for a specific model is limited by the number of required parameters.

3. Solutions for Representative Processes

BJS apply their numerical solution to the specific processes

$$Be^{2+} + H \rightarrow Be^{+} + H^{+} \ (+ 4.61 \text{ ev}) \ , \quad R_x = 5.8 \ a_o \qquad (2.C.7$$

with a close crossing, and

$$Mg^{2+} + H \rightarrow Mg^{+} + H^{+} \ (+ 1.43 \text{ ev}) \ , \quad R_x = 18.9 \ a_o \qquad (2.C.8)$$

with a distant crossing and calculate the cross sections as a function of velocity. These processes are experimentally difficult to study; however, the qualitative features of the results can probably be extended to other processes. The parameter that provides the basis for the comparison is the crossing distance, R_x . This extension is reasonable because previous experimental results and calculations with the L - Z formula indicate that the interaction matrix elements

are primarily a function of R_x (cf. Sec. B). It should be emphasized that the BJS solutions and any L - Z calculations that have been made apply only to s - s transitions, and the results should not be indiscriminately extended to other transitions.

The BJS results for processes (2.C.7) and (2.C.8) are reviewed and presented here for reference. The probability vs. impact parameter results of BJS for process (2.C.7) are reproduced in Fig. 2.C.1 and clearly show the oscillatory effects. Their cross-section results are given in Fig. 2.C.2 as a function of the relative velocity of approach.

A considerable difference between the close crossing process (2.C.7) and the distant crossing process (2.C.8) is evident. For the close crossing provess, BJS note two essential differences between their solution and the L - Z model solution.[24] The maximum of the BJS solution is almost twice that of the L - Z solution because of the considerable contribution from the region outside the crossing point (i.e. $\rho > R_x$), and the magnitude is considerably larger at lower velocities, mainly because the matrix elements are considered as functions of the separation rather than as constants calculated at the crossing point.

The features of the cross-section for process (2.C.8) are related to several of the experimental cross-sections in Chap. 6. For distant crossings the L - Z model gives a single maximum at very low energies (cf. Sec. B) due to transitions near the crossing point. However the BJS calculations give a second maximum at a considerably higher velocity. This second maximum occurs because the maxtrix

elements are considered as a function of the separation, and their variation is such that the transition probability is high for closer encounters where the impact parameter, ρ , is less than about half of R_x . This second maximum is very important because it indicates that some cross-sections, previously thought to be very small except at low velocities on the basis of the L - Z theory, will be large through a wide range of velocities.

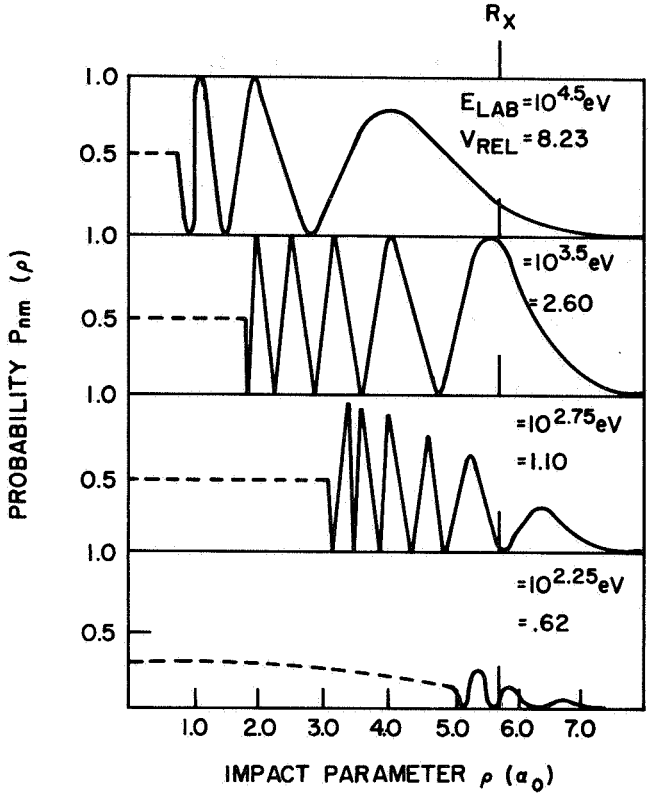

Fig. 2.C.1. Probability of $Be^{2+} + H \rightarrow Be^{+} + H$ as Function of Impact Parameter (From Bates, Johnson and Stewart[13]).

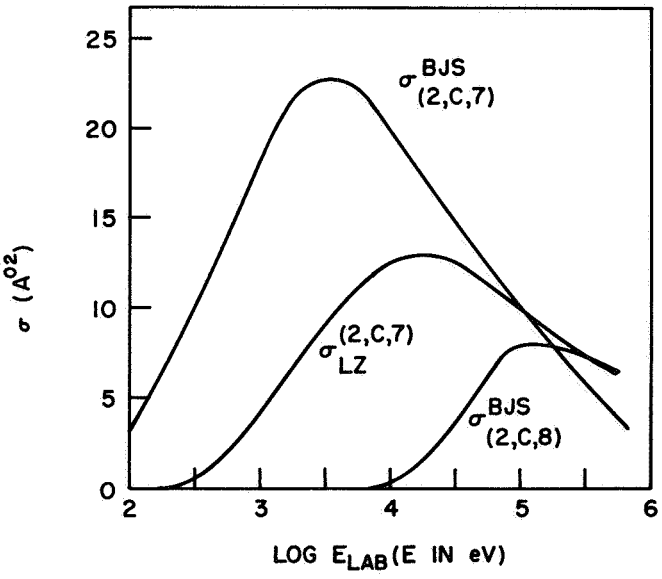

Fig. 2.C.2. Theoretical Cross Sections. (σ^{BJS} for (2.C.7) and and (2.C.8) from[13] and σ_{LZ} for (2.C.7) from[24]).

D. Processes Involving Two-Electrons

The discussion in previous sections of this chapter has been confined to consideration of the exchange of only one electron between two definite states. However, processes involving the change of state of more than one electron must also be considered. They are exemplified by two-electron capture, one-electron capture with excitation of the target and one-electron capture with an Auger-type of ionization of the target. Capture with target ionization is a special case of capture with target excitation for which the final state is in the continuum. At low energies, two-electron capture is usually less probable than one-electron capture, and in this experiment the measured cross-section does not include two-electron capture. However, the two electron processes of one-electron capture along with excitation or ionization of the target are included in the measured cross section for single-electron capture (see Chap. I.B) and must be considered in the interpretation of the results.

Considering the complexity of the theory of the one-electron process, it is not surprising that little can be said about the two-electron process of one-electron capture with target excitation or target ionization. In a sense the two-electron processes can be considered as second-order in that a coupling between the two electrons is required. If in a region of internuclear separations the initial and final states are closely spaced in energy, the probability of a two-electron transition might be large in some region of velocities. Therefore, it appears reasonable to consider the adiabatic potential

energy curves for the initial and final states and possible pseudo-crossings of these states. However, the L - Z theory, as discussed in previous sections of the chapter, is not applicable.

The magnitude of a cross section, σ, for any process is approximately proportional to the product of the square of the crossing distance at which it occurs and to the probability of a transition at that crossing distance. Therefore, the magnitude of a cross section can be qualitatively described for the many cases: transitions at small distances with high probability ($\lesssim 1$) imply small or moderate σ; transitions at moderate distances with small or moderate probability imply moderate or large σ; transitions at large distances with small probability imply moderate σ; transitions over a range of distances with small or moderate probability imply large σ, etc. Little can be said about the velocity dependence of any of these cases for the two-electron processes, except in a very speculative manner by comparison to the L - Z theory for one-electron transfer.

In the remainder of this section are considered collisions in which the final state is in a continuous spectrum of states; a rough estimate is made of the cross section at low velocities for electron capture with Auger-type ionization of the target for the C^{4+} + Argon collision.

Ionizing collisions that can occur as a result of curve-crossing have been considered by Bates and Massey[3], and they discuss the one-electron process

$$A + B \rightarrow A + B^{+} + e \qquad (2.D.1)$$

which is endothermic. The initial and final curves can have a pseudo-crossing because of the final polarizability interaction. The crossing between the initial curve (A and B) and the final curve (A and B^+ and an ejected electron with zero kinetic energy) is shown in Fig. 2.D.1. Inside the first crossing, R_{xo}, there is a continuum of states, for which the electron has a positive kinetic energy. This is an autoionizing region for the quasi-molecule (A + B). Bates and Massey give the following approximate formula for the cross-section

$$\sigma = \pi R_x^2 \left\{ 1 - e^{-\frac{R_x W}{v}} \right\} \qquad (2.D.2)$$

where W^{-1} is the life-time against auto-ionization and is assumed to be constant inside of R_x. More detailed treatments of this type of process have been made[32,33,34].

The two-electron process of single electron capture with ionization the target

$$A^{Z+} + B \rightarrow A^{(Z-1)+} + B^{2+} + e + E \qquad (2.D.3)$$

is exothermic if the recombination energy of the projectile is greater than the sum of the first and second ionization potentials of (IP_1 and IP_2) the projectile, i.e.

$$IP_Z(A) > IP_1(B) + IP_2(B) \cdot \qquad (2.D.4)$$

Whereas the previous ionizing process (2.D.1) had a continuum of

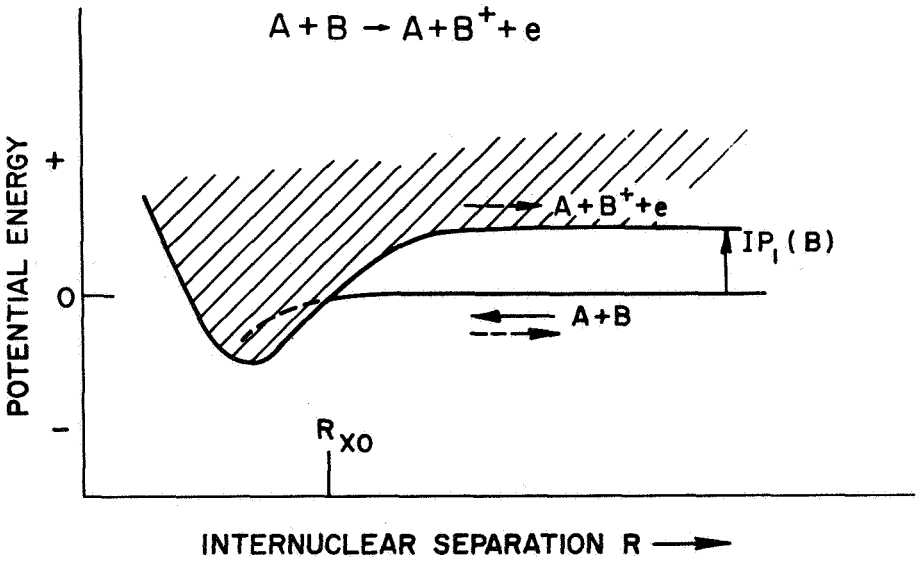

Fig. 2.D.1. Potential Energy Curves for Ionizing Collision

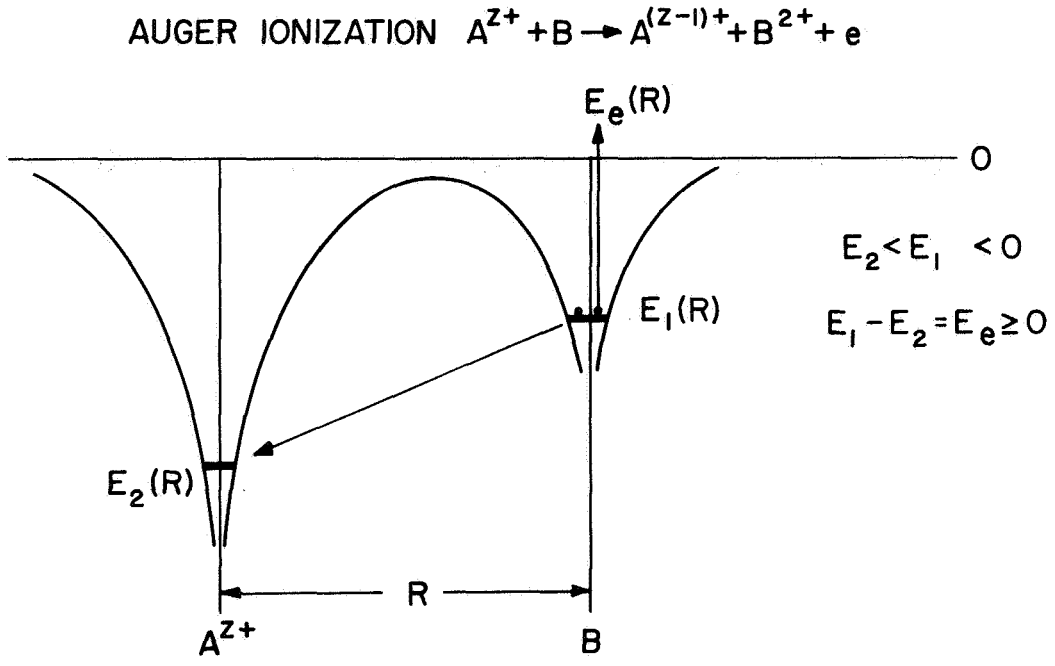

Fig. 2.D.2. Electronic Potential Energy-Level Diagram for Auger Ionization. (From Kishinevsky and Parilis[35]).

states inside some crossing point, process (2.D.4) has a continuum of states outside of a crossing point, R_{xo} . The crossing point, R_{xo} , is defined by the intersection of the initial curve with the final curve (for $A^{(Z-1)+}$ and B^{2+} and an ejected electron with zero kinetic energy, see Fig. 2.D.4). An important feature of both processes (2.D.1) and (2.D.3) is that they are isoenergetic, the excess bound electronic energy going into kinetic energy, E_e of the free electron. Also the transitions are not confined to some region about a crossing point.

The lifetime (W^{-1}) against autoionization for (2.D.3) is clearly not approximately constant. For example, only when the internuclear separation is small enough for the system to be quasi-molecular with sufficient overlapping of the wave functions can autoionization occur. Therefore, with W a function of R , the formula corresponding to (2.D.2) for this case is

$$\sigma = 2\pi \int_o^\infty \left\{1 - \exp\left[-\frac{2}{v}\int_\infty^\rho \frac{W(R)RdR}{(R^2-\rho^2)^{\frac{1}{2}}}\right]\right\}\rho\, d\rho \quad . \qquad (2.D.5)$$

Eq. (2.D.5) requires a knowledge of the transition probability per unit time, $W(R)$, as a function of R .

In the autoionizing region the quais-molecule $(A^{Z+} + B)$ is an excited system. As noted by Kishinevsky and Parilis[35], the mechanism whereby one electron fills a vacancy in a lower level and the other electron is ejected, is of the Auger type, shown schematically in Fig. 2.D.2. They compute the transition probability per second

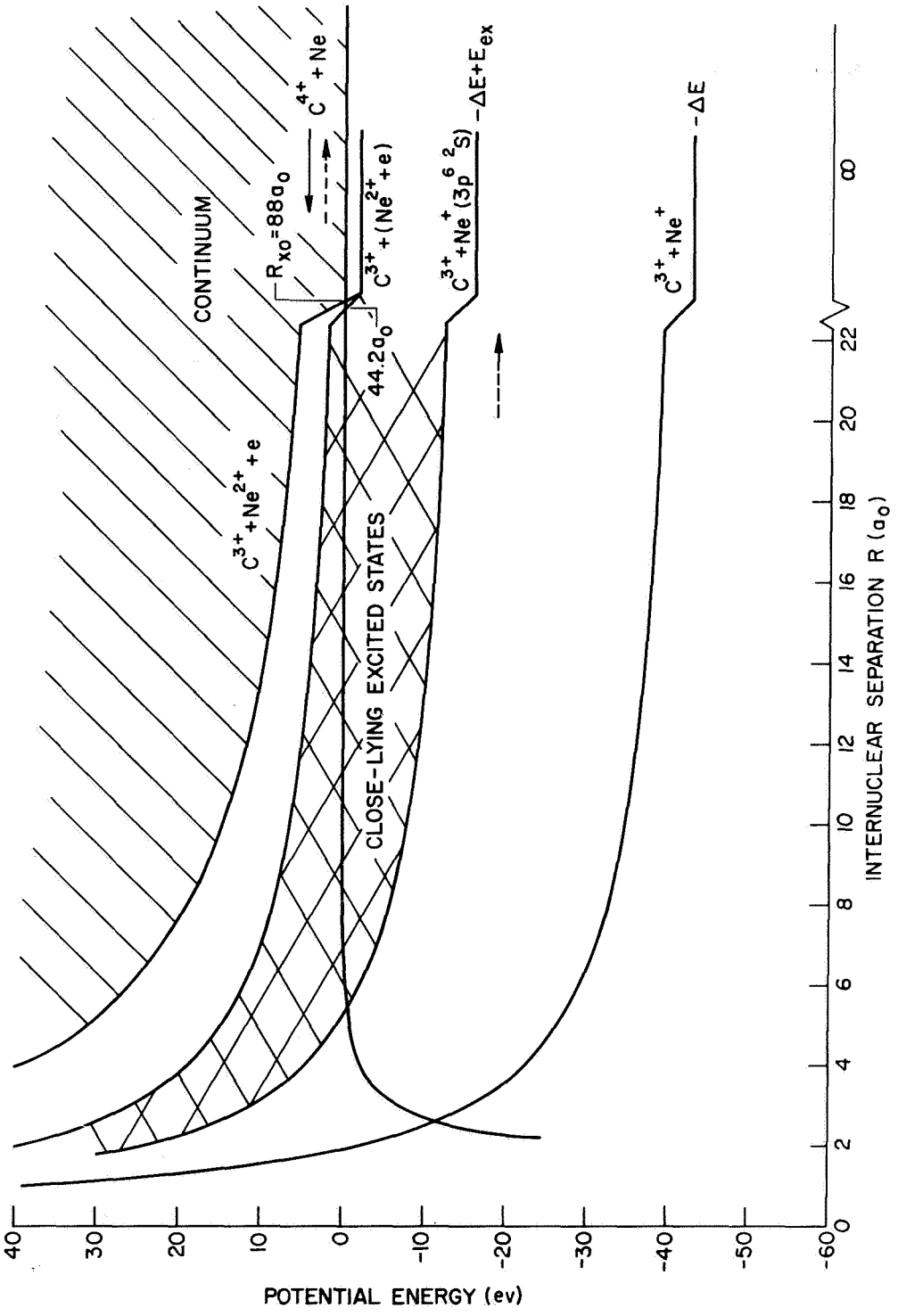

Fig. 2.D.3. Approximate, Pseudo-Crossing Potential Energy Curves for C^{4+} + Neon. (For single-electron capture into 2s $^2S_{\frac{1}{2}}$ ground state of C^{3+} with various final, excited levels of Neon).

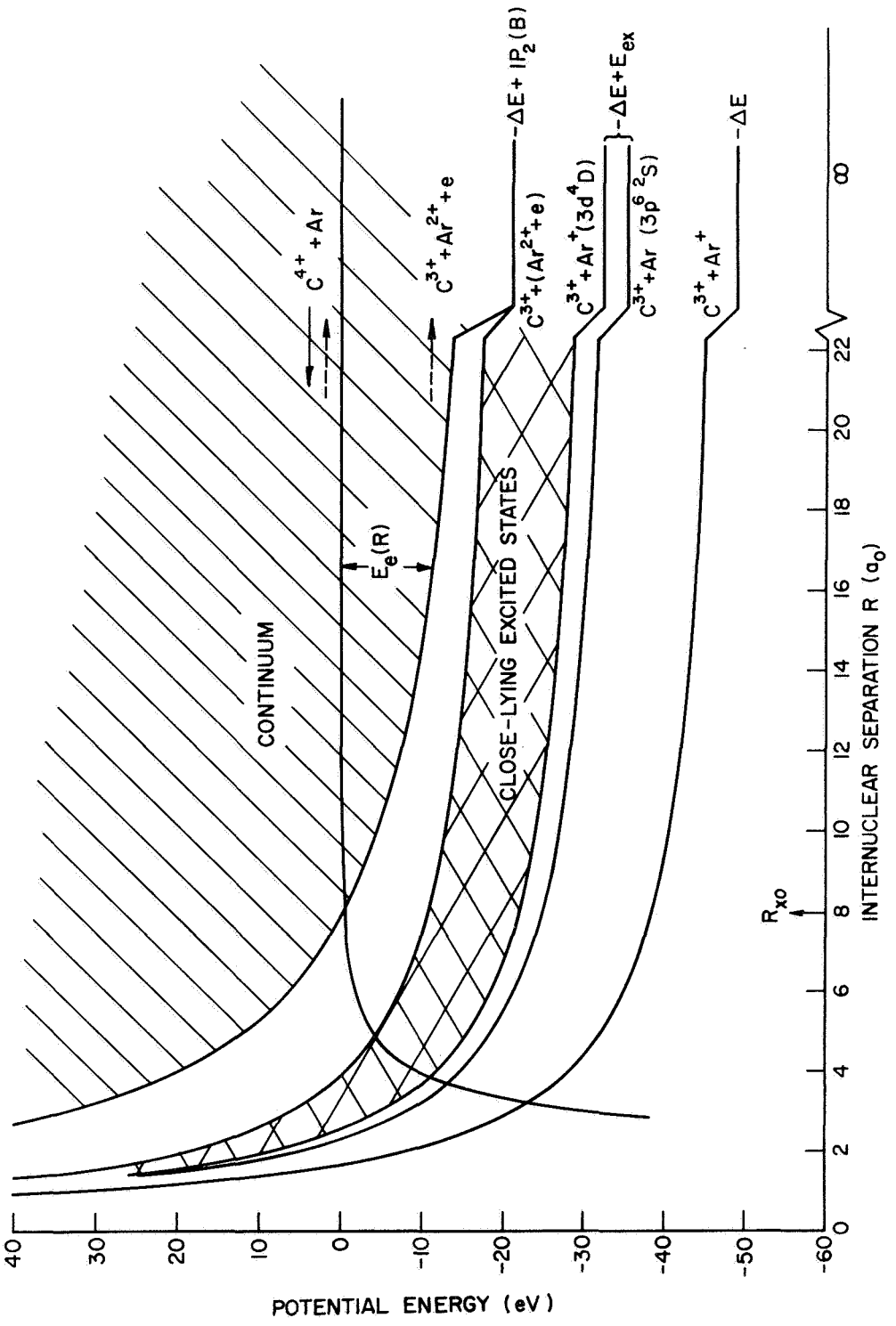

Fig. 2.D.4. Approximate, Pseudo-Crossing Potential Energy Curves for C^{4+} + Argon. (For single-electron capture into $2s\ ^2S_{\frac{1}{2}}$ ground state of C^{3+} with various final, excited levels of Argon).

$W(R)$, for the model of two electrons in the field of two Coulomb centers separated by a fixed distance, R . The probability obtained from their calculation has a maximum ($\sim 4 \times 10^{15}$/sec) at the internuclear separation, R , where the energy of the ejected electron is a minimum. The magnitude of their cross section for this model is of order 3×10^{-16} cm^2 at a velocity of 10^6 cm/sec , and it decreases slowly with increasing velocity.

We now consider the specific cases of C^{4+} + Neon and C^{4+} + Argon, both of which satisfy Eq. (2.D.4) so that the Auger ionization process (2.D.3) is exothermic. The approximate, pseudo-crossing potential energy curves are shown in Figs. 2.D.3 and 2.D.4. The energy terms included in the curves are the initial polarizability of the neutral target in the initial curve and the Coulomb repulsion in the final curve. Note that the crossing points, R_{xo} , are quite different for the Neon and Argon targets, i.e. 88 a_o and 8.0 a_o respectively because the energy defects are 1.85 ev and 21.1 ev respectively. Also shown are the curves for target excitation including only the energy terms noted above. All the curves are for capture into the ground $2s^2S_{\frac{1}{2}}$ state of C^{3+} . Capture into the $n = 3$ excited states of C^{3+} is also exothermic (see Table 6.2), but these curves are not shown in the figures.

Considering the C^{4+} + Argon curves, we note that the initial curve lies in the continuum of final states, but it is not clear how the initial state interacts with the continuum states or with their boundary for which the electron energy is, $E_e = 0$. Obviously, a quantum mechanical description considering all states would be complex.

However, a qualitative comparison of C^{4+} + Neon and C^{4+} + Argon can be made because of the large difference in their crossings, R_{xo}. Since for the Neon target $R_{xo} = 88\ a_o$ is very large, little interaction with the continuum states can be expected. However, for the Argon target $R_{xo} = 8.0\ a_o$ is a moderate value, and it seems reasonable to expect that interaction with the continuum states resulting in Auger-type ionization is probable.

A rough estimate of the cross section for electron capture with Auger-type ionization of the target can be made. We define R_e as an effective radius inside of which there is an interaction with the continuum states and define $\bar{W}$ as the average transition probability per second for $R < R_e$. Then Eq. 2.D.5 is

$$\sigma \approx \pi R_e^2 \left\{ 1 - e^{-\frac{\bar{W}R_e}{V}} \right\} . \qquad (2.D.6)$$

Choosing $R_e = R_{zo} = 8\ a_o = 4.2\ A°$ for C^{4+} + Argon, we note that the probability term enclosed in parenthesis is of order one for $\bar{W} \gtrsim 10^{15}$/sec at $V = 10^7$ cm/sec. The estimated cross section is then approximately equal to the geometrical factor,

$$\sigma \approx \pi R_e^2 = 55\ A°^2 \qquad (2.D.7)$$

Even if the transition probability were an order of magnitude less, the estimated cross section would still be large because of the large geometrical factor.

CHAPTER III

PULSED-DISCHARGE ION SOURCE

Ionization by electron impact is the usual method of producing singly or multiply-charged ions. A review of various types of ion sources is made by Hasted[36] who mentions pulsed sources. A common type of electron-impact ion source is one in which a gas is bombarded by a well-controlled beam of electrons; this type of source is sometimes operated in a discharge or plasma mode by increasing the gas pressure and electron current. These electron-impact and/or plasma discharge sources are typically characterized by: continuous ouput of current, production of mostly singly-charged and doubly-charged species, typical output currents of up to 10^{-6} amperes, and some production of more highly-charged ions of elements with large atomic numbers (e.g. Kr^{4+}). The lighter elements, however, are more difficult to multiply-ionize and many are not gaseous at near room-temperatures. For example, carbon ions can be produced in an electron-impact ion source from the gaseous compound CO_2, but the charge state is essentially limited to $Z \leq 2$ in that type of source. A pulsed-discharge ion source that produces carbon (4+), and its operation in a collision experiment, are described in the following sections.

A. Design and Operation

In order to increase the average charge state of the ions from a source, it is necessary to increase the rate of electron impact; the energy of many of the electrons must of course be greater than the ionization potentials of each charge state to be produced. These requirements can be met by creating a high-temperature plasma using an electrical discharge of high current.

The source developed for this experiment has evolved from the washer-type, pulsed-plasma gun using hydrogen loaded titanium washers[37] . Eubank and Wilkerson[38] observed ions in the output of their hydrogen plasma source characterized by $M/Z = 3$, apparently C^{4+} generated from impurities in the vacuum system. On the basis of that observation carbon was introduced in the present source by using graphite electrodes and graphite washers to form the discharge cavity, as shown in Fig. 2.A.1.

The central graphite electrode of the source is connected to a .1 μf capacitor charged to 10 KV to 15 KV relative to the first concentric washer which is statically at the potential, V_{acc} . A fast triggering pulse of polarity opposite to the voltage of the central electrode is applied to the first washer; the discharge of the small .002 μf capacitor in the trigger circuit causes initial vaporization and ionization of electrode material. The main (.1 μf) capacitor then discharges along the washer stack producing additional ionization. The circuit path of the main capacitor discharge is short in length for low inductance and the main capacitor discharges in about 2 μsec.

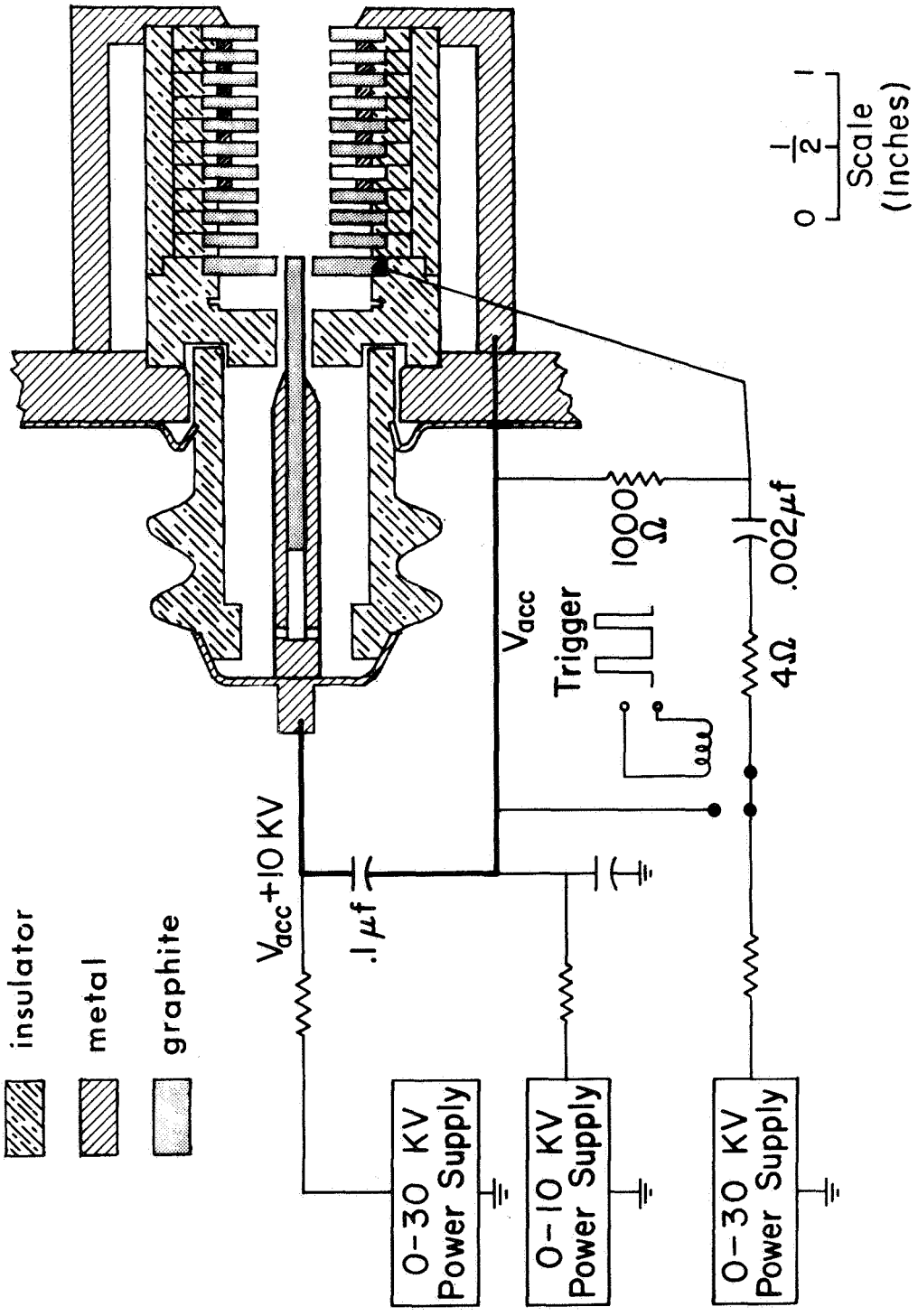

Fig. 3.A.1. Pulsed-Discharge Ion Source (Scale drawing and electrical circuits).

The dense plasma that is formed in the cavity expands outward along the axis and through a drift region approximately 50 cm long, during which the density falls to a value where space charge and Debye screening are unimportant. After the expansion, it is possible to control the motion of the ions by electrostatic and magnetic fields. The source and the discharge and triggering circuits are raised to a positive potential, V_{acc}, so that the ions are electrostatically accelerated, after expansion of the plasma, to higher energies than those naturally generated by the source.

Fig. 3.A.2 illustrates the time of flight analysis made of the output of the ion source. A 127° focusing, electrostatic energy analyzer selects ions with an energy per unit charge ratio that is proportional to the symmetric voltages applied to the deflecting plates. The analyzer is followed by a secondary emission type ion detector. Knowing the dependence of the kinetic energy on mass and velocity and using the total path length and energy selector setting, it is possible to identify the peaks corresponding to ions of different mass per unit charge on the time resolved detector signal. Such an oscilloscope trace is also shown on Fig. 2.A.2. Note that after the $m/z = 1$ and $m/z = 2$ peaks, which appear to be hydrogen impurities generated from the hydrocarbon material used as a binder for the graphite, peaks corresponding to C^{+4}, C^{+3}, C^{+2}, and C^{+1} appear. There are no significant peaks corresponding to other possible impurities (e.g., N^+, O^+, Si^+, etc.)

Investigation of the output at various ion energies shows that

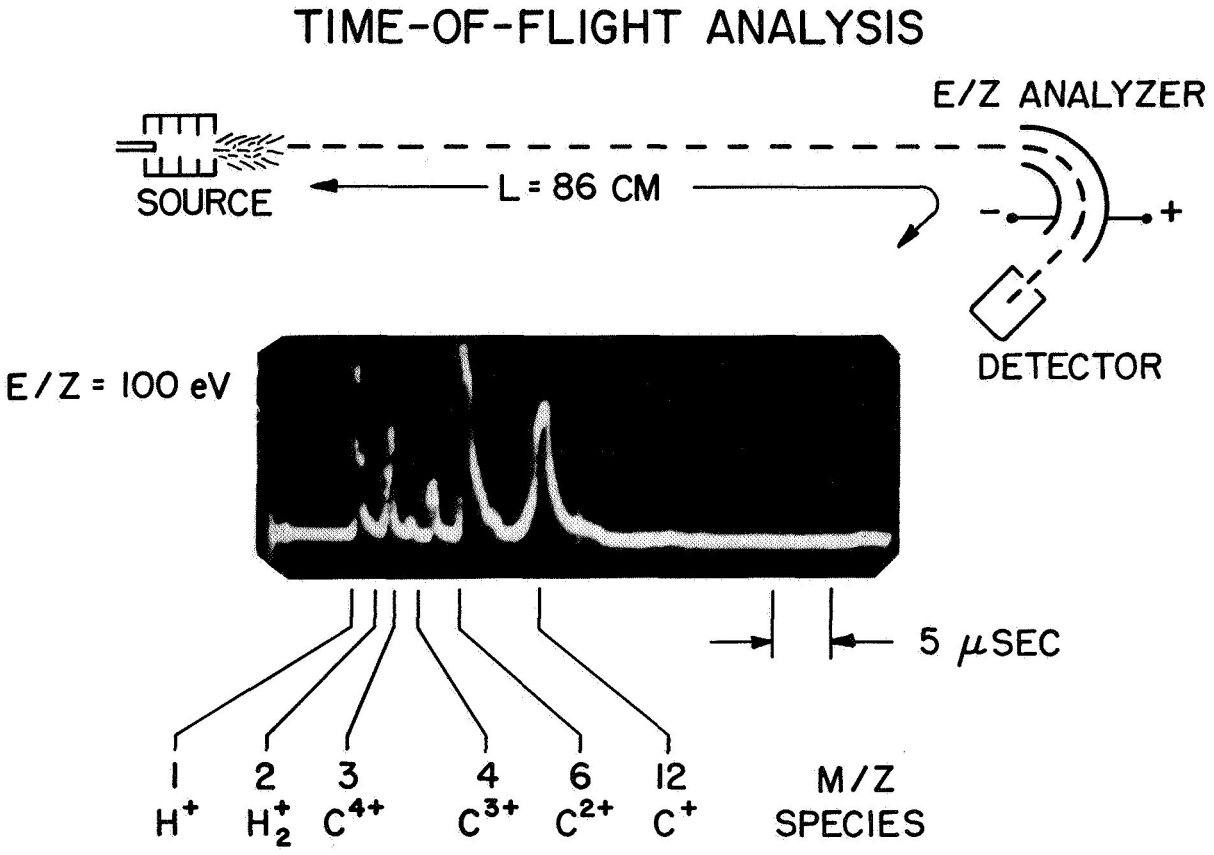

Fig. 3.A.2. Time-of-Flight Analysis of Output from Pulsed-Discharge Ion Source.

there is a wide range in the energy of the output as would be expected from such a source. Fig. 3.A.3 presents the relative intensity, averaged over a number of shots, for the various carbon ion peaks at different energies. Zero acceleration potential, V_{acc}, was used for these measurements. Note that the C^{+4} signal is about one order of magnitude less than that of the less highly charged ions. Because the x-axis is plotted in terms of kinetic energy per unit charge, a plot of this data as a function of true kinetic energy would show each of the curves for increasing charge state shifted to successively higher energies. Although this graph does not reflect the different efficiencies with which the detector records the various ion charge states, detailed calibration would not be expected to change the qualitative nature of the curves. Using estimated sensitivities it can be calculated that 10^3 to 10^5 ions per pulse enter the detector.

The bandwidth of the energy analyzer is a linear function of the selected energy, i.e. the range of energies passed by the energy selector is a constant fraction of the central, selected energy. The dependence of the measured relative intensity (as shown in Fig. 3.A.3) on the bandwidth can be removed by dividing the intensity by the energy. The result is a true distribution of the relative intensity of the source output per unit of energy per unit charge and is shown in Fig. 3.A.4. Note that the distributions in Fig. 3.A.4 peak toward zero energy. Acceleration of all ions to a higher energy, with subsequent selection of ions in an energy band that is a fraction of the higher energy, increases the intensity of useable ion output. Therefore, the wide spread in the energy of the output is less restrictive at high energies

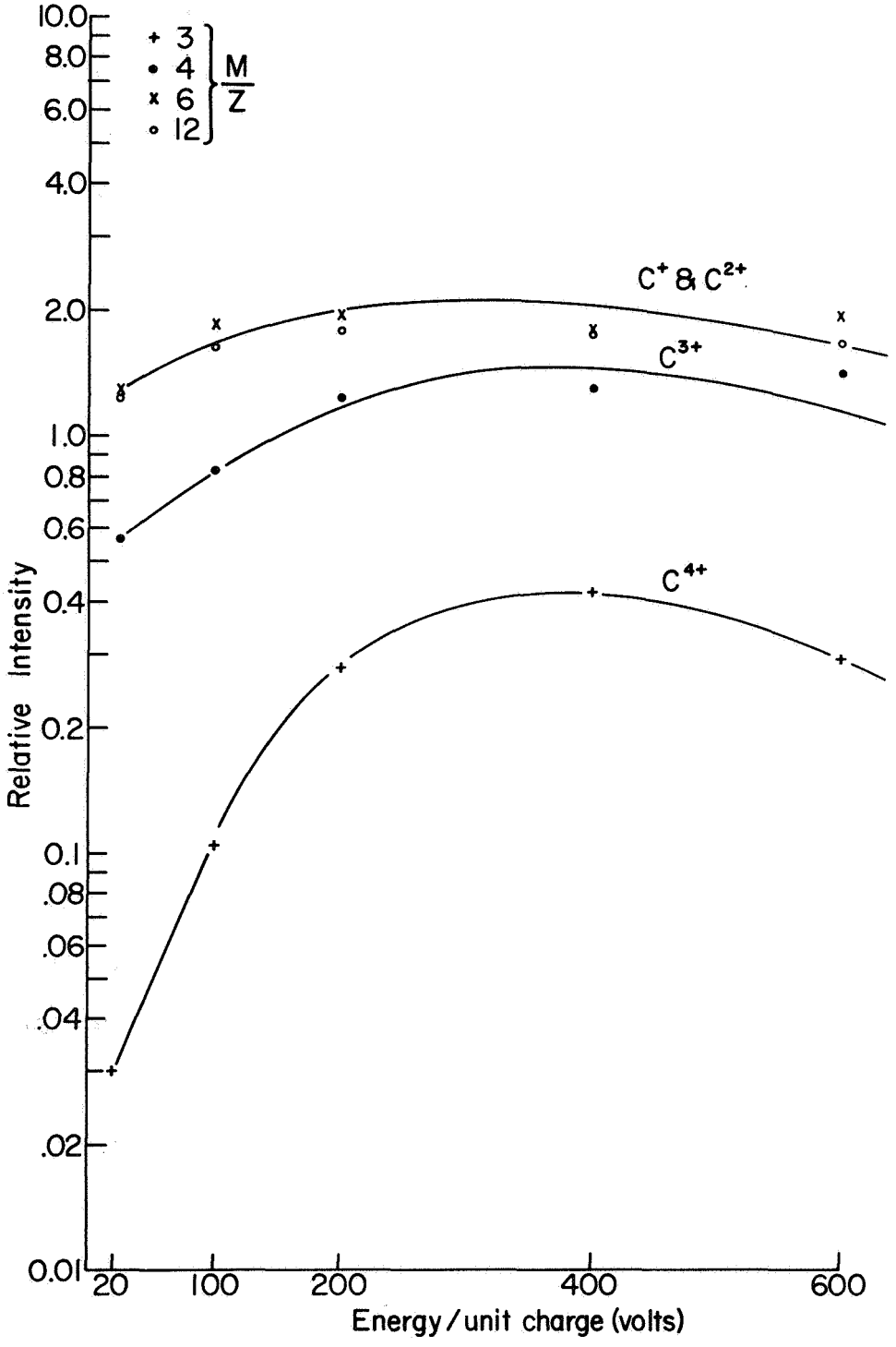

Fig. 3.A.3. Pulsed-Discharge Ion Source Output. (Each point is an average over about 20 pulses).

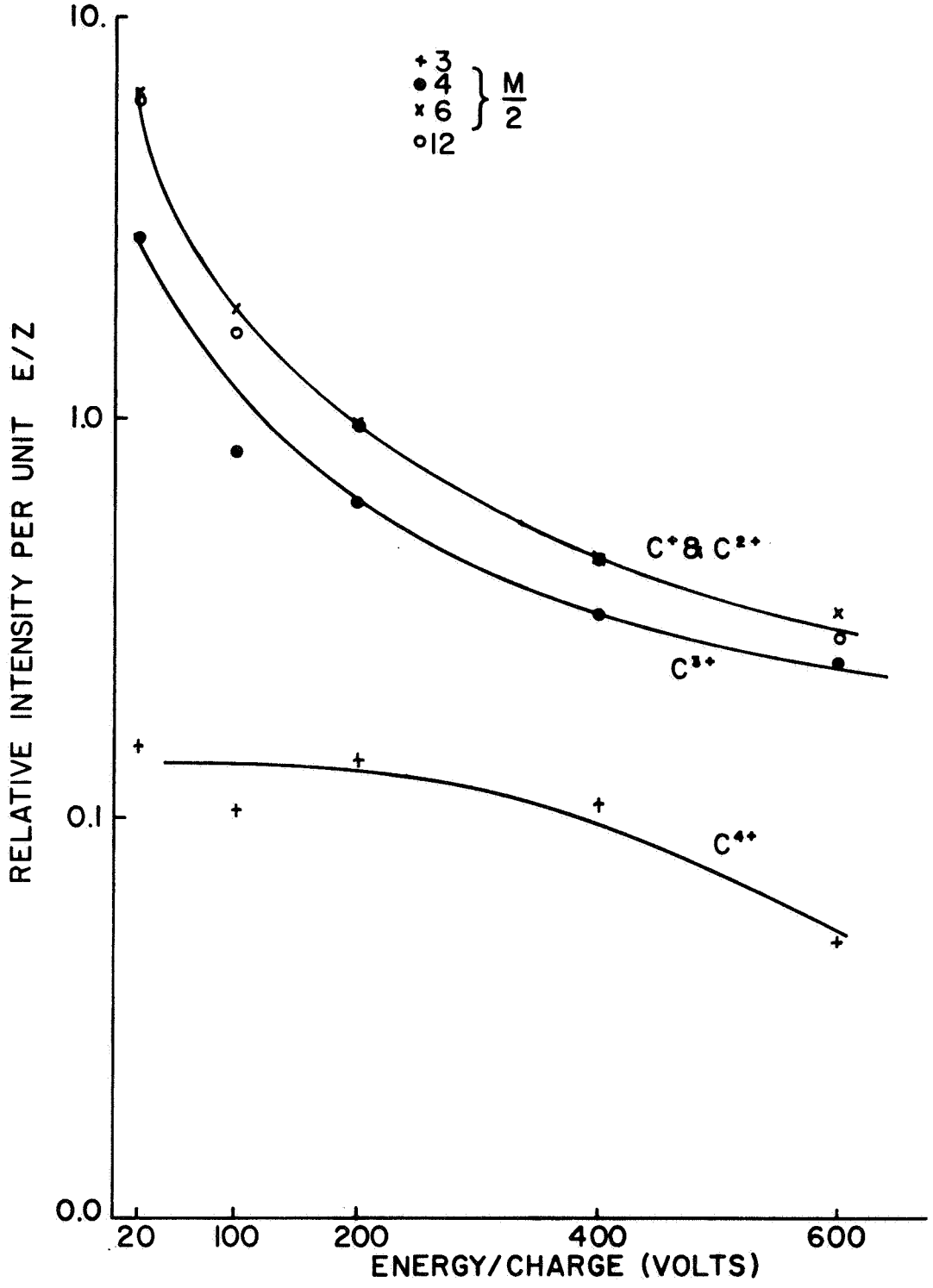

Fig. 3.A.4. Pulsed-Discharge Ion Source Output per Unit of E/Z. (Each point is an average over about 20 pulses).

if the required energy bandwidth is a fraction of the central, selected energy.

The measurements shown in Figs. 3.A.3 and 3.A.4 were made with the main capacitor charge to minus 10 KV. Subsequent to these measurements the triggering circuit was modified to that shown in Fig. 3.A.1. The improved circuit would also trigger the main capacitor when it was charged to a positive voltage. The mode with the main capacitor positively charged seemed to give a more reliable ion output and was used for the measurements in the collision experiment.

In the collision experiment the desired ion species and its energy is selected by a double-focusing mass spectrometer (cf. Chap. 4.A). Fig. 3.A.5 shows the relative location of the source, the drift region, the acceleration region, and the first slit of the mass spectrometer. The accelerating voltage used to obtain higher ion energies is about 50 to 100 volts less than the desired ion energy. The useable output is a maximum in the approximate range of energy per unit of charge of 1 kev to 6 kev; it is small at higher energies perhaps due to defocusing in the accelerating region, and also smaller at lower energies because of the relatively wider spread in the energy of the ion source output.

Thousands of discharges can be made without severe erosion of the electrodes. Most erosion that does occur is from the central electrode, which occasionally must be replaced. Usually, the life of the source between cleanings is limited by a uniform coating of graphite that is deposited on the insulator behind the first washer (trigger electrode). Eventually, the trigger breakdown occurs along this coating

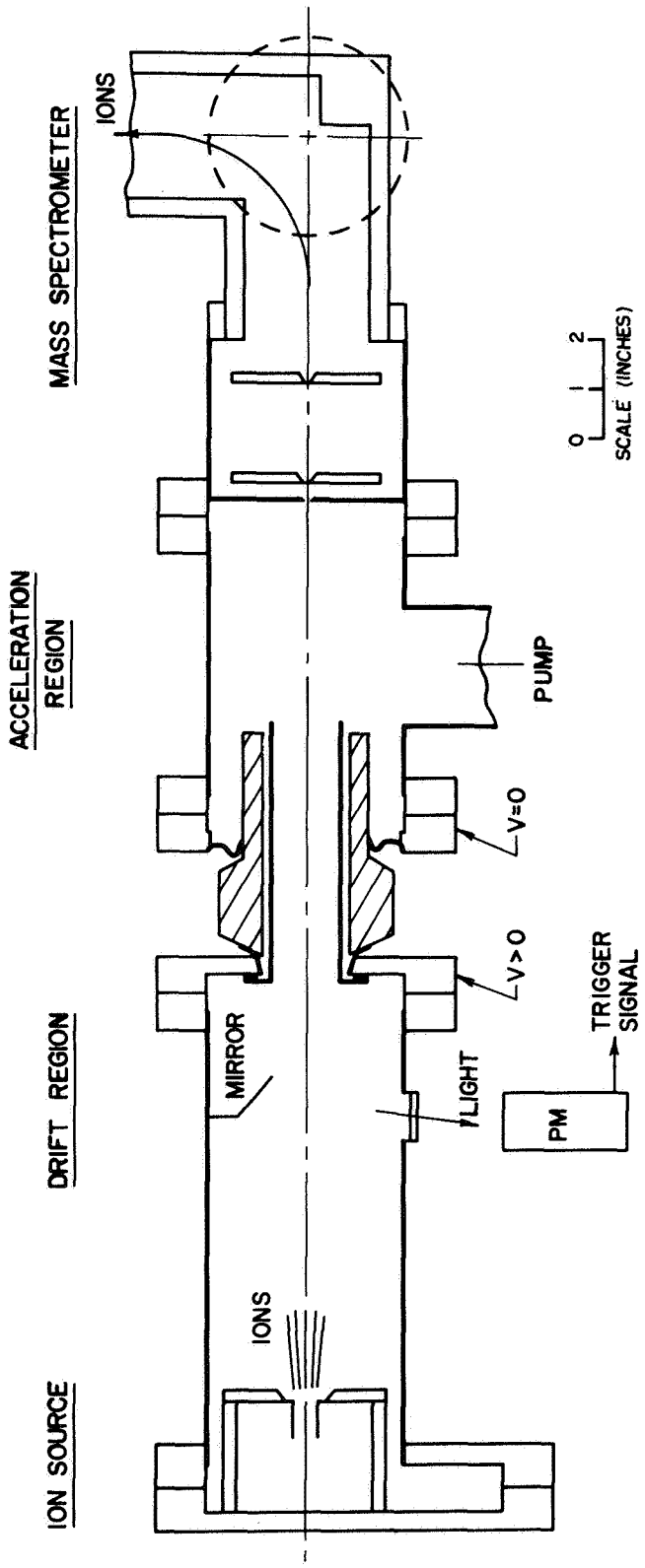

Fig. 3.A.5. Relative Location of Pulsed Source, Drift Region, Acceleration Region, and Mass Spectrometer.

on the insulator, and then cleaning is required. The groove around the inside of the insulator increases the time between cleanings.

During preliminary studies with the present source, copper-clad graphite electrodes were used, and output peaks identified as copper ions were observed. In principal, any conductive material that can be formed into electrodes should be suitable for production of ions in various charge states; a large number of ion species that were previously inaccessible should be available for experimental measurements.

B. Use with a Collision Experiment

The use of a pulsed-discharge ion source to produce ions for measurement of collision cross sections poses a number of experimental problems that are essentially problems of ion detecting and signal recording. The characteristics of the source that cause the main difficulties are: short duration of the ion output (low average output), large variation of the output from pulse to pulse, neutral gas output, and generation of radio frequency noise. A coordinated design of the source, detectors, and recorders has made these measurements possible.

Each pulse of the ion source is sufficient to make an experimental measurement if each of the measured quantities represents a statistically significant number of events. Otherwise, these quantities must be summed (before or after recording) over a sufficiently large number of pulses of the ion source. Typically, for electron capture with normal target density and single collision conditions of order

one in 10^2 projectile ions captures an electron. Therefore, the total number of incident ions must be at least of order 5×10^4 for a meaningful measurement. The design of an ion detector that has a range of measurement of from one ion per pulse to of order 10^5 ions per pulse is described in Chap. 4.E and App. A.

The variation in output of the source from pulse to pulse is more than an order of magnitude; therefore, each of the quantities must be measured for each pulse. For the measurements of total cross section in this experiment the problem of variable output is overcome by using a detector and a recorder for each of the two charge states measured (e.g. simultaneous measurement of both C^{4+} and C^{3+}). The output of each detector is recorded on a gated, peak-reading, memory voltmeter. Each voltmeter is gated to measure the height of the signal that occurs when the ions arrive at the detector; spurious signals or r - f noise from the electrical discharge of the source outside this time interval are partially avoided by the gating; and the height of the signal is related to the number of ions as described in App. A. The methods of data recording and analysis that are used to obtain statistically significant measurements are described in Chap. 5.

Careful consideration must be given to the design or isolation of electronic circuits used with a pulsed-discharge ion source in order to avoid the problem of r - f interference. The r - f noise generated by the discharge is partially isolated from the detectors by the insulator between the ion source and the accelerating section (cf. Fig. 3.A.4), and the voltage supplies for the source are physically separated from the other equipment. The voltage supplies on the

detectors, the mass spectrometer, and the 45° separator were modified to prevent the r - f pickup from causing a momentary loss of regulation. The r - f pickup in the detector circuits was reduced to a sufficiently low level to avoid erroneous signals.

The quantity of neutral gas output is reduced by differential pumping and by baffles on the source section. Also, since the neutral gas travels slower than the ions and the pulse of ions is of short duration, the neutral gas emerges from the mass spectrometer after the ions, and so does not affect the results of the collision measurements.

Measurements of such quantities as a beam profile, mass spectrometer resolution, detector calibration factors, and differential cross sections, for which it is difficult or impossible to measure all the required quantities for each pulse, would require a large number of pulses to average over the variable output and/or an elaborate measurement scheme. For this reason, performance tests and calibrations of the associated experimental equipment are made with the constant output of an electron-impact ion source.

The advantage of the pulsed-discharge ion source is that it can produce ions previously unavailable for collision measurements. However, even simple collision measurements are difficult to make with this source.

CHAPTER IV

THE APPARATUS

The basic components of the apparatus, shown in Figs. 4.1 and 4.2,are: an ion source, a mass spectrometer, a gas cell and pressure gauges, moveable post-collision slits, a post-collision charge separator and the ion detectors. Ions are produced in the source, selected according to energy, mass and charge state and formed into a beam; then they collide with neutral atoms in the gas cell. After collision, the ions can be selected by direction with moveable slits and separated by charge state with an electrostatic field. Finally, the ions are detected in the form of an electronic signal from one of the secondary-emission ion detectors. The ion source was described in the previous chapter, and the other components are described in the following sections. An electron-impact ion source with a continuous ion output was used for the operational tests of the various components.

A. Mass Spectrometer

The double-focusing mass spectrometer selects one species (mass per unit charge) with an energy per unit charge range of about four percent. This instrument has been designed[39] according to the ion-optic equations derived by Mattauch and Herzog[40]. The proper slit positions to obtain optimum resolution were determined by an empirical investigation of the directional focusing properties. A maximum resolution of about 1000 has been achieved. Precision machining was

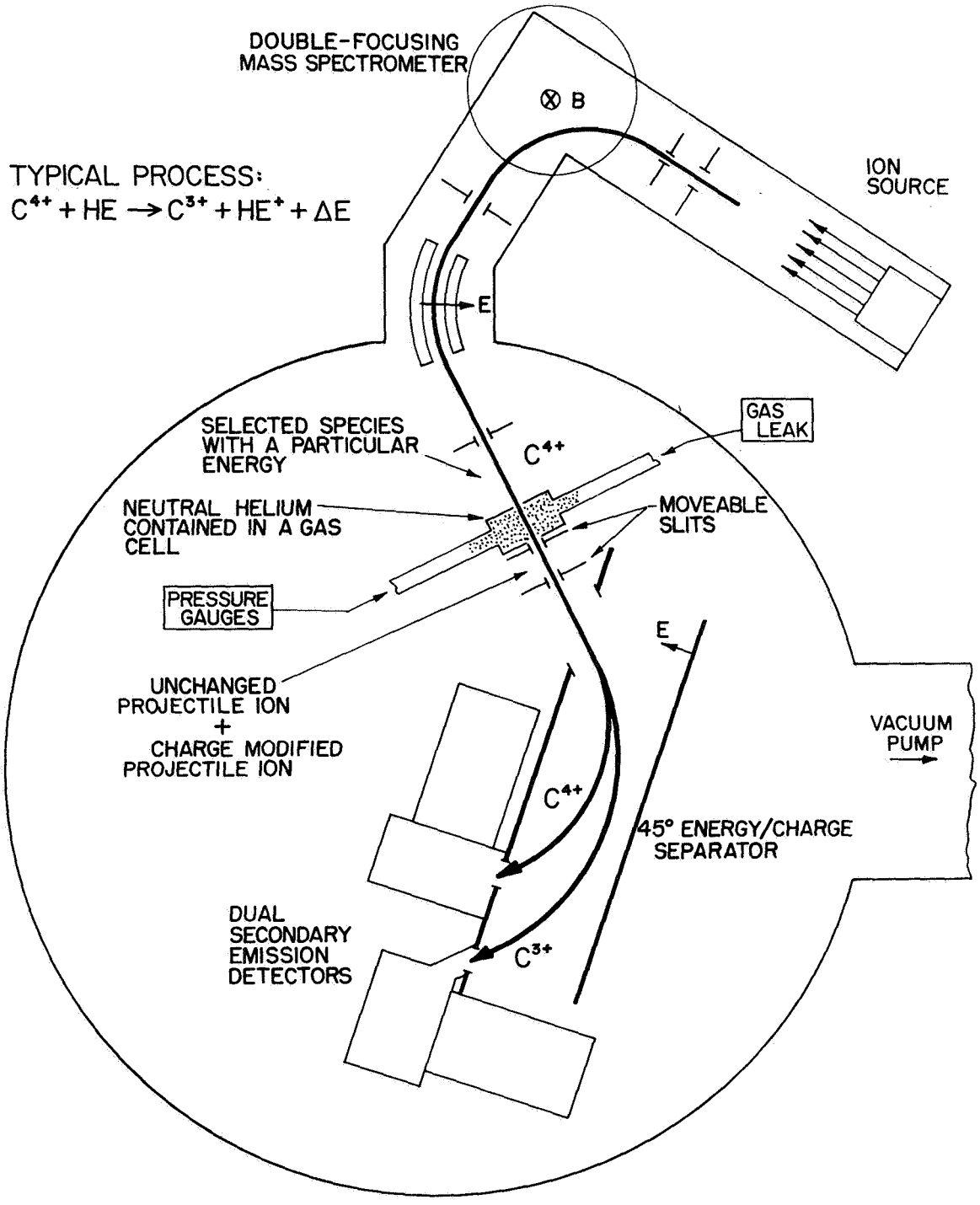

Fig. 4.1. Apparatus for Measurement of Electron Capture Cross Sections for Multiply-Charged Ions.

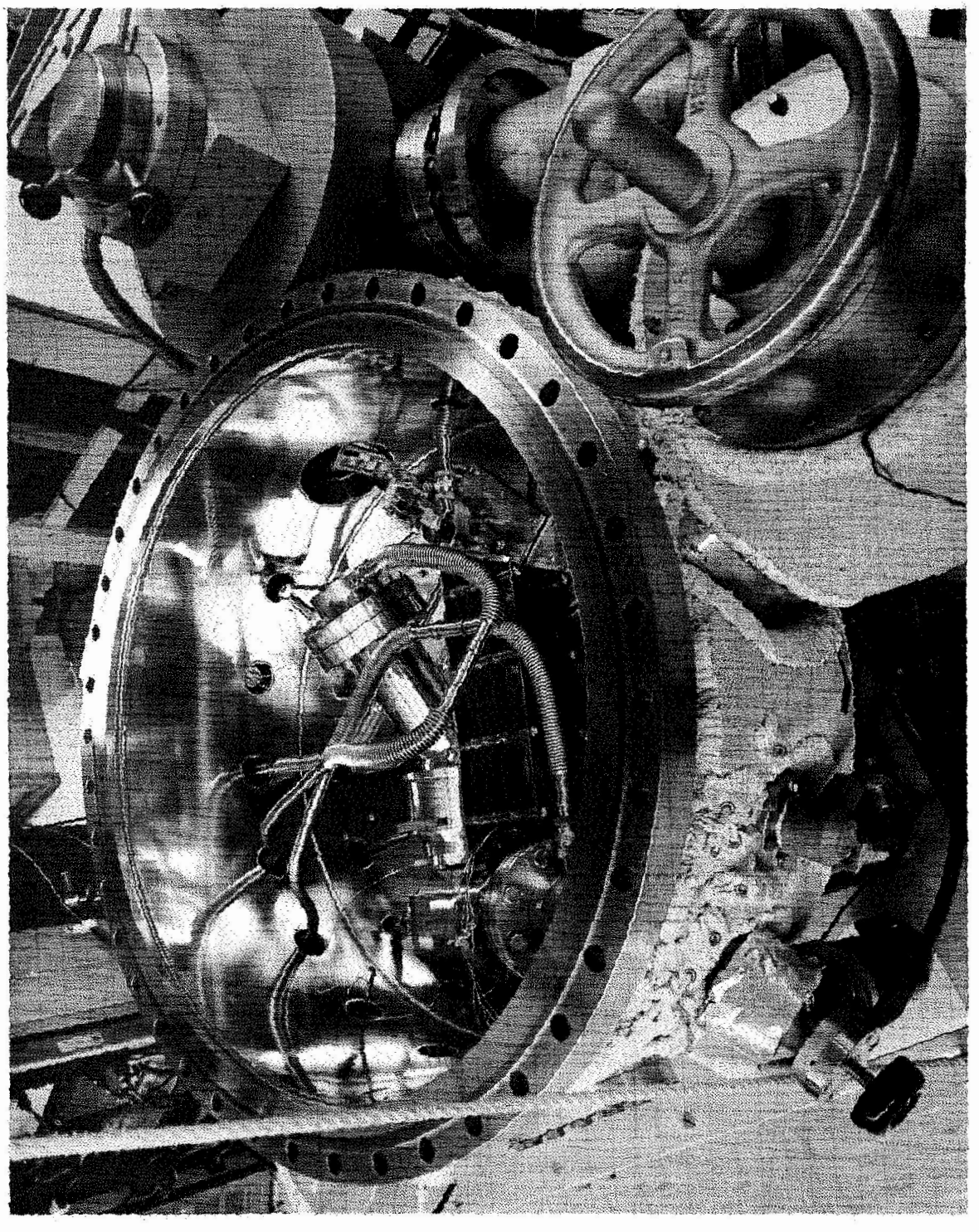

Fig. 4.2. Photograph of Apparatus for Multiply-Charged Ion Experiment.

used for accurate alignment of the slits and of the fields. A four-inch diameter magnet[41] with a field-regulated power supply provides a precise and well controlled magnetic field.

The precision alignment, which is continued through the gas cell, and the directional focusing properties of the mass spectrometer eliminate the need for a number of lenses and alighment plates usually used in an ion beam apparatus. This is especially important for satisfactory operation with a pulsed source; adjusting a number of voltages to tune for a peak would be very difficult because the pulsed output is variable. Here the magnetic and electric fields can be readily preset for a given mass peak at a given energy.

The operation of the mass spectrometer is illustrated in Fig. 4.A.1. Shown is the mass spectrum of triply-ionized Krypton from a d.c. electron bombardment ion source. The resolution is sufficient to resolve the triply-ionized mass 84 isotope of Krypton from the molecular nitrogen ion, both at mass 28. Their mass difference is 1 part in 780. With this high resolution it is possible, for example, to use the isotope Kr_{86}^{3+} at mass per unit charge equal to 28.6 for collision measurements and to avoid contamination of the triply-charged Krypton beam by other mass 28 particles. For the cross section measurement of multiply-charged carbon, the slits were widened, changing the resolution to 1 part per 100 to increase the intensity of the desired ion flux while maintaining sufficient energy and mass resolution.

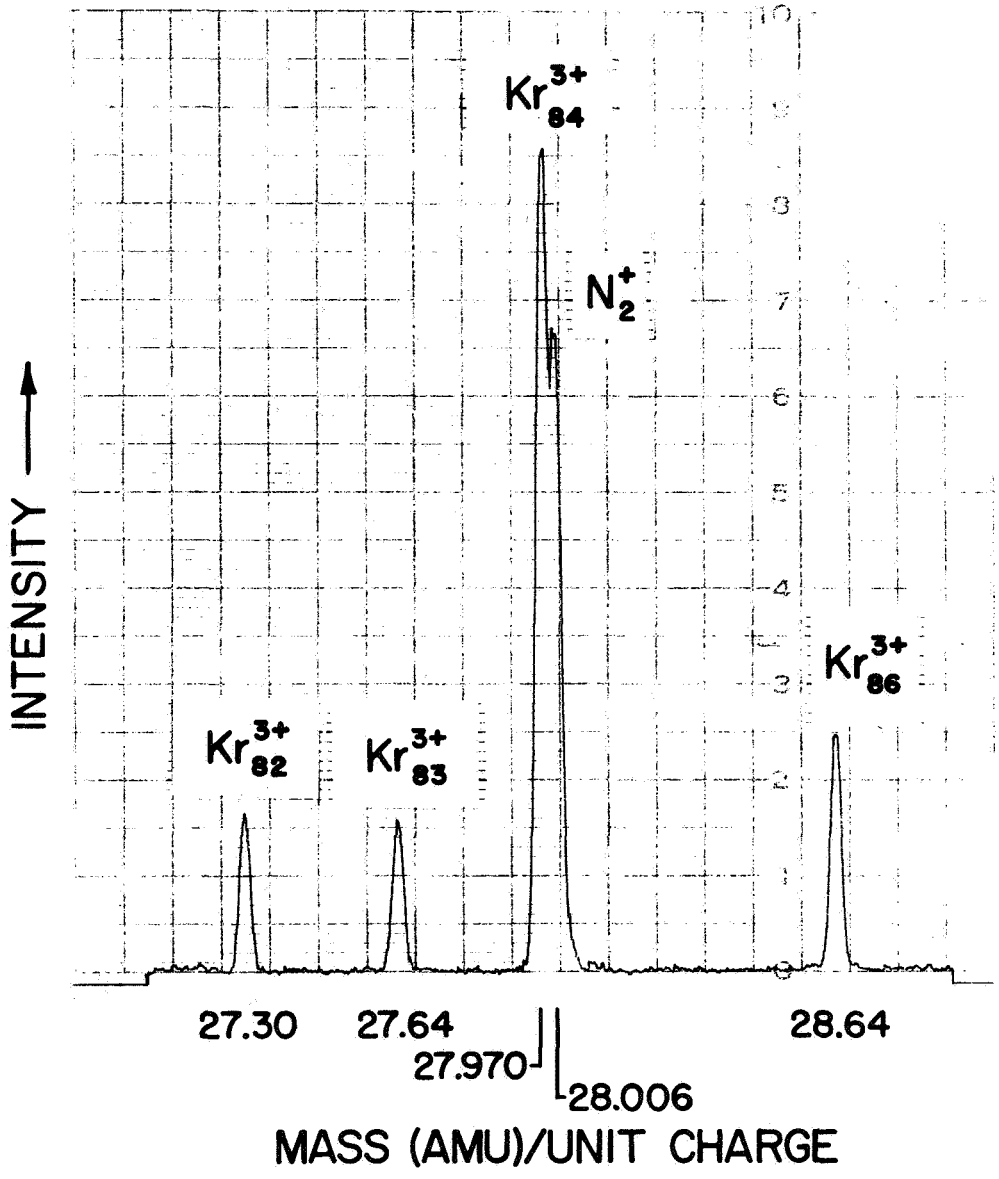

Fig. 4.A.1. Mass Spectrum of Triply-Ionized Krypton.

B. Collision Region

The collision region is formed by containing a target gas along a portion of the path of the ion beam. The gas is contained in a cell having an entrance slit (S_{en}) and an exit slit (S_{ex}) for passage of the ion beam and having an extension with an ionization gauge[42] for measurement of the gas density. A continuous inflow of gas balances the effusion from the slits. A sliding exit slit and a rotating slit (S_{rot}) farther along the path of the ion beam enable the selection of ions according to their angle of scatter in the gas cell. The relative location of the gas cell to the mass spectrometer (MS) and to the charge separator is shown in Fig. 4.B.1.

Rectangular slits are used in the gas cell. Circular apertures would simplify the considerations of angular divergence and scattering of the beam. However, rectangular slits are used in the MS and circular aperatures in the gas cell would reduce the beam flux by approximately the height to width ratio of S_{en}, which has a ratio of 25. The directional properties of the beam are considered mainly for the horizontal (XZ) plane; this is justified because the limits of allowed deviation are more restrictive in this plane for most of the particles in the beam. The dimensions of the slits in the collision region and the other apparatus are listed in Table 4.1.

Table 4.1

Slit Dimensions (units of inches)

Instrument	Location	Symbol	Width	Height	Distance from Last Slit	Remarks
Source			.5 diam			
Baffle			.125	.5	18	
MS		S_1	.0248	.250	.44	limits α_x
	entrance	S_2	.0102	.250	2.00	
	intermediate	S_3	.0969	.250	8.62	limits energy bandwidth
	exit	S_4	.0161	.250	9.07	
					22.2	
Gas Cell	extrance	S_{en}	.010	.250	2.50	
	exit (fixed)	S_{ex}	.010 to .040	.250	.500	.031 for collision measurements
	exit (sliding)	S_{ex}	.010	.250		
	rotating	S_{rot}	.010	.250	1.000	
Charge Separator	entrance	S_{in}	.553	.500	1.00	Grids on slits
	exit	S_o	.500	.625	4.84, 9.68, 14.52, or 19.36	detector entrance

The beam is directionally focused by the MS in the XZ-plane at the exit slit, S_4, of the MS. The slits S_4 and S_{en} define a maximum angular divergence of the beam in the XZ-plane. The divergence is expressed in terms of the half-angle (α), which is the deviation from a parallel position on each side of the beam. The α defined by S_4 and S_{ex} in the XZ-plane is

$$\alpha_x = \tan^{-1}\left(\frac{S_4 + S_{en}}{2L}\right) = 0.3° \qquad (4.B.1)$$

where the slit symbols also indicate their widths and where $L = 2.5$ inches is the distance between them. The cell length (ℓ) is normally 0.5 inches, so that without scatter the maximum width of the beam at S_{ex} is

$$W = S_{en} + 2(\ell \tan \alpha) \qquad (4.B.2)$$

where $\ell \tan \alpha = .0026$ inches. The slits S_1 and S_2 at the input of the MS also define an α_x, which is initially 0.5° but is reduced by the optics of the MS to about the same value of 0.3° at the MS exit. In the vertical (YZ) plane the maximum value of the half-angle, $\alpha_Y = .65°$, is determined by the height of slit S_1 on the MS, by the height of slit S_{en} on the cell, and by the distance between them.

The gas cell is precisely aligned with the MS by a projection of the cell that fits into a groove of the MS (see Fig. 4.B.1) and is clamped in position. The MS slit, S_4, also fits into this groove. The slits of the cell were machined in plates with two holes through which slide precision rods that were installed in the cell parallel to the beam. One of these round rods is machined to the cross sectional shape of a diamond with two of its opposing points rounded. The slit plates slide with a close fit on the round rod; the diamond-shaped rod through the other hole prevents rotation about the round rod. The slits are precisely machined in the slit plates with respect to the rod holes. Therefore, when the slit plates are placed on the cell body, the slits are aligned with the MS slit, S_4, and with

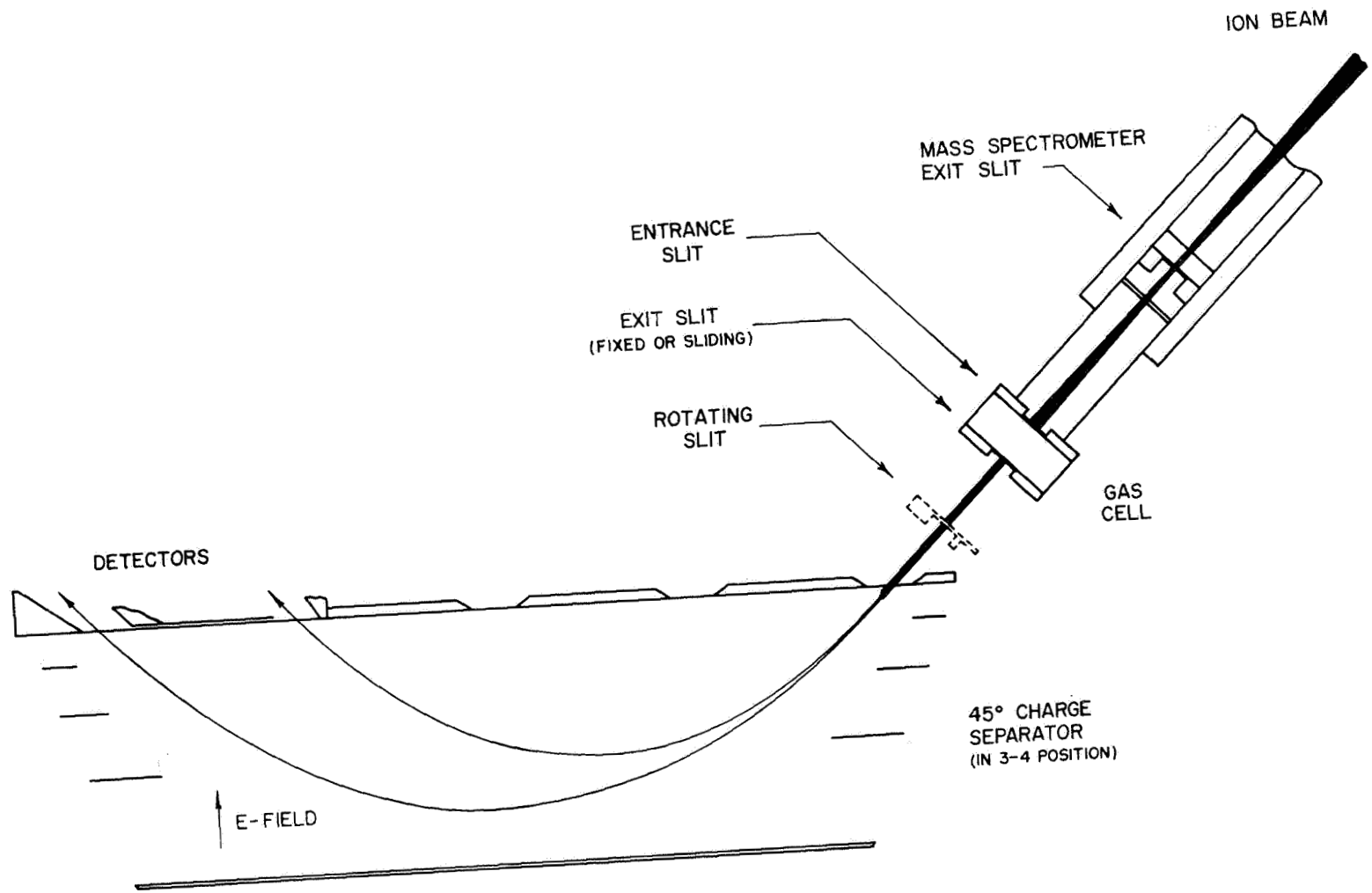

Fig. 4.B.1. Relative Location of Gas Cell to Mass Spectrometer and Charge Separator.

each other to a typical accuracy of 1 or 2 thousandths of an inch. Typical machining tolerances are given in ten-thousandths of an inch. Viton 0-ring seals are used between the slit plates and the cell body. An extension block with an additional 0-ring seal can be installed on the rods between the S_{en} plate and the cell body, thereby increasing the cell length.

The widths of the beam in the XZ-plane at the cell exit and at the rotating slit, S_{rot}, were measured by moving the respective slits to measure a slit-beam profile. The sliding S_{ex} moves perpendicular to the beam in a close-fitting groove. The S_{rot} rotates around an axis through the center of the cell. The centerline through the two moving slits, for small angles from the beam direction, is approximately the same as the line through S_{ex} and its axis of rotation, differing by only $0.46°$ at $20°$ from the beam direction. Thus, the sliding S_{ex} is a close approximation to a rotating slit at the same position for small angles of rotation.

The S_{rot} is fixed on a rotating platform that is driven from outside the vacuum chamber by a linear motion feed-through calibrated in units of .001 inch. A pin on the line between the point of rotation and the center of the S_{rot} engages a groove in the sliding S_{ex}. The range of angles of the centerline of the slits is limited to $5°$ to one side of the beam and $30°$ to the other side.

The slit-beam profiles are shown in Fig. 4.B.2. If a slit is moved across a beam of uniform density the profile is in general a trapezoid. The width of the trapezoid at 1/2 maximum is equal to the

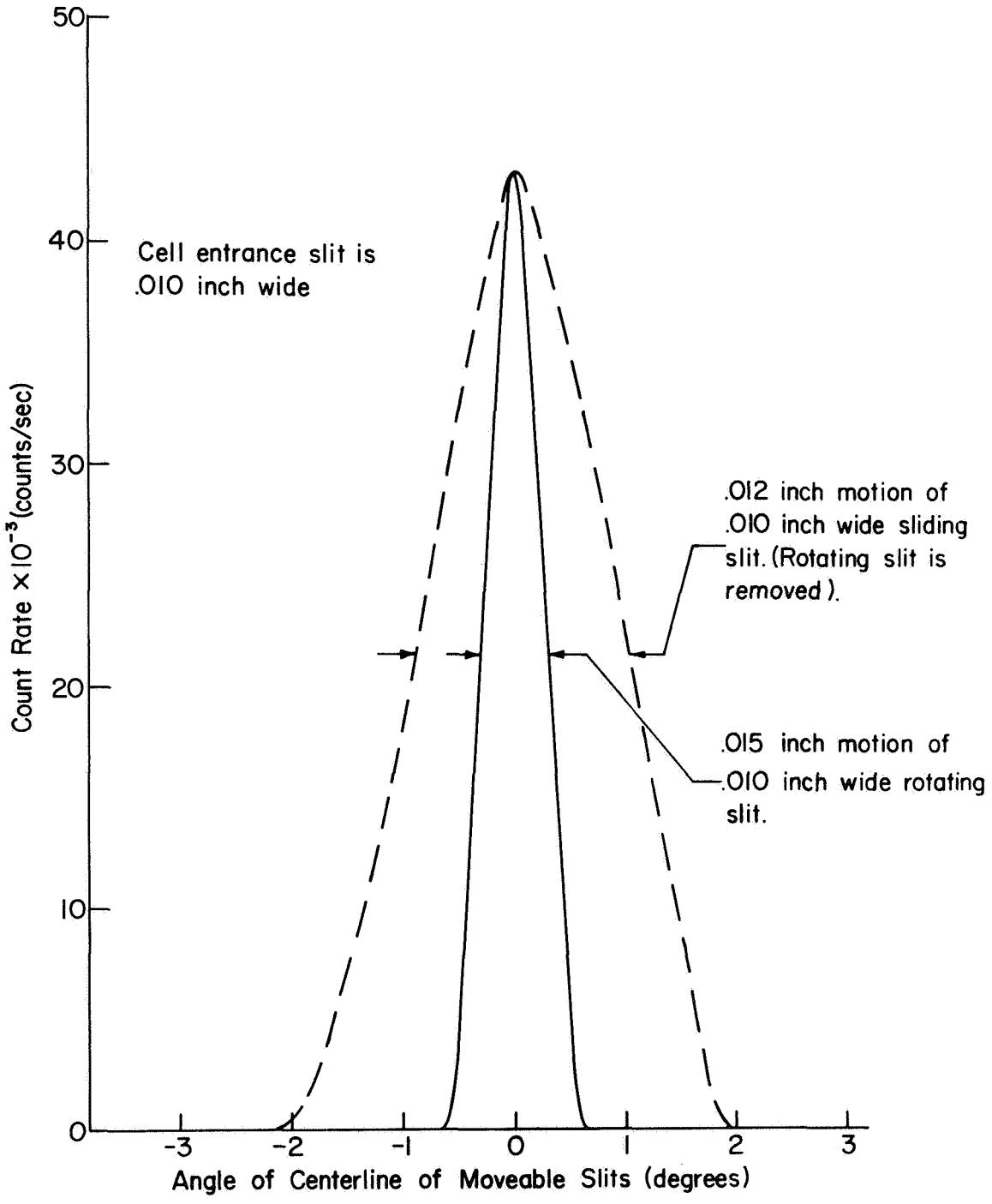

Fig. 4.B.2. Slit-Beam Profiles at Cell Exit Slit and at Rotating Slit. (Showing divergence of beam in horizontal plane).

width of the slit or the width of the beam, whichever is greater. The profile is triangular if the width of the beam is equal to the width of the slit. The slits, S_{en}, S_{ex} and S_{rot} were all .010 wide for the profiles of Fig. 4.B.2. The wider profile was made with S_{rot} removed and is the profile at the sliding S_{ex}, where 1° of rotation corresponds to .0060 inches of linear motion perpendicular to the beam. The width of the beam at the cell exit is deduced to be .012 inches. The narrower profile was made with both slits installed and is primarily a measure of the slit-beam profile at S_{rot}. The width of the beam at S_{rot} is deduced to be .015 inches using the relation of 1° of rotation equals .00219 inches of linear motion. These values of the beam width indicate a 1/2 angle divergence of about 0.15° or about a half of that given by Eq. 4.B.1. Therefore, in the XZ plane the beam is very nearly parallel. The beam input into the MS from the ion source is believed to be more divergent than $\alpha = .3°$ and, therefore, the beam is restricted in angle by the slits of the MS and by S_{en} of the gas cell, as designed.

Data on the elastic scattering of the ion beam and on the inelastic scattering with electron capture obtained with these moveable slits are presented in Chapter 5. The data does not give a differential cross section directly, and it could only be related to a differential cross section by a very complicated form factor[43]. However, these measurements of the angular scattering indicate the approximate angle inside of which all particles must be measured to obtain a total cross section.

The maximum angle, θ_m, through which a particle can scatter in the XZ-plane inside the cell and still pass through the exit slit is restricted by the width of the exit slit. The value of θ_m depends upon the X-position in the beam and upon the distance ℓ from the exit slit of the origin of the scattering. The angle, θ_m, is plotted as a function of ℓ for three X-positions in the beam in Fig. 4.B.3 for the values of $S_{en} = .010$ and $S_{ex} = .031$ used for the collision measurements.

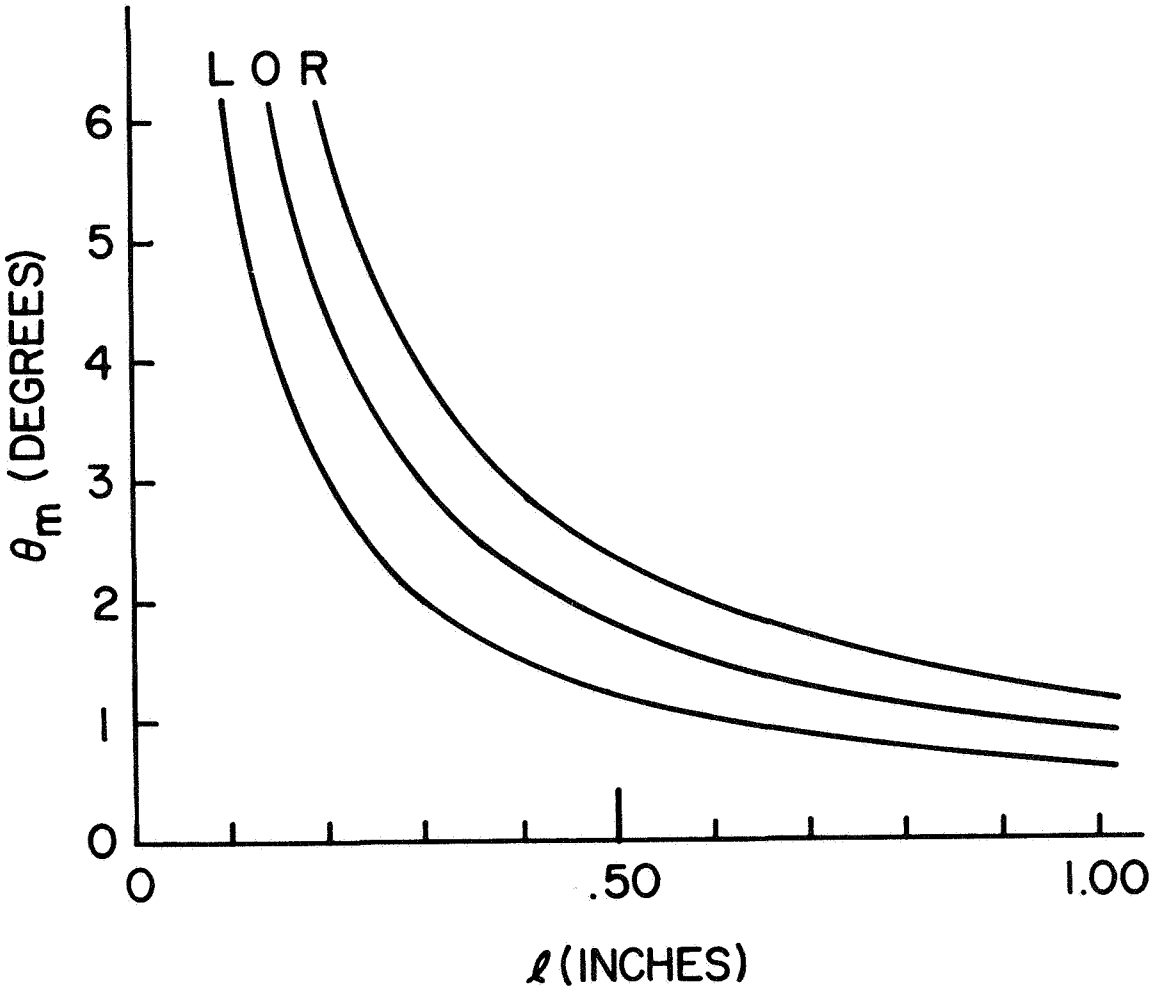

Fig. 4.B.3. Maximum Angle Ion Can Scatter in Gas Cell and Pass Through Exit Slit. (Shown as a function of point of scattering).

The beam is assumed to be parallel at S_{en}. Curve 0 is for scatter from the center of the beam, curve L is for scatter from either side of the beam away from the beam in the X-direction, and curve R is for scatter from either side of the beam through the beam to the opposite side. Particles that scatter out of the XZ-plane through angles larger than θ_m might also pass through the exit slit. The minimum value of θ_m for the value $\ell = 1/2$ that is used for the collision measurements is $\theta_m^{min} = 1°$ as can be seen in Fig. 4.B.3. Thus, nearly all particles that scatter in the cell through angles of less than 1° exit the cell as do many particles that scatter through larger angles. An additional upper limit is placed on the maximum scattering angle by the collection angle of the post-collision separator and detector system, as described in the next section.

Effusion through the slits of the cell limits the pressure ratio that can be maintained in the cell relative to the pressure in the surrounding vacuum chamber. The pressure ratio maintained is a function of the total slit area and the pumping speed on the main chamber. The pumping speed required to maintain a pressure ratio of P/P_o (ratio inside cell to vacuum chamber) is

$$S = NA = 60 \left[\frac{P\,A}{P_o\,M^{\frac{1}{2}}} \right] \qquad \text{(liters/sec)} \qquad (4.B.3)$$

where A is the total slit area in cm^2, N is the effusion rate in number of liters at P_o per cm^2 per sec, and M is the atomic mass of the target gas. A pumping speed of $S = 200$ ℓ/sec is required to

maintain a pressure ratio of 100 for Helium and for the slit sizes of $S_{en} = .010$ and $S_{ex} = .031$ which are .250 high (units in inches).

The fraction of projectile ions that capture an electron is a function of the target gas density, the cell length and the cross section as given by Eq. 5.A.5. The fraction is .0125 for the typical values of $\sigma = 3\ A^{\circ 2}$, $p = 10^{-3}$ torr, and cell length of $\ell = .5$ inches, demonstrating that the chosen length of $\ell = .5$ inches permits operation under single-collision conditions with several per cent of the particles undergoing electron capture at reasonable gas pressures.

The effective length of the target gas is actually greater than the cell length because the effusing gas causes a considerable gas density to exist in the region just outside the slits. Since the cell length is relatively short, this end effect is appreciable and is corrected for in a manner described in Chapter 5.C.

The flow of gas into the cell is controlled by a precision leak valve[41] outside of the vacuum chamber at the end of a long 1/2 inch diameter tube connected to the gas cell. Another tube, connected to the cell at right angles to the first, leads to a closed volume containing the ionization pressure gauge. The arrangement is shown schematically in Fig. 4.B.4. A capacitance manometer[44] is used to calibrate the ionization gauge for the various gases as described in chapter 5.D.

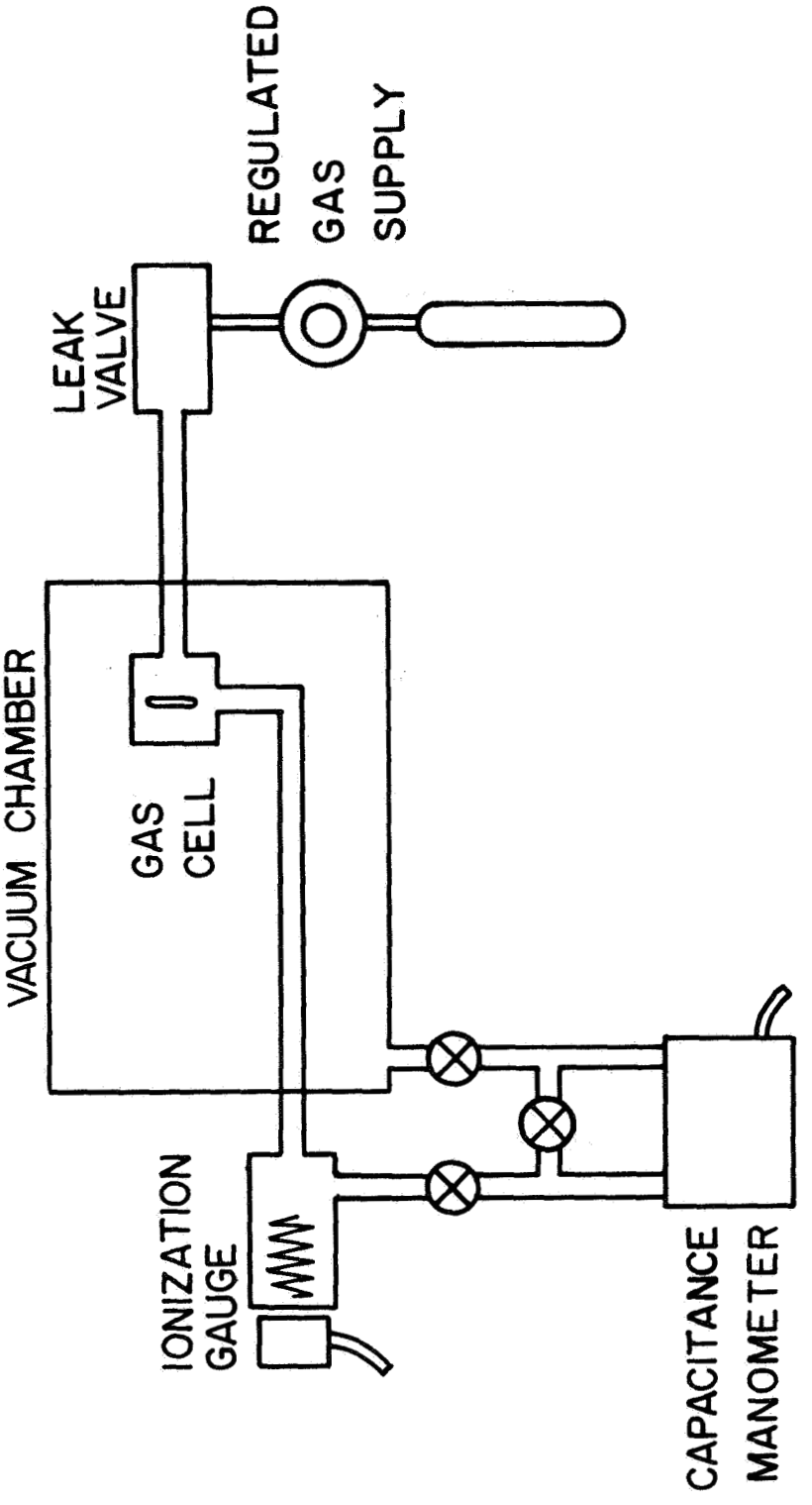

Fig. 4.B.4. Arrangement for Gas Handling and Pressure Calibration.

C. Post-Collision Charge Separator

The ions in the beam are separated according to their charge, Z , after collision, by a 45° electrostatic analyzer[45] that has first order directional focusing in the horizontal (XZ) plane (Z is the beam direction). The beam enters the electric field at an angle of 45° and follows a parabolic path in the constant electric field (see Fig. 4.B.1) according to its energy per unit charge. If the electric field has no component perpendicular to the XZ-plane, the velocity component of the particles is unchanged in the vertical plane. A converging effect in the vertical direction was added by placing horizontal plates above and below the separator at the same electrostatic potential as the end vertical plate of the separator. The electric field is then slightly concave toward the separator entrance and exit, and the field is more concave at the peak of the parabola. A test of this operation is described below.

The height of the vertical plates that form the electric field is 3.0 inches, which is about 12 times the height of the beam. The distance (d) between the entrance of the separator and the end plate is d = 3.0 inches. The three intermediate plates are at the appropriate potentials to maintain a linear field. The intermediate plates have rectangular holes that are 1.62 inches high and have a length as shown in Fig. 4.B.1.

The detectors are mounted directly at the exit of the separator with a fixed distance between them. The separator-detector assembly can be positioned to accept the beam at each of the three

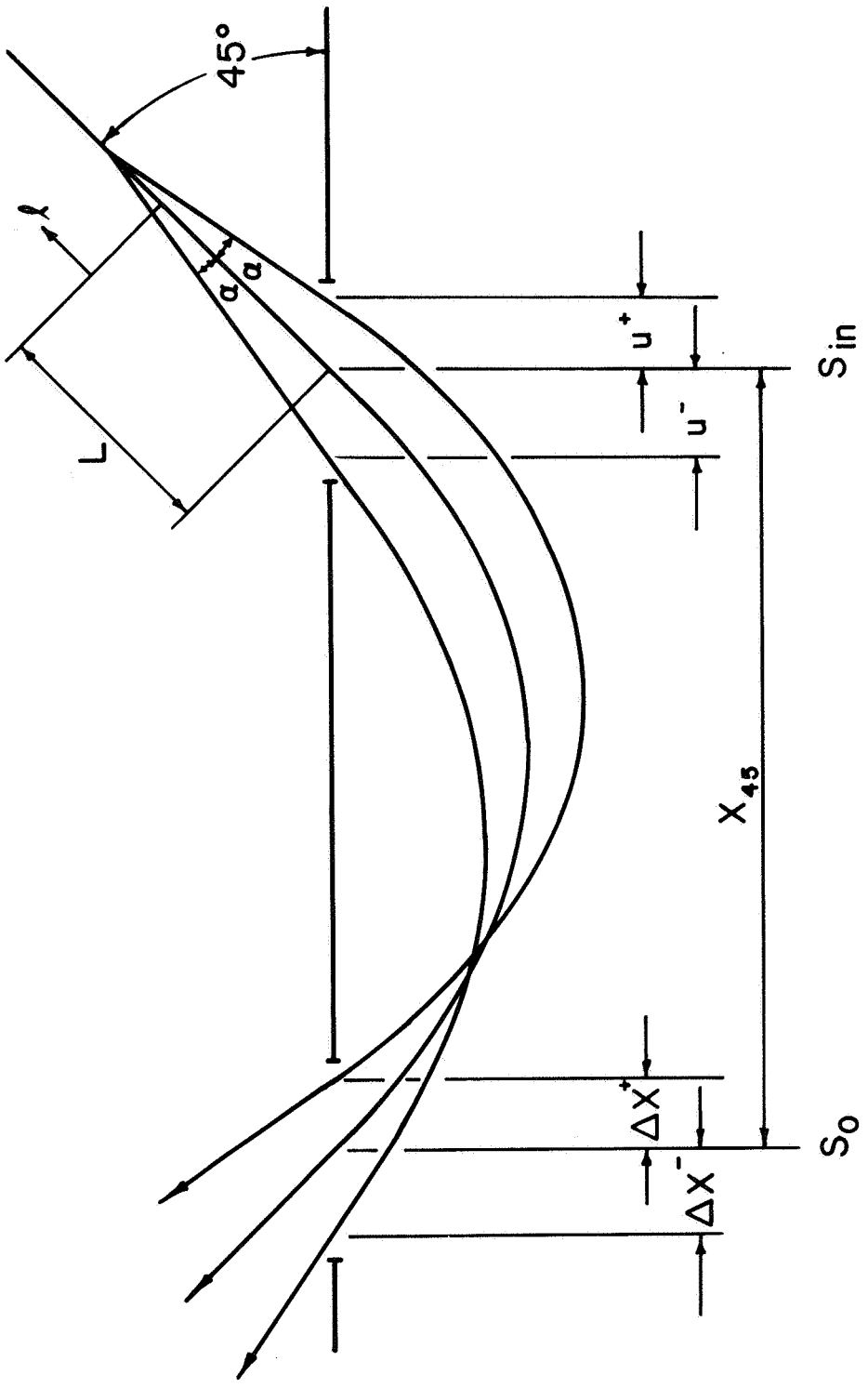

Fig. 4.C.1. Paths of Ions in 45° Charge Separator.
(Shown schematically with notation).

entrances so that particles with the charge ratios of 1:2, 2:3, or 3:4 respectively enter the detectors. The entrance slits are covered by a 95 percent transparent tungsten grid that practically eliminates the fringing field at the slit. The divergence of the beam caused by the fringing field from an uncovered slit was particularly severe in the vertical plane; tests of this are described below.

The equations that described the operation of the analyzer are summarized here. The distance, x, between the entrance point and the exit point is given by

$$x = x_{45} \cos 2\alpha \tag{4.C.1}$$

where α is the angle between the actual line of entrance to the separator and the line of entrance, which is at an angle of 45° to the electric field (see Fig. 4.C.1). The distance x_{45} is the maximum value of x, which occurs for $\alpha = 0$ ($\theta = 45°$). The directional focusing of the exit is first order in α as can be seen from the expansion of the cosine in Eq. 4.C.1.

$$x = x_{45}(1 - 2\alpha^2 + \frac{2\alpha^4}{3} - \ldots) . \tag{4.C.2}$$

The peak "height" of the parabola is

$$y_p = \frac{x_{45}}{4} (1 + \sin 2\alpha) \tag{4.C.3}$$

and the required voltage on the last separator plate is

$$V = \frac{4d}{x_{45}} \left(\frac{1}{2} \frac{E}{Z}\right) \qquad (4.C.4)$$

where d was defined and E/Z is the kinetic energy per unit charge. The value of x_{45} is the distance between the center line of the entrance slit and the center line of the exit slit. In this design, x_{45} is in multiples of 2.386 inches,

$$x_{45} = (2.386)n \qquad (4.C.4)$$

where $n = 1, 2, 3,$ or 4. The separator voltage, V_{sep}, that is theoretically required is

$$V_{sep} = \frac{2.515}{n} (E/Z) \ . \qquad (4.C.5)$$

The bandwidth of the energies of particles that can leave the separator from a beam that is narrow and parallel at the entrance is

$$\beta = \frac{100\ S_o}{x_{45}} = \frac{21.0}{n} \text{ percent} \qquad (4.C.6)$$

where S_o is the width of the separator exit slit and $S_o = .55$ inches.

The maximum angle through which a particle can be scattered in the cell and pass through the separator and into the detector is considered here, by deriving the deviations in the XZ-plane of the points at which the particle enters and exits the separator from the

corresponding points for no scattering ($\alpha = 0$). For a given maximum scattering angle, α, in the XZ plane and for a point ℓ inside the gas cell (see Fig. 4.C.1), there is a spread of the beam at the entrance slit, S_{in}, and at the exit slit, S_o, of the separator. The initial width of the beam is neglected. The deviations as a function of α at S_{in} are

$$u^{\pm} = (L + \ell)\sqrt{2}\ \frac{\tan \alpha}{1 \pm \tan \alpha} \qquad (4.C.7)$$

and the total spread at S_{in} is

$$u_{TOT} = u^{+} + u^{-} \ . \qquad (4.C.8)$$

The deviations at S_o are the sum of the deviation at S_{in} and the deviation of the trajectory in the electric field because α is nonzero, i.e.

$$\Delta x^{\pm} = u^{\pm} \pm x_{45}(1 - \cos 2\alpha) \qquad (4.C.9)$$

The total spread at S_o is

$$\Delta x_{TOT} = \Delta x^{+} + \Delta x^{-} = u_{TOT} \ . \qquad (4.C.10)$$

Thus, the spread at S_o is equal to the spread at S_{in}. The middle of the spread at S_{in} is displaced by

$$\Delta u_o = \frac{u^+ - u^-}{2} \qquad (4.C.11)$$

and at S_o is displaced by

$$\Delta x_o = \frac{\Delta x^+ - \Delta x^-}{2} = \Delta u_o + \Delta x_\alpha \qquad (4.C.12)$$

where $\Delta x_\alpha \equiv x_{45}(1 - \cos 2\alpha)$. Values of these quantities are listed in Table 4.2.

Table 4.2.

Beam Spread at Separator Exit as Function of Scattering Angle

(units are inches)

α (degrees)	Total Spread $x_{TOT} = u_{TOT}$			Displacement of Middle of Spread				
	ℓ=0	ℓ=.5	ℓ=1	Δu_o ℓ=.5	Δx n=4	Δx_o n=4 ℓ=.5	Δx^- n=4 ℓ=.5	Δx^+ n=4 ℓ=.5
.5	.049	.062	.074	-.0003	.0015	.0012	.030	.032
1	.099	.124	.148	-.0011	.0058	.0047	.057	.067
1.5	.148	.185	.222	-.0025	.0131	.0106	.082	.103
2	.198	.247	.297	-.0043	.0233	.0190	.105	.143
3	.297	.372	.446	-.0097	.0523	.0426	.143	.228
3.5	.347	.434	.521	-.0133	.0711	.0578	.159	.275
4	.398	.497	.596	-.0174	.0927	.0753	.173	.324
5	.499	.623	.748	-.0273	.1447	.1174	.194	.429
6	.601	.752	.902	-.0395	.2081	.1686	.207	.544

If the path of a particle that is not scattered were through the center of S_{in} and S_o , a particle that is scattered at the cell entrance through an angle $\alpha \lesssim 3.2°$ would also enter the detector, since $\Delta x^{\pm} < \frac{S_o}{2} = .250$. However, the spread at S_o caused by the

range of energies of the particles in the beam must also be considered, and this spread is given by (using Eq. 4.C.6)

$$\Delta x_E = \frac{\beta x_{45}}{100} \quad . \tag{4.C.13}$$

The range of energies in the beam is limited to 4 percent by the MS. The spread for $\beta = 4$ is $\Delta x_E = .382$ at the $n = 4$ position and $\Delta x_E = .286$ at the $n = 3$ position; therefore, the limit on the scatter in the XZ plane at the cell entrance is about 1° for the $n = 4$ position and is about 1.7° for the $n = 3$ position. Most of the particles that scatter less than 1° are detected, and many that scatter to larger angles are also detected. The restriction on the angle is less severe for the smaller n positions.

A test of the focusing effect (in the YZ-plane) of the plates that were added above and below the separator was made. Without the grid on S_{in}, some of the beam diverged to large vertical angles causing 30 percent fewer particles to be measured by detector, B, at the $n = 4$ position than by detector, A, at the $n = 3$ position. Adding the plates counteracted the effect of the divergence so that 8 percent more were measured in B than in A, indicating that the focusing is more effective for the $n = 4$ position. With the grid on S_{in}, the same number of particles were measured in each detector when the beam was restricted to the top portion of its height at S_{rot} (i.e. more particles with larger angles) as when it was unrestricted. The actual limit on scattering in the YZ-plane was not determined, but is estimated to be 1°.

The actual required separator voltage, V_{sep}, was determined by measuring slit-beam profiles at each of the detectors for each of the three positions of the detector-separator and for beam energies of 100 ev and 1000 ev. Two of the twelve profiles are shown in Figs. 4.C.2 and 4.C.3. The width at 1/2 max is a measure of β. The values of β derived from these 1/2 widths agree with the values given by Eq. 4.C.6 to an accuracy of ± 8 percent. The center point voltages measured are all within several precent of each other. A slightly larger center point voltage was measured for the $n = 4$ position into detector B. This position requires a more accurate setting because its energy bandwidth is the narrowest (Eq. 4.C.6). Therefore, the value chosen for the constant in Eq. 4.C.5 is the one which best fits the center point for the $n = 4$ position. The required separator voltage is thus

$$V_{sep} = \frac{2.575}{n} (E/Z) \qquad (4.C.5)$$

where the constant is 2 percent larger than the theoretical value and less than 1 percent larger than the measured value for the $n = 3$ position (with particles entering detector A). Since the energy bandwidth for the $n = 3$ position is 1.8 percent larger than that for the $n = 4$ position, the setting given by Eq. 4. C.5 is satisfactory for both detectors.

The separator voltages for the collision measurements are set at the values given by Eq. 4.C.5. For the measurement of σ_{43} the detector-separator assembly is placed in the 3-4 position (beam entrance

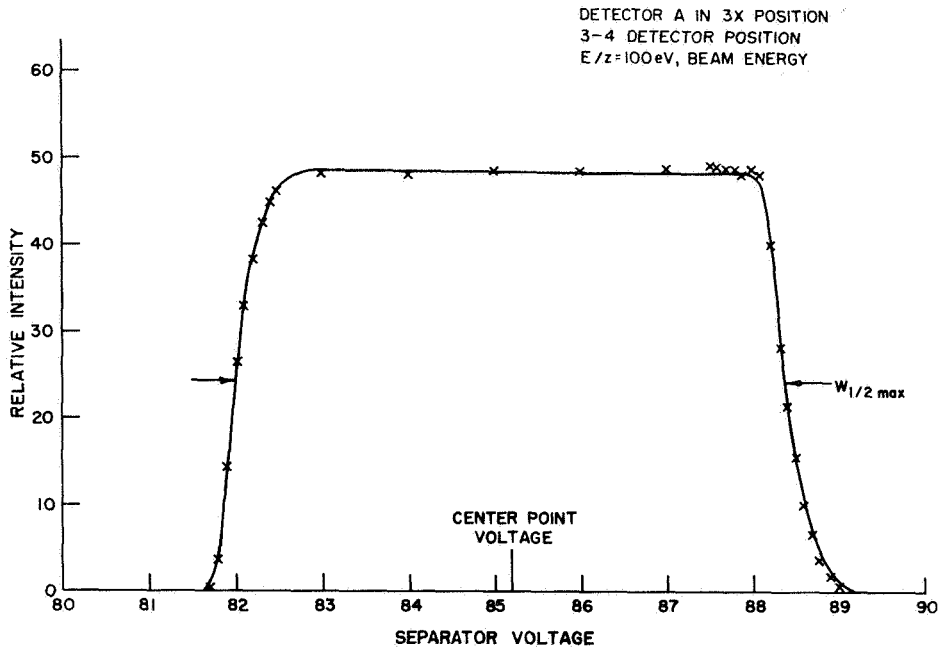

Fig. 4.C.2. Slit-Beam Profile at Detector A Entrance.
(Used to determine energy bandwidth and required voltage).

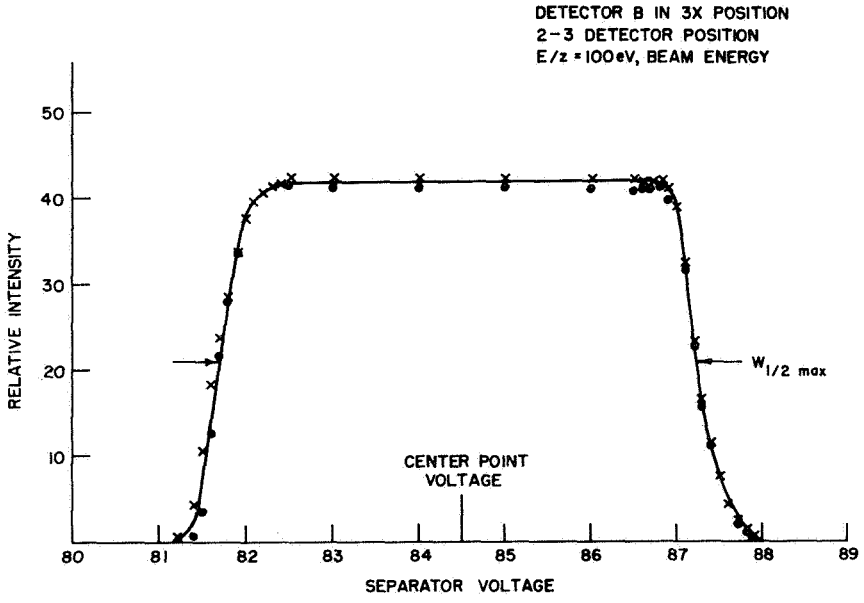

Fig. 4.C.3. Slit-Beam Profile at Detector B Entrance.
(Used to determine energy bandwidth and required voltage).

into the outermost S_{in}), so that $Z = 4$ particles enter the closest detector (A) and $z = 3$ particles enter the other detector (B) .

D. Ion Detectors

The general requirement of an ion detection system is that it measure either relatively or absolutely a quantity of ions and record the measurement as a function of the various parameters of the experiment. The requirement is divided into categories according to the rate of arrival of the ions at the detector. If the rate is sufficiently high ($\gtrsim 10^6$/sec) and approximately constant for averaging times of order of seconds, then a Faraday cage and an electrometer is a suitable detector. For lower average rates (from several per second to 10^7/sec) the effect of each individual ion can be amplified and counted. However, the pulsed output of the pulsed-discharge ion source has a high rate for a very short period of time, and the detectors must operate with a low average but high instantaneous ion input.

The problem of absolute measurement of a number of ions is avoided in this experiment because the required quantity to be measured is the number of ions in one detector relative to the number in another detector. Therefore, only a relative calibration of the detectors is required, and the accuracy of the required ratio is equal to the accuracy of relative calibration. However, the detectors must operate over a range of ion inputs greater than the ratio of the number of ions in the respective channels.

The system for ion detection consists of two Daly-type, secondary-emission detectors, designed to operate in either a pulsed

mode or a counting mode and appropriate recorders for each mode. The pulsed mode is designed to measure ions that arrive in a period of several μsecs. This mode uses a signal from the ninth dynode of the photomultiplier of the detector. The decay time of this dynode signal is long compared to the arrival period of the ions, so that the height of the signal is proportional to the total number of ions in a pulse. The dynode signal is amplified and recorded on a gated, peak-reading memory voltmeter.

The counting mode is designed to measure ions that arrive randomly at continuous, average rates up to about 3×10^7 per sec. Each individual ion produces a fast anode signal that is counted by a 100 mc. pulse counter. At higher rates the individual pulses pile-up and the counting efficiency decreases.

The simultaneous anode and dynode signals caused by a pulse of about 10^4 carbon (4+) ions are shown in Fig. 4.D.1. The rise of the dynode signal represents the arrival of the ions in the detectors. The steps on the rising portion of the dynode signal indicate that the ions arrived in several bursts. The individual fast pulses cannot be distinguished on this time scale and actually most pulses were piled-up.

The dynode signal is in effect an integral of the individual dynode ion signals which can be observed for very low ion fluxes ($\sim 10^3$/sec). The integrated, dynode signal must be calibrated to relate it to the total number of ions. The calibration can be accomplished by using the double output provided from the dynode and the anode to measure the mean dynode pulse height in a manner described in App. A, and has an estimated absolute accuracy of ±35% and a relative (one detector to another) accuracy of ±7%. A detailed description of the detectors is given in App. A.

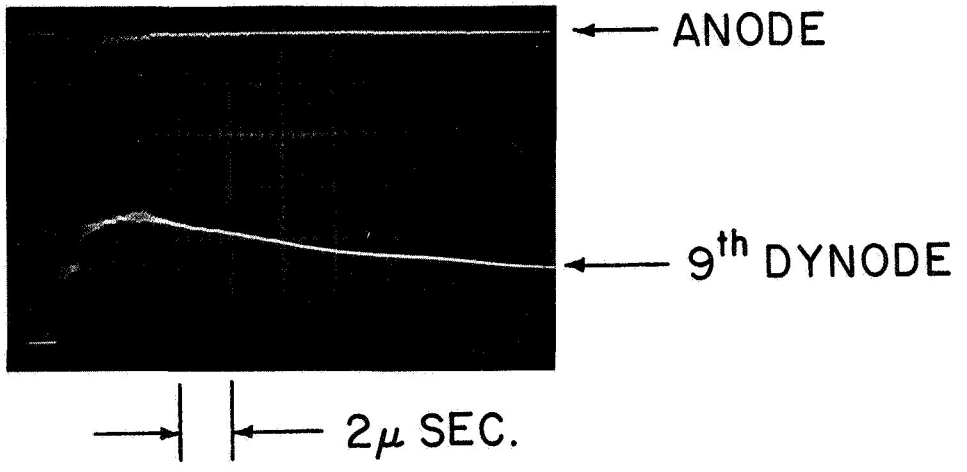

Fig. 4.D.1. Simultaneous Anode and Dynode Signals. (Caused by approximately 10^4 carbon (4+) ions).

E. Vacuum System

The essential requirements of the vacuum system are: 1) that it have a low ultimate base pressure relative to the pressure to be used in the gas cell, 2) that the gas handling capacity be sufficient to maintain the required pressure differential across the slits of the gas cell. Vacuum technology has progressed to the point where it is possible to obtain low pressures with off-the-shelf items and standard techniques, so a detailed description of the vacuum equipment is not necessary.

The general approach was to use stainless steel for the chamber and where possible for the internal components. Organic and other materials with high outgassing rates were avoided. Most of the vacuum seals were made with metal gaskets, except that Viton-A O-rings were used in the roughing valve seat, in the main chamber valve, for seals on the slits of the gas cell, and for the seal around the scintillator of the detectors. The 25-inch diameter seal on the cover of the main chamber was designed for either a Viton O-ring or an aluminum wire gasket; the unbaked base pressure was about a factor of 5 lower when the metal gasket was used. The main vacuum pump was a 6-inch, ultra-high vacuum, diffusion pump system manufactured by Consolidated Vacuum Corp. The pump was trapped by a water-cooled baffle and a bakeable sorbent trap. The plateau pumping speed of the system is approximately 400 liters/sec. Silicone DC-705 pump oil was used, and the foreline and roughing line each contained a sorbent trap. A 30 liter/sec ion pump was used to diffentially pump the pulsed ion source.

The chamber was bakeable and initially a base pressure of 10^{-9} torr was obtained with the chamber empty. Some of the components of the experiment were not bakeable: the scintillator, the photo tube and some of the precision machined parts. The ultimate, unbaked base pressure with the components installed was about 10^{-8} torr. When the collision measurements were made, the base pressure with the gas cell valve closed was typically 5×10^{-8} torr.

CHAPTER V

EXPERIMENTAL PROCEDURE

The experimental procedure for measuring the total cross section for single-electron capture is described in this chapter. The general method was described in chapter 1.B, and the design and operation of the components of the apparatus were described in chapters 3 and 4. This chapter contains descriptions of the procedures for taking data, of the analysis of the data, calibrations of the instruments, of the tests of the system, and an estimation of the accuracy of the measurements. Angular scattering measurements for several processes are included.

A. Total Cross Section

The attenuation of the initial component of the beam as it passes through a gas is given by

$$\frac{dI}{dx} = I\,\sigma N \qquad (5.A.1)$$

where I is the beam intensity (or flux) at a distance x from where the intensity was I_o, σ is the cross section for an encounter with a target particle (gas atom) resulting in a change of the projectile particle, and N is the number of targets per unit volume. There are two types of complications: 1) the primary component may change directly to other than one secondary component, and 2) cascades may

occur from one secondary component to another and to the primary component if multiple collisions take place. The general consideration of all the possible processes requires a set of coupled equations[46] involving the cross sections for all of the processes. For a given path length in the target gas, the single collision terms are proportional to the density of the target gas, and the multiple collision terms are proportional to higher powers of the gas density. The second of the above complications is usually eliminated by maintaining a sufficiently low target density so that single collisions predominate. Measurements at higher densities for which multiple collisions are probable have been made by others (e.g. Ref.47).

The cross section for the process in which the initial (i) component changes only to the j component is

$$\sigma_{ij} = \frac{1}{N\ell} \ln \frac{I_j(\ell)}{I_o} \qquad (5.A.2)$$

where I_j is the intensity of the j component at $x = \ell$ and

$$I_o = I_i(\ell) + I_j(\ell) \qquad (5.A.3)$$

If there are other possible components, k, the Eq. 5.A.2 is a good approximation provided

$$I_j(\ell) \sim I_k(\ell) \ll I_o \, . \qquad (5.A.4)$$

The Eq. 5.A.2 with the logarithm expanded is

$$\sigma_{ij}(A^{o2}) = \frac{120}{P(\mu)\ell(in.)} \left\{ \frac{I_j}{I_o} + \frac{1}{2}\left(\frac{I_j}{I_o}\right)^2 + \frac{1}{3}\left(\frac{I_j}{I_o}\right)^3 + \ldots \right\} \qquad (5.A.5)$$

which is valid even for large values of I_j if all $I_k \ll I_j$ and the cross section from j to other states is small. Usually, only the linear term is significant unless $I_j/I_o \gtrsim .1$. The gas density was expressed in Eq. 5.A.5 as a function of the gas pressure at room temperature.

The laboratory data is taken to obtain the ratio W ,

$$W \equiv \frac{I_j}{I_i+I} + \frac{1}{2}\left(\frac{I_j}{I_i+I_j}\right)^2 + \frac{1}{3}\left(\frac{I_j}{I_i+I_j}\right)^3 \qquad (5.A.6)$$

as a function of the gas pressure, p . The length, ℓ , of the gas target is the physical length of the gas cell plus the end correction described in section C. A statistically valid measurement of W is readily obtained by counting (for 1 - 10 sec) the ions in each component when the ion current is from the continuous output of the electron impact ion source used for the C^{2+} and the Kr^{3+} cross section measurements. However, one pulse at the pulsed-discharge ion source that is used for C^{4+} is usually not sufficient to obtain a good measure of W . Variations in the measured values of W occur because the number of particles, n , in the intensity, I_j , of the secondary component is usually statistically small and because the density of the target gas may fluctuate from pulse to pulse. The expected error[48]

in the ratio measured for one pulse yielding n product ions is

$$E \lesssim \frac{100\ \%}{\sqrt{n}} \tag{5.A.7}$$

with a probability of .68 (one standard deviation). Therefore, if there are $n = 100$ particles in I_j the measured value of W is within 10% of the actual value of W with a probability of .68 (or within 20% with a probability of .95, etc.). When K measurements of W are made for K pulses of the ion source and averaged $(\text{WBAR} \equiv \sum_1^K W_i/K)$, the fractional standard deviation[49] of the measured mean (WBAR) is

$$\text{SIG WBAR} = \left\{\frac{\sum(W_i - \text{WBAR})^2}{K(K-1)}\right\}^{\frac{1}{2}} \left(\frac{100}{\text{WBAR}}\right) \text{ percent} \tag{5.A.8}$$

which decreases as the number of measurements, K. The actual value of W is within the range, $W_{\text{measured}} \pm \text{SIG WBAR}$, with a probability of .68.

Usually, 20 measurements were made at each of $J = 5$ values of the pressure. The data were recorded on a key punch format, and the entire data analysis was made with a computer routine. The values of the standard deviation of the mean, WBAR, were typically 7 percent at each pressure point and were smaller at the larger pressures. A least squares linear curve fit of WBAR as a function of pressure was made with each point weighted in inverse proportion to the value of WBAR. This weighting tended to force the curve through the value of

the base pressure. The weighted fit considers the square of the deviation of each point from the computed curve relative to the value of the point, i.e. a fractional rather than an absolute deviation. The formula for the slope of the weighted fit is

$$\text{SLOPE} = \frac{\text{SV}\cdot\text{SVXY} - \text{SVX}\cdot\text{SVY}}{\text{SV}\cdot\text{SVXX} - (\text{SVX})^2} \tag{5.A.9a}$$

and the Y-intercept is

$$C = \frac{\text{SVY} - \text{SLOPE}\cdot\text{SVX}}{\text{SV}} \tag{5.A.9b}$$

where the weights of the I^{th} pressure point are

$$V(I) \equiv \frac{1}{\text{WBAR}(I)} \left\{ \frac{J}{\sum \frac{1}{\text{WBAR}(I)}} \right\} \tag{5.A.9c}$$

are defined so that

$$\text{SV} \equiv \sum V(I) = J$$

and where

$$\text{SVX} \equiv \sum V(I) \cdot P(I)$$

$$\text{SVY} \equiv \sum V(I) \cdot \text{WBAR}(I)$$

$$\text{SVXY} \equiv \sum V(I) \cdot P(I) \cdot \text{WBAR}(I)$$

$$\text{SVXX} \equiv \sum V(I) \cdot P(I) \cdot P(I)$$

and the summations are over the values of $I = 1$ to $I = J$. The computed curves of WBAR versus pressure are plotted in Fig. 5.A.1. for two values of the energy and for the σ_{43} cross section of C^{4+} + He. The error bars are at plus and minus SIGWBAR(I) of each WBAR(I), and the averages of the SIGWBAR(I) over each set of 5 points are shown. The distributions of the W's are given in the histograms of Fig. 5.A.2 for each of the pressure points.

A measure of the linear curve fit is the standard deviation of the slope,

$$\text{SIGSLOPE} = \left\{ \frac{\text{SVDYDY}}{(J-2) \cdot \left(\text{SVXX} - \frac{(\text{SVX})^2}{\text{SV}}\right)} \right\}^{\frac{1}{2}} \left(\frac{100}{\text{Slope}} \right) \text{ percent} \qquad (5.A.10a)$$

where

$$\text{SVDYDY} \equiv \sum \text{V(I)} \cdot \{\text{WBAR(I)} - \text{P(I)} \cdot \text{SLOPE} - \text{C}\}^2 \qquad (5.A.10b)$$

The quantity SIGSLOPE includes a measure of the inaccuracy of the fit caused by the deviations of the values of the measured WBAR(I) from the true mean values, and a measure of the non-linearity, if any, of the curve through the true mean values. The values of the standard deviation of the slope, SIGSLOPE, are usually about the same as the value of the average SIGWBAR(I), or slightly less. A computer print out is made of all the quantities for each energy point at which data is recorded. The cross sections are given as a function of energy in chapter 6 with error bars representing the standard deviations of the

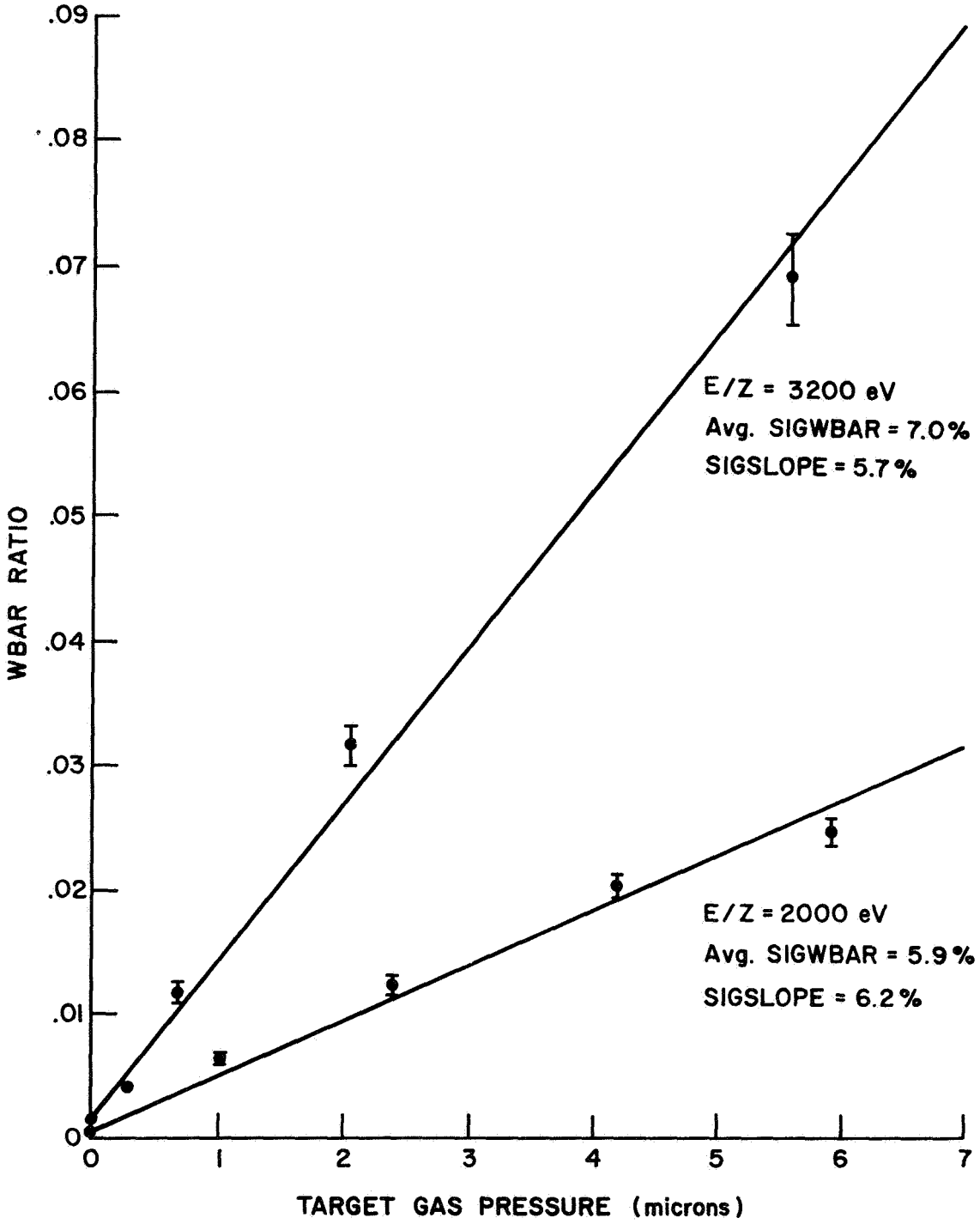

Fig. 5.A.1. Ratio of Secondary Component to Incident Flux. (Showing standard deviation of the mean at each pressure point).

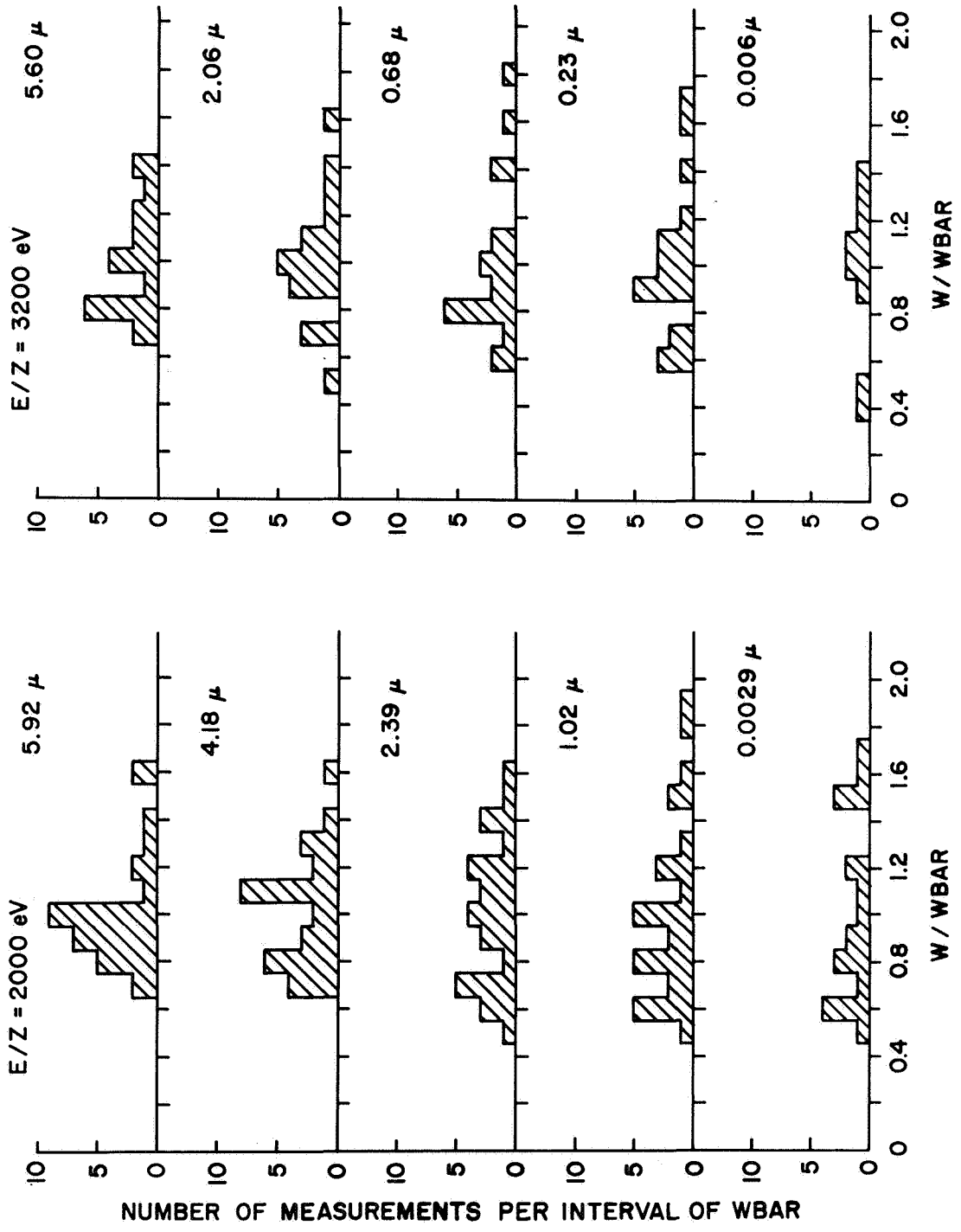

Fig. 5.A.2. Distribution of Ratio W About Its Mean.

slope, SIGSLOPE. Curve fits for the C^{4+} cross section data are made to various power of the velocity with an Omnitab[65] computer program.

B. Angular Scattering Measurements

Angular scattering measurements have been made for several processes and are shown in Figs. 5.B.1, 5.B.2 and 5.B.3. These measurements indicate the relative amounts of elastic scattering and inelastic scattering with electron capture. The acceptance angle of the moveable slits is relatively wide as indicated by $W_{\frac{1}{2}max}$ (cf. chapter 4.C). The profiles indicate that most of the collision products are scattered in the forward direction in the laboratory. The scattering is to smaller laboratory angles for Kr^{3+} + He than it is for C^{2+} + Ar , partly because of the different factors for the center of mass to laboratory transformation of the angles. The C^{2+} + Ar results indicate more scattering to larger angles at the lower energy as might be expected. The C^{2+} + Ar results at 1000 ev are also shown in Fig. 5.B.4 on a linear scale.

Measurements of the single-electron capture cross section for C^{2+} + Ar have been made for three different restrictions on the angle that a particle can scatter and still leave the collision region (see chapter 4.C). These results are shown in Fig. 5.B.5. The measured cross sections are several per cent less when the width, S_{ex} , of the cell exit is restricted to .010 inch compared to the

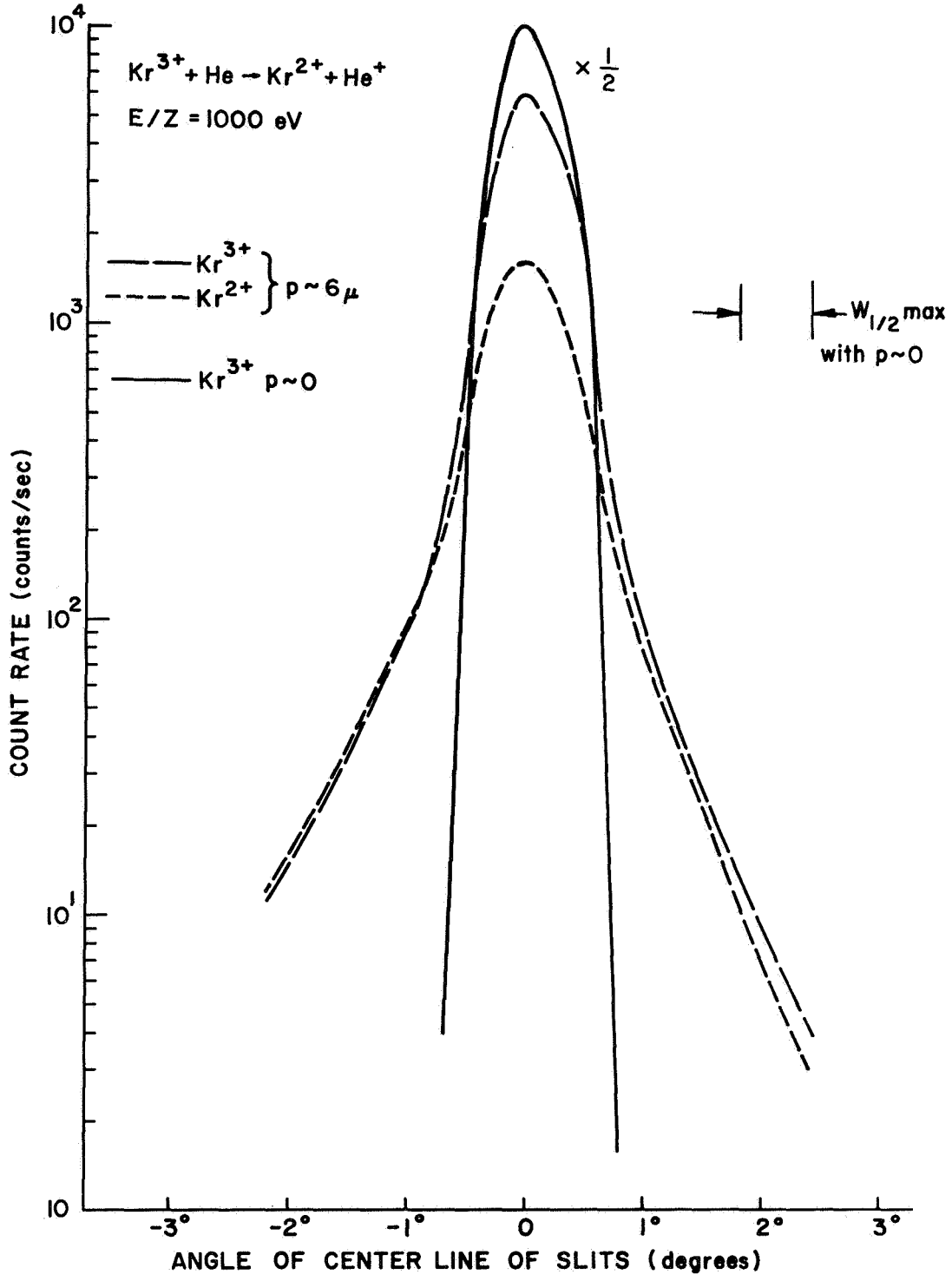

Fig. 5.B.1. Angular Scattering of Kr^{3+} in He at 1000 ev.

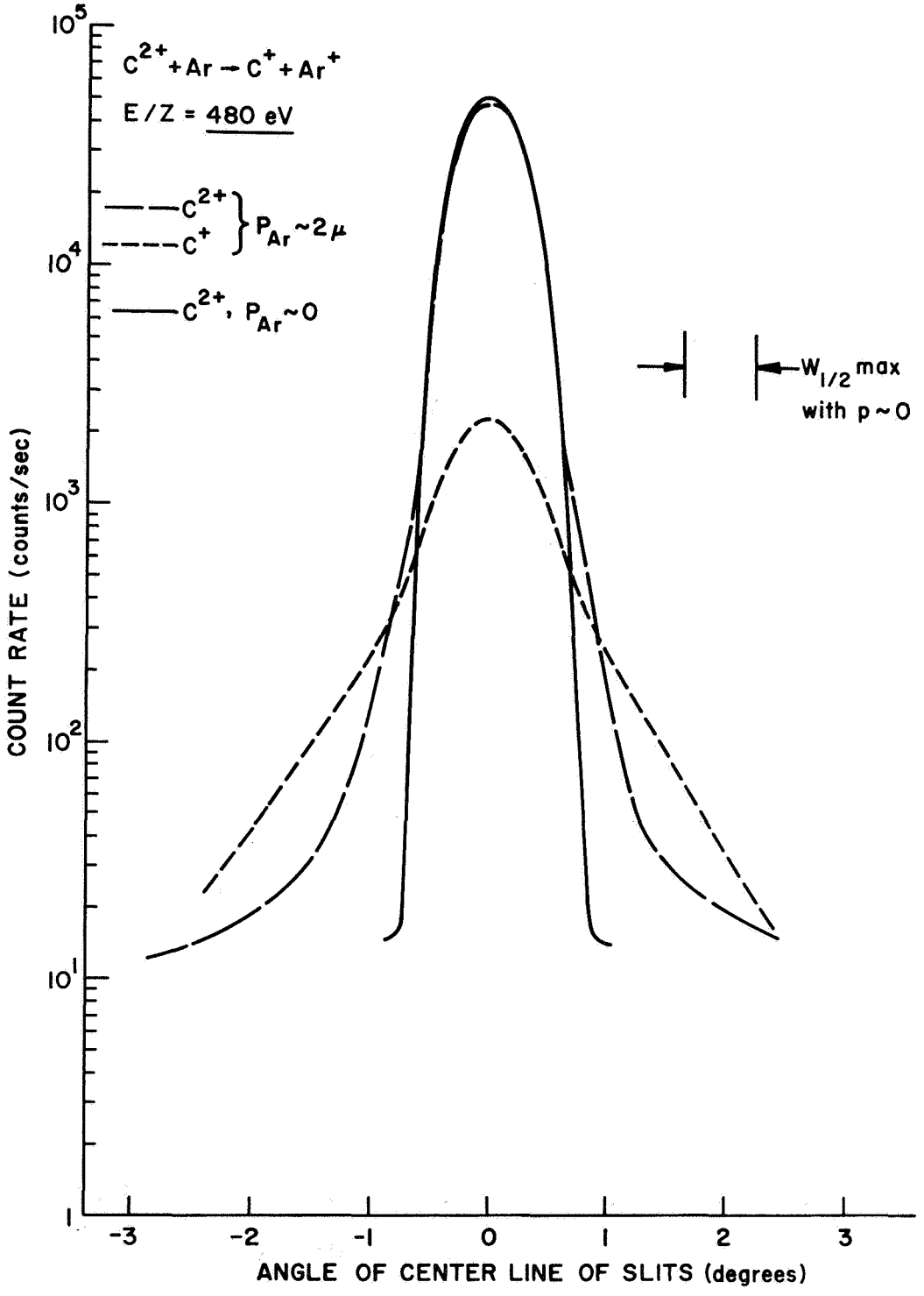

Fig. 5.B.2. Angular Scattering of C^{2+} in Ar at 480 ev.

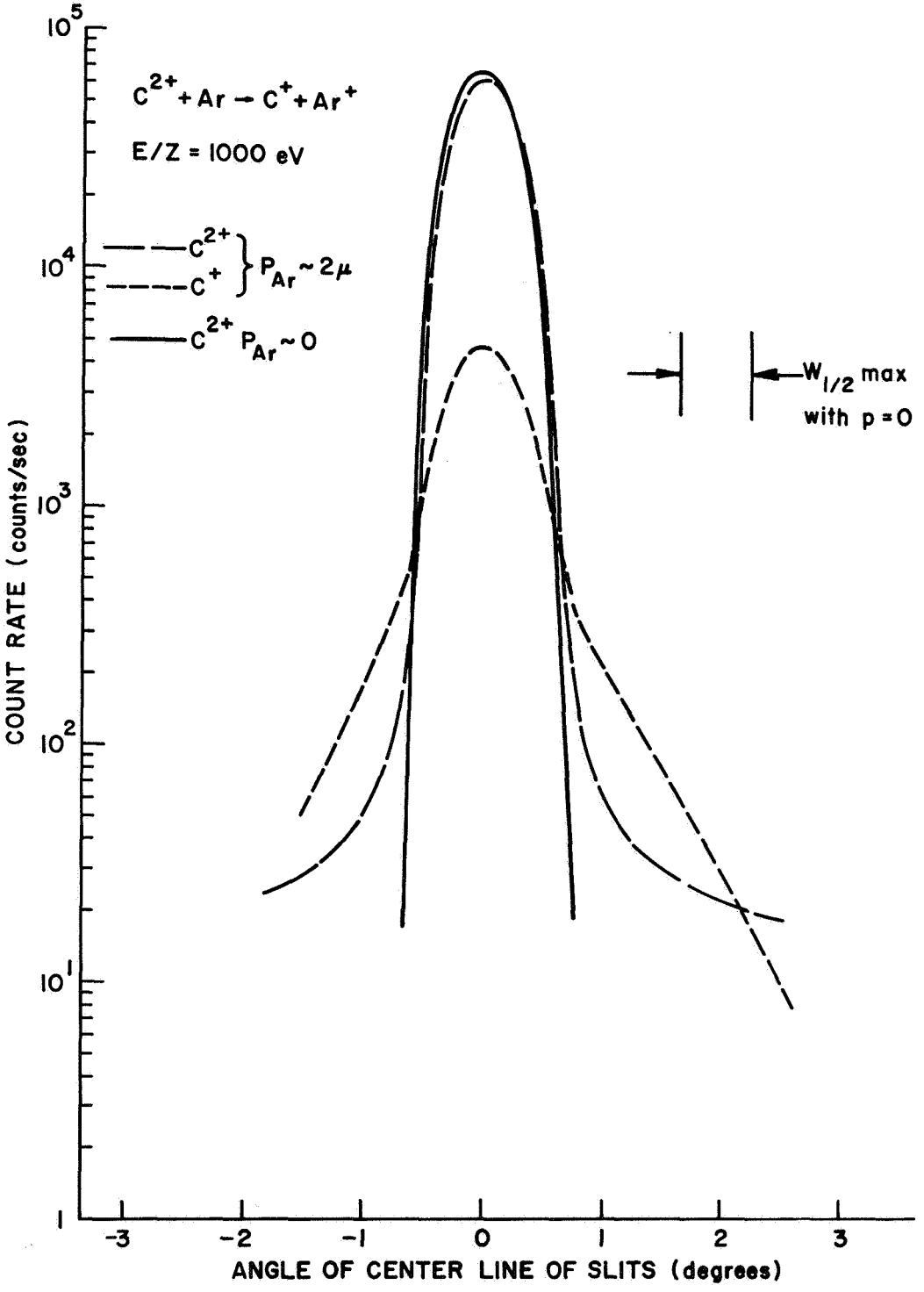

Fig. 5.B.3. Angular Scattering of C^{2+} in Ar at 1000 ev. (Logarithmic scale).

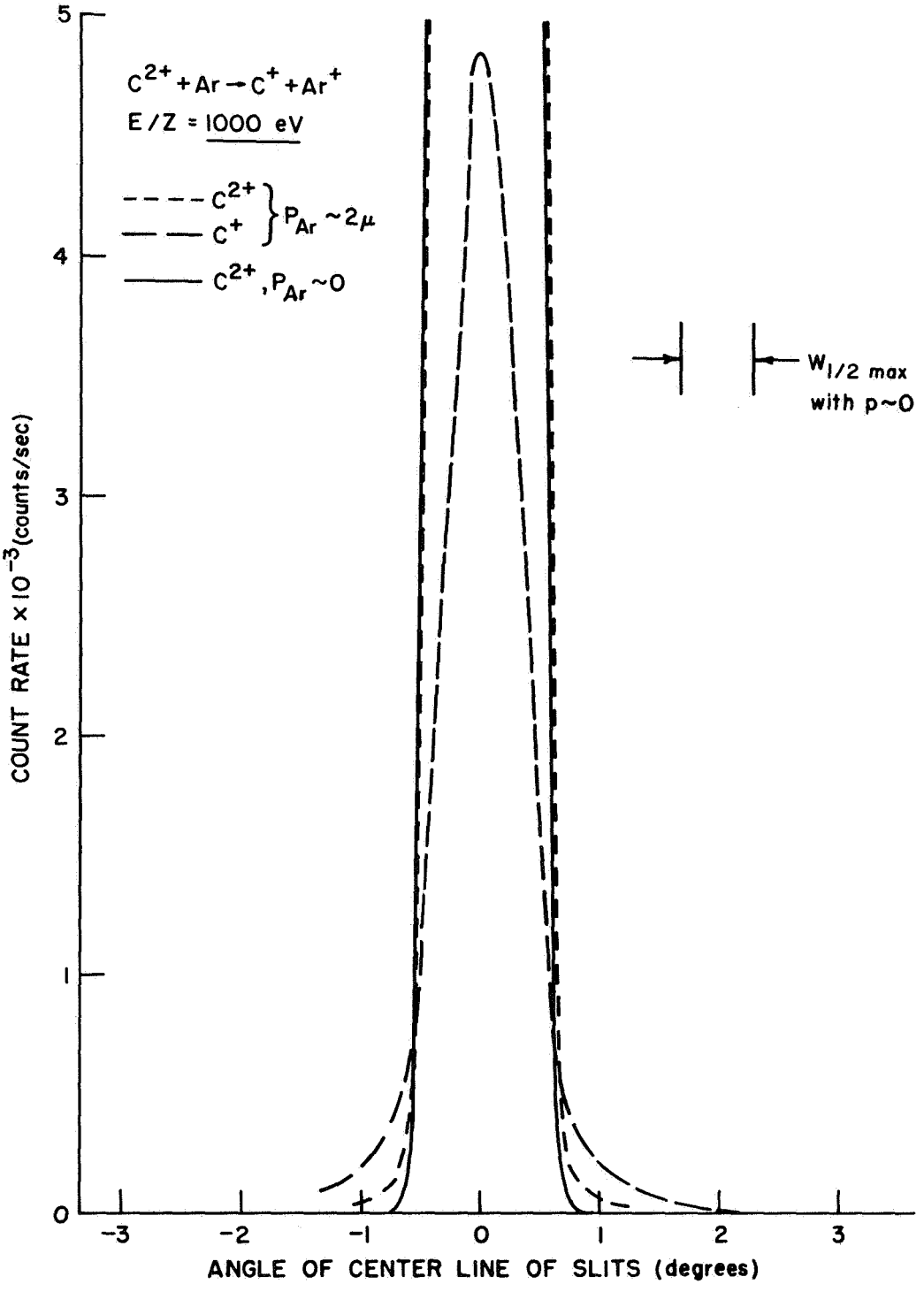

Fig. 5.B.4. Angular Scattering of C^{2+} in Ar at 1000 ev. (Linear scale).

measured cross sections when the cell exit is .031 inch wide (rotating slit not installed). When the angle of allowed scatter is more severely restricted by adding the rotating slit, there is a significant change in the measured cross section. These results indicate that the collection of scattered particles, using $S_{ex} = .031$ inch, is satisfactory for the measurement of the $C^{2+} + Ar$ cross section.

A series of cross-section measurements, similar to those of Fig. 5.B.5, for $C^{2+} + Ne$ with $S_{ex} = .020$, .013 , and .040 give a set of three nearly parallel curves for the cross section in the energy range of 500 ev to 2000 ev. The measured cross section increases about 3 per cent for each .010 inch of slit width. A slight increase is expected because of the increased end effect, caused by effusion from the larger slits. Measurement of the total correction for the end effect with $S_{ex} = .031$ is described in the next section.

C. Gas Cell End Correction

The effusion of the target gas through the entrance and exit slits of the gas cell causes the effective length of the target to be longer than the physical length (ℓ) of the cell. Expressing this end effect as an additive factor to ℓ , gives

$$L = \ell(\text{cell}) + \ell_s \qquad (5.C.1)$$

where

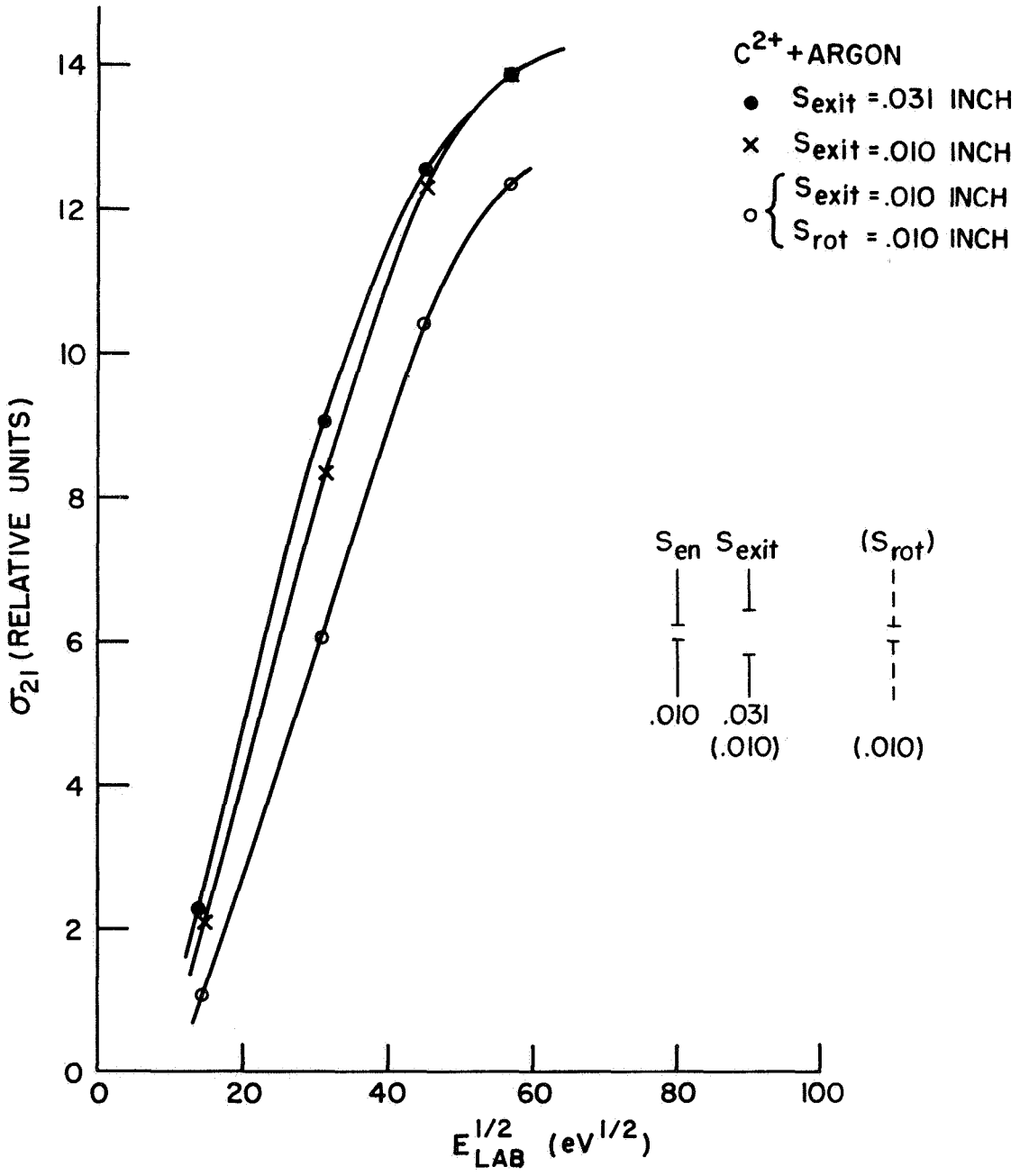

Fig. 5.B.5. Measured Cross Sections for Several Widths of Gas Cell Exit Slit.

$$\ell_s \equiv \ell_{en}(S_{en}) + \ell_{ex}(S_{ex}) \ . \qquad (5.C.2)$$

The actual cross section is

$$\sigma = \frac{k}{(\ell + \ell_s)} \quad W' \qquad (5.C.3)$$

where W' is the W of section A per unit of gas pressure. The value of ℓ_s is determined by measuring $W'(\ell)$ for two values of ℓ, and is given by

$$\ell_s = \frac{W'_1\ell_2 - W'_2\ell_1}{W'_2 - W'_1} \ . \qquad (5.C.4)$$

Measurements of the W' quantities were made for the processes $Kr^{3+} + He$ and $C^{2+} + Ar$ at two values of the length, $\ell = .500$ and $\ell = 1.000$ (inches), with the slit widths of $S_{en} = .010$ and $S_{ex} = .031$ (inches). The resulting value of ℓ_s was $\ell_s = .161$ inches with an estimated accuracy of ± 10 percent. This value of ℓ_s is about four times the slit width. The end correction is 32 percent of the cell length for a length of $\ell = .500$, and the accuracy in the measurement of ℓ_s corresponds to about ± 3 percent accuracy in the measured cross section.

D. System Tests and Calibrations

Most of the operational tests of the system are described in chapter 4 as they pertained to the design and operation of the various

components. A test of the effect of the fringing magnetic field from the mass spectrometer on the operation of the detectors is described here. This test could not be made with an ion input to the detectors, because a flux of ions could not be controlled independently of the magnetic field, B. However, a source of light from the ionization gauge of the vacuum chamber was controlled to produce countable pulses from the detectors. The electrostatic separator was used to prevent the many stray ions produced by the ionization gauge from also entering the detectors. The discriminator level of the pulse counters was set to count pulses above some minimum level. A decrease in the gain of the photomultiplier tubes, which are sensitive to fields of order one gauss, would be indicated by a decrease in the count rate. The results for the larger values of B are shown in Fig. 5.D.1. Note that the loss of counts is approximately zero up to very large values of B. The loss of counts begins to rise sharply above 9 kG, at which point the fringing field also increases as evidenced by the departure from linearity of the matnetic current versus B. The loss in detector A is larger than in detector B because detector A is closer to the magnet. The value of B used for the collision measurements was always less than 5 kG, for which the shielding of the photomultipliers is satisfactory.

In order to preset the value of the B-field in the mass spectrometer so that a given mass per unit charge, M, at a given energy per unit charge, V, is selected, the field control unit must be calibrated to an accuracy of several tenths of a percent, which is small compared to the mass resolution of 1 percent. The field-regulated control unit is calibrated by measuring the magnetic field that is required to select a series of known masses. This procedure determines

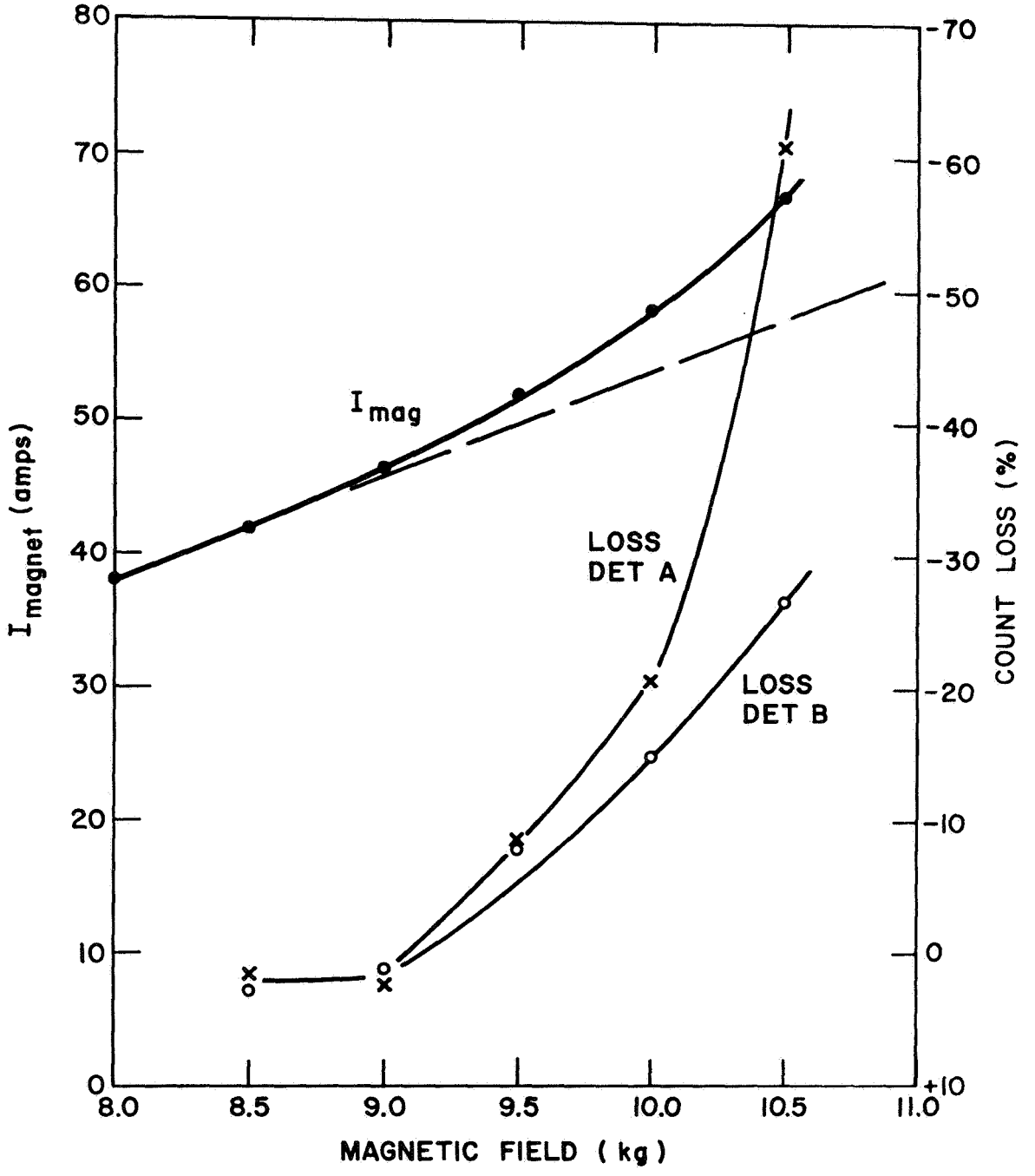

Fig. 5.D.1. Effect of Fringing B Field on Detector Gain at Large Values of B Field. (B < 5 kG was used for collision measurements).

the constant of proportionality between the dial indicated value of B and the value of $\sqrt{MV}$ for a series of M values. A zero offset adjustment and an adjustment of the constant of proportionality between the dial-indicated value of B and the actual value of the B-field permit a calibration of the control unit to the relation

$$B = 22.758 \sqrt{MV} \quad \text{gauss.} \tag{5.D.1}$$

The value of the constant in Eq. 5.D.1 was determined by an initial calibration of the B-field versus a nuclear magnetic resonance instrument. The relation of B to M was valid over the mass range of 1 to 130 amu to an accuracy of ±0.1 percent. The two voltage supplies for the electric field of the mass spectrometer were calibrated to a similar accuracy.

The peak reading memory voltmeters[50] have a rated accuracy of ±3 percent of the full scale reading. One meter was used for each of the two ion detector outputs. The absolute accuracy of the two meters was determined to be ±3 percent of the true d.c. input voltage, as compared to a digital voltmeter, for readings above 25 percent of full scale. The relative accuracy of the meters in their gated, a.c. mode was compared by feeding a 50 μsec signal of variable amplitude to both detectors. The difference between the readings on the two meters was less than ±1 percent, except at the lower portion of the meter scale for which the difference was less than 1 percent of full scale. The same comparison of their a.c. accuracy was made with the preamplifiers in the input circuit, in order to calibrate the preamplifiers to the same accuracy. This a.c. calibration test was repeated at intervals through the data

recording period. The accuracy remained constant so that a recalibration was not required. The accuracy of the measurement of the amplitude of the detector signals for the cross section measurements is estimated to be ±3 percent.

The ionization gauge[42] used to measure the target density in the collision region was calibrated against a capacitance manometer,[44] as shown in Fig. 4.B.4. This calibration was made daily after the cross section measurements. Since the vacuum chamber was used for the reference pressure of the capacitance manometer and the pressure in the chamber increases as the gas cell pressure increases, a correction factor dependent upon the total area of the slits of the gas cell was determined and applied to the calibration. The capacitance manometer was compared to a Mcleod gauge and the results of this comparison for several gases were consistent with other results[51]. The limits of the accuracy of the calibrations of the ionization gauge are estimated to be ±2%.

An estimate of the combined limits of the experimental accuracy is made here by simply summing the limits of the accuracy of the individual components. It is assumed that all systematic errors have been eliminated and that there is no significant loss of particles caused by large angle scattering of the collision products. The separate limits are: gas cell end correction, ±3 percent; pressure calibration, ±2 percent; detector gain calibration, ±7 percent; and the voltmeter-preamplifier calibration, ±3 percent. The total limit

of accuracy is ±15 percent. The combined limit is ±10% for the counting mode of the detector operation because the counting efficiencies of the detectors are the same within ±2% . In the pulsed mode this limit does not include the inaccuracy of each individual measurement as reflected by the error bars (standard deviation) on each of the cross-section data points. These standard deviations of each point are typically 7% and the effect of these deviations is reduced by the number of data points taken as a function of energy.

CHAPTER VI

RESULTS AND CONCLUSIONS

The total cross section results for single-electron capture are presented in this chapter and are discussed in terms of the adiabatic potential energy curves for the electronic states that are involved. As discussed in chapter 2, previous theoretical and experimental studies have provided qualitative information about the nature of these cross sections. However, the completeness and accuracy of this qualitative description is uncertain.

Each combination of projectile and target has a different set of electronic states and crossing points. Usually, more than one pair of states can be involved during a collision, and the interpretation of the results is arbitrary or ambiguous if all the pertinent states are not considered. For example, similar results might be expected for capture of C^{4+} from each of Helium, Neon, and Argon if only the ground electronic states are considered, since the energy defects between the initial and final ground states are 39.9 ev, 42.9 ev, and 48.7 ev, respectively. However, the measured cross section for capture from Argon is considerably larger than that from Helium or Neon and varies less as a function of relative velocity.

The measured, total cross section for single-electron capture includes possible contributions from the combined processes of single-electron capture with target excitation or target ionization, as discussed in chapter 1.B, in addition to the ordinary single-electron capture contribution.

A. Krypton (3+) on Helium

The experimental results for the total cross section for single-electron capture of Kr^{3+} from Helium are given in Fig. 6.A.1. The cross section is an increasing function of velocity in the range of measurement, and no clear maximum value at the cross section can be discerned. Also shown in Fig. 6.A.1 are the previous experimental results of Hasted and Chong[16] who used the method of slow ion collection and several cross-section functions from the empirical use of the L - Z theory as described in chapter 2.B. If the double-electron capture cross section (σ_{31}) is not small, it could account for the difference in the experimental results, since the method of slow ion collection actually measures[18] ($\sigma_{32} + 2\sigma_{31}$) .

A comparison between the previous experimental results and an approximate theoretical calculation[18] of ΔU_x has been made by Hasted and Hussain[18] in the manner of method 4 of chapter 2.B. They consider capture into the ground state of Kr^{2+} with the projectile Kr^{3+} also being in the ground state and calculate a value of $\Delta U_x = 1.17$ which is compared with the experimentally observed[16] value of $\Delta U_x = 1.65$. The observed value was derived from a position of the experimental cross section maximum. However, this observed value of $\Delta U_x = 1.65$ seems to depend upon the use of {2 times the "impact energy" ÷ by the reduced mass}$^{\frac{1}{2}}$ in the L-Z formula (Eq. 2.B.3) instead of relative velocity as given by Eq. 2.B.7; this affects the value of the observed ΔU_x by a factor of $(M_A/M)^{\frac{1}{4}} = (85.9/3.82)^{\frac{1}{4}} = 2.2$, with the observed ΔU_x being smaller if v_{REL} were correctly used. The parameters ($\Delta E = 11.1$ ev, $R_x = 5.0\ a_o$, $\Delta U_x = 1.65$ ev, and

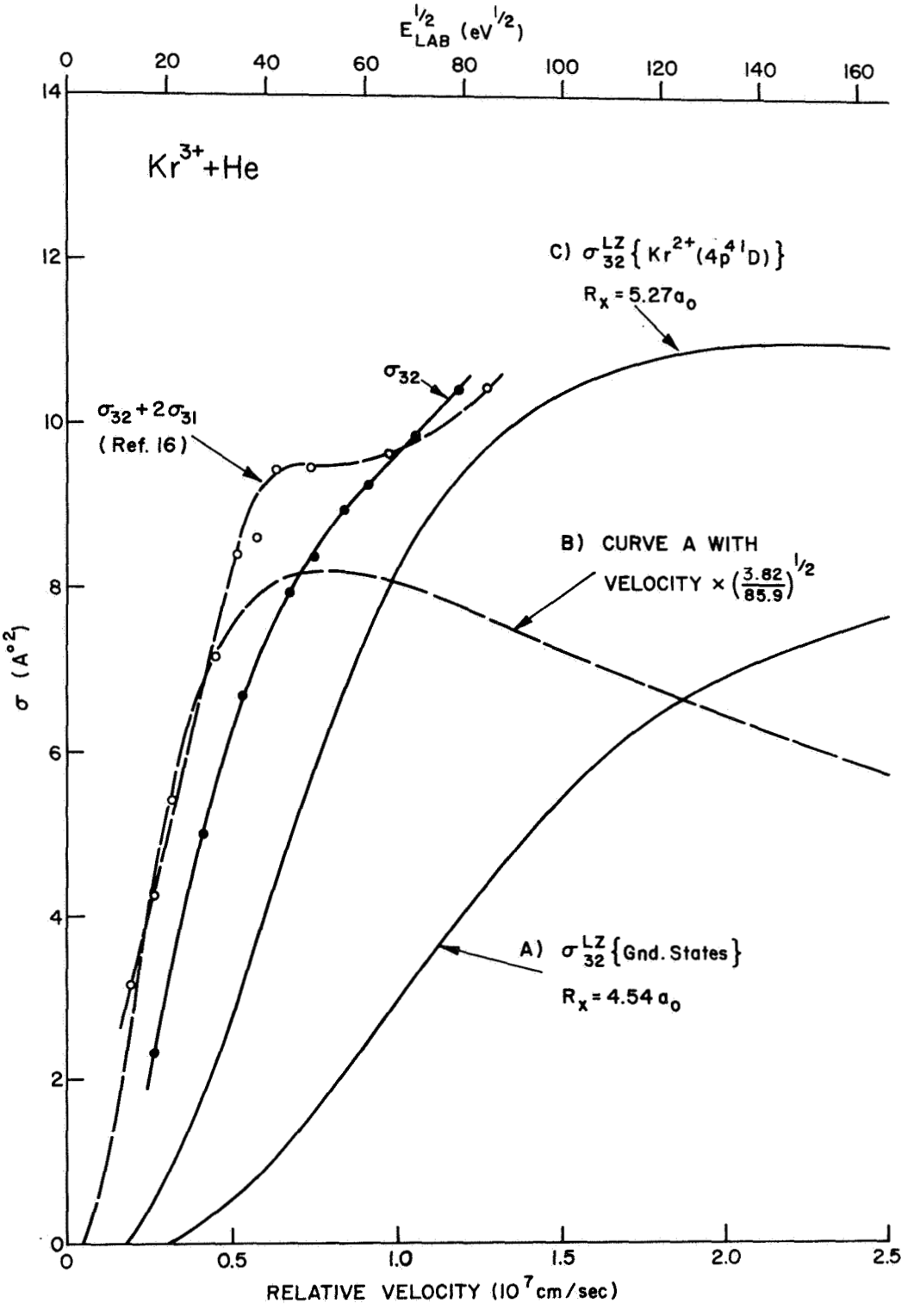

Fig. 6.A.1. Experimental Cross Sections for Kr^{3+} + He and Empirical Functions σ^{LZ}. (Data from Hasted and Chong[16] and this experiment.)

E_P^{Max} = 1900 ev) listed by Hasted and Chong approximately satisfy Eq. 2.B.16 if $M = 3.82$ is used with E_P instead of the correct $M_A = 85.9$.

We now consider the empirical σ^{LZ} function of Eq. 2.B.18. Using the ground state energy defect, $\Delta E = 12.36$ ev, and $Z = 3$, we have $R_x = 4.54\ a_o$ from Eq. 2.B.8. The empirical curve of Fig. 2.B.1 gives $\Delta U(R_x) = 1.93$ ev. The σ^{LZ} function for these values is curve A of Fig. 6.A.1 and is quite different from the experimental curves. Using the incorrect mass in the σ^{LZ} function, or equivalently multiplying the velocity scale by $(M/M_A)^{\frac{1}{2}} = (3.82/85.9)^{\frac{1}{2}} = .21$, gives curve B which is similar to the experimental curves but is not correct.

An agreement could be forced by using the correct velocity and selecting the empirical value of ΔU which would give curve B. The selected value of ΔU would thus be $\Delta U = \Delta U(R_x)/2.2 = .88$ ev which is closer to the calculated $\Delta U = 1.17$, but the selection of an observed ΔU in this manner seems somewhat arbitrary. The difficulty of accurately choosing an observed ΔU according to the position of a cross section maximum (or vice-versa) is demonstrated by the above considerations which suggest that the interpretations and conclusions of Hasted and co-workers concerning the applicability of the L - Z theory be regarded with caution.

Furthermore, capture into the excited states of Kr^{2+} must also be considered. The empirical σ^{LZ} function for capture into the state that is 1.82 ev above ground is $\sigma^{LZ}(\Delta E = 10.55, R_x = 5.27\ a_o, \Delta U(R_x) = 1.25$ ev) and is curve C of Fig. 6.A.1. Note that curve C is

a better fit to the experimental results and only a small change of ΔU would improve the fit, but the experimental results are probably the sum of the capture into several states. Also, the inaccuracy of the simple L - Z theory itself and the improved treatment by BJS should be considered in any detailed comparison with theory.

Data over a wider range of velocities are required to determine the maximum value of this cross section and its velocity position. On the basis of the present knowledge, it is not possible to define which states are involved in the capture process or to make a more meaningful comparison between theory and experiment.

B. Carbon (2+) on Helium, Neon and Argon

The experimental results for the total cross sections for single electron capture of C^{2+} from Helium, Neon and Argon are shown in Fig. 6.B.1. These results have essentially the same velocity dependence as the previous results of Hasted and Smith[31], but the magnitude of the cross section is approximately 50% smaller. The differences in the velocity dependence among the cross sections for the three target gases are apparent. The energy defects for all particles in the ground state are $\Delta E_{He} = -.204$ ev , $\Delta E_{Ne} = 2.82$ ev and $\Delta E_{Ar} = 8.62$ ev. The corresponding zero-order potential energy curves for Helium do not cross, for Neon they cross at $R_x = \underline{9.71}\ a_o$, and for Argon they cross at $R_x = \underline{4.14}\ a_o$.

Since the life-time of some metastable ions is longer than the time-of-flight, TOF , from the source to the collision region (TOF $\sim$ 100 cm/v $\sim 10^{-5}$ to 10^{-6} sec) , it is possible that some of the projectile ions are in excited states, such as the first excited state of C^{2+} ($2p^3P^o_{o,2}$; $E_{ex} = 6.49$ ev). An interpretation of the cross sections for the C^{2+} collisions is first considered on the assumption that the fraction of metastable projectiles is insignificant, and then the possibility of the projectiles being in the first excited state is also considered. The states of the ions and the various parameters to be considered are listed in Table 6.1.

1. Carbon (2+) on Helium

There are no exothermic pairs of states for single electron capture of C^{2+} from Helium, if the projectile ion is in the ground

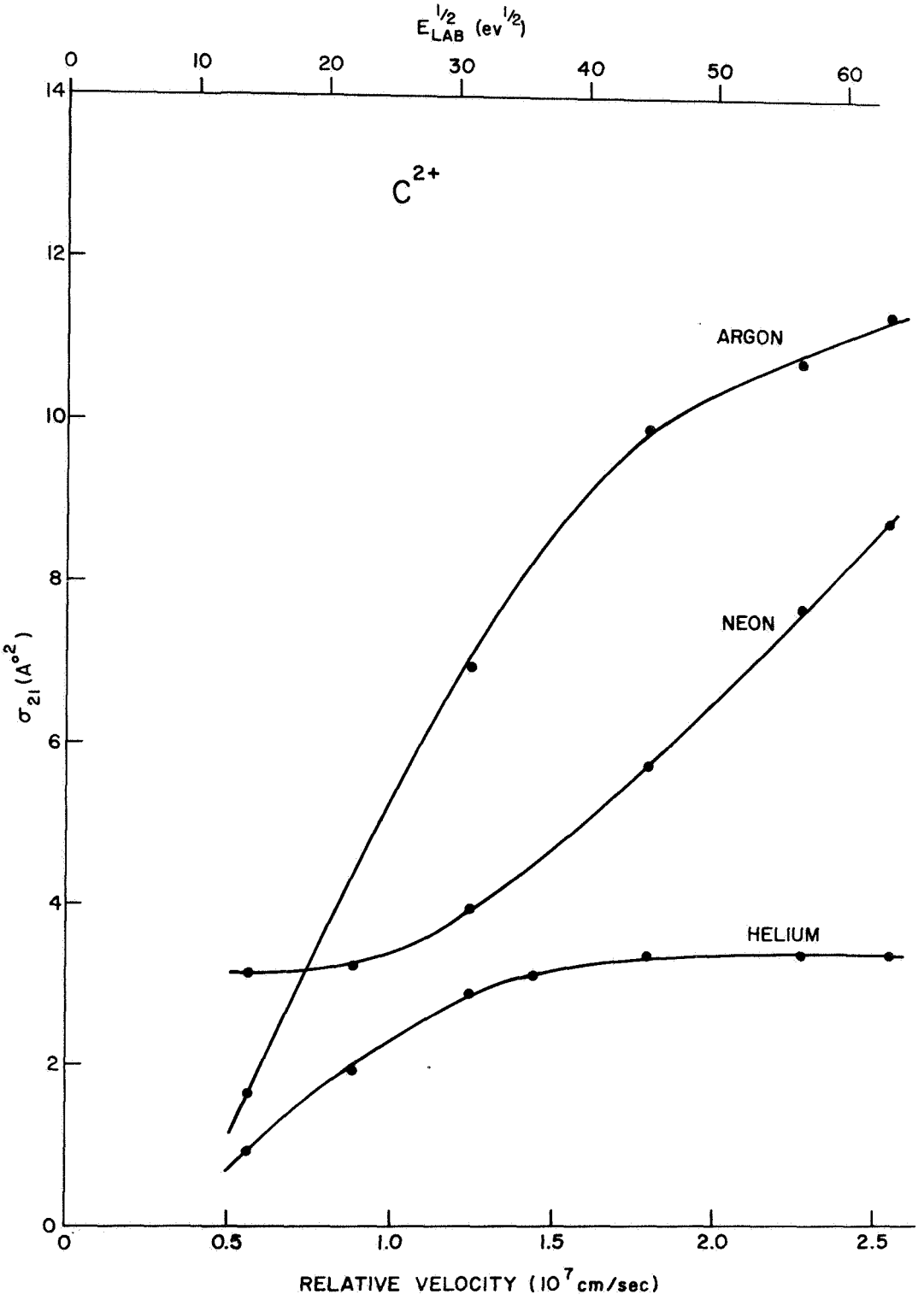

Fig. 6.B.1. Total Single-Electron Capture Cross Sections for C^{2+} on He , Ne and Ar .

TABLE 6.1 States and Parameters for Single-Electron Capture by Carbon (2+)

Target	Initial State	Final State	Final Excit. Energy (ev)	Energy Defect & Crossing Pt. ΔE (ev)	$\Delta E/(z-1)$ (ev)	R_x (a_o)	L - Z Parameters $\Delta U(R_x)$ (ev)	J_{max} (A^{o2})	$v^{\sigma max}_{REL}$ (10^7 cm/sec)	Target Excitation E_{Ex} (ev)	R^{Ex}_x (a_o)	Remarks
Helium	$3s^2\ ^1S$ (ground state of C^{2+})(IP_2 = 24.4 ev)	$2p\ ^2P^o$	0	- .204	- .204	--	--	--	--	≥40.8	--	Endothermic
	$2p\ ^3P^o_{o,2}$	$2p\ ^2P^o$	0	6.28	6.28	4.46	2.01	7.9	7.9		--	
	(E_{ex} = 6.5 ev)	$2p^2\ ^4P$	5.33	.95	.95	28.6	$<10^{-9}$	large	small		--	
Neon	$2s^2\ ^1S$	$2p\ ^2P^o$	0	2.82	2.82	9.71	.072	38	.053	≥26.9	--	
	$2p\ ^2P^o_{o,2}$	$2p\ ^2P^o$	0	9.30	9.30	3.34	3.78	4.4	11.1		--	
		$2p^2\ ^4P$	5.33	3.97	3.97	6.96	.48	19	1.2		--	
		$2p^2\ ^2D$	9.29	.014	.014	>99					--	
Argon	$2s^2\ ^1S$	$2p\ ^2P^o$	0	8.62	8.62	4.14	2.39	6.8	4.8	≥13.5	--	
		$2p^2\ ^2P$	5.33	3.29	3.29	8.56	.17	29	.21		--	
	$2p\ ^3P^o_{o,2}$	$2p\ ^2P^o$	0	15.1		3.11	4.41	3.9	5.3		16.8	
		$2p^2\ ^4P$	5.33	9.78		3.85	2.80	5.9	5.0		--	
		$2p^2\ ^2D$	9.29	5.82		5.35	1.20	11.4	2.9		--	
		$2p^2\ ^2S$	11.96	3.14		8.92	.13	32	.14		--	
		$2p^2\ ^2P$	13.71	1.39		19.6	3.4×10^{-7}	large	small		--	
		$3s\ ^2S$	14.45	.66		41	$<10^{-9}$	large	small		--	

state. The ground state case is endothermic by -.204 ev. Hasted and Smith[31] note the form of the C^{2+} + He cross section is similar to the form of other cross sections (for singly-charged ions) that can be qualitatively described by the adiabatic condition, Eq. 1.A.2, which is

$$v_{REL}^{m} \sim 0.13|\Delta E(ev)|\ell(a_o) \quad (10^7 \text{ cm/sec}) \tag{6.B.1}$$

where ΔE is the energy defect at infinity and ℓ is the approximate range of the interaction. For the singly-charged ion case, ΔE is approximately constant for all R and values of $\ell = 10 - 20\ (a_o)$ fit the experimental data[7,52]. For the multiply-charged ion case, it is not clear what values of the adiabatic parameters, ΔE and ℓ, should be used since ΔE is a strong function of R given by

$$\Delta E(R) = -\Delta E(\infty) + \frac{27.21}{R(a_o)} \quad (ev) \ . \tag{6.B.2}$$

Since the average value of ΔE for C^{2+} + Helium in the range of $R = 5$ to $10\ a_o$ is about -4 ev, we might choose $|\Delta E| = 4$ ev and $\ell = 5\ a_o$; this implies $v_{REL}^{m} \sim 2.6 \times 10^7$ cm/sec, which is consistent with the experimental data of Fig. 6.B.1.

If the projectile ions were in the first excited state, then capture into a 2s orbit of $C^{+}(2s^2 2p^2 P^o)$ is exothermic by 6.28 ev ($R_x = 4.46\ a_o$) and capture into a 2p orbit is exothermic by 0.95 ev ($R_x = 28.6\ a_o$). The first ($R_x = 4.46\ a_o$) of these cases has an empirical σ^{LZ} function (see Fig. 2.B.2) similar to the measured

cross section. Hence, the measured cross section cannot be definitely ascribed to the endothermic pair of states unless most of the projectile ions were definitely in the ground state.

2. Carbon (2+) on Neon

Only one pair of states is exothermic for single-electron capture of C^{2+} from Neon if the projectile C^{2+} ions are in the ground state. The energy defect between these ground states is $\Delta E = 2.82$ ev, and the crossing point is $R_x = 9.71\ a_o$. Capture into an excited state of C^{+} is endothermic by at least 2.5 ev, and excitation of the neon target is endothermic by at least 24 ev.

The empirical σ^{LZ} function, σ^{LZ} ($\Delta E = 2.82$ ev, $R_x = 9.71$, $\Delta U(R_x) = .072$ ev), is plotted in Fig. 6.B.2 along with the experimental data. The function σ^{LZ} has a maximum at a very low velocity, $v_{REL} = .05 \times 10^7$ cm/sec, and has no resemblance to the experimental curve

Considering the possibility that the projectile ion is in its first excited state, leads to two additional σ^{LZ} functions also plotted in Fig. 6.B.2. Considerable manipulation of the L - Z parameters would be required to force a resemblance between the data and any of these σ^{LZ} functions. We conclude that the measured cross section is not due to transitions near a pseudo-crossing of the potential energy curves as described by the L - Z theory.

Additional discussion of this cross section is given in section C.2 of this chapter.

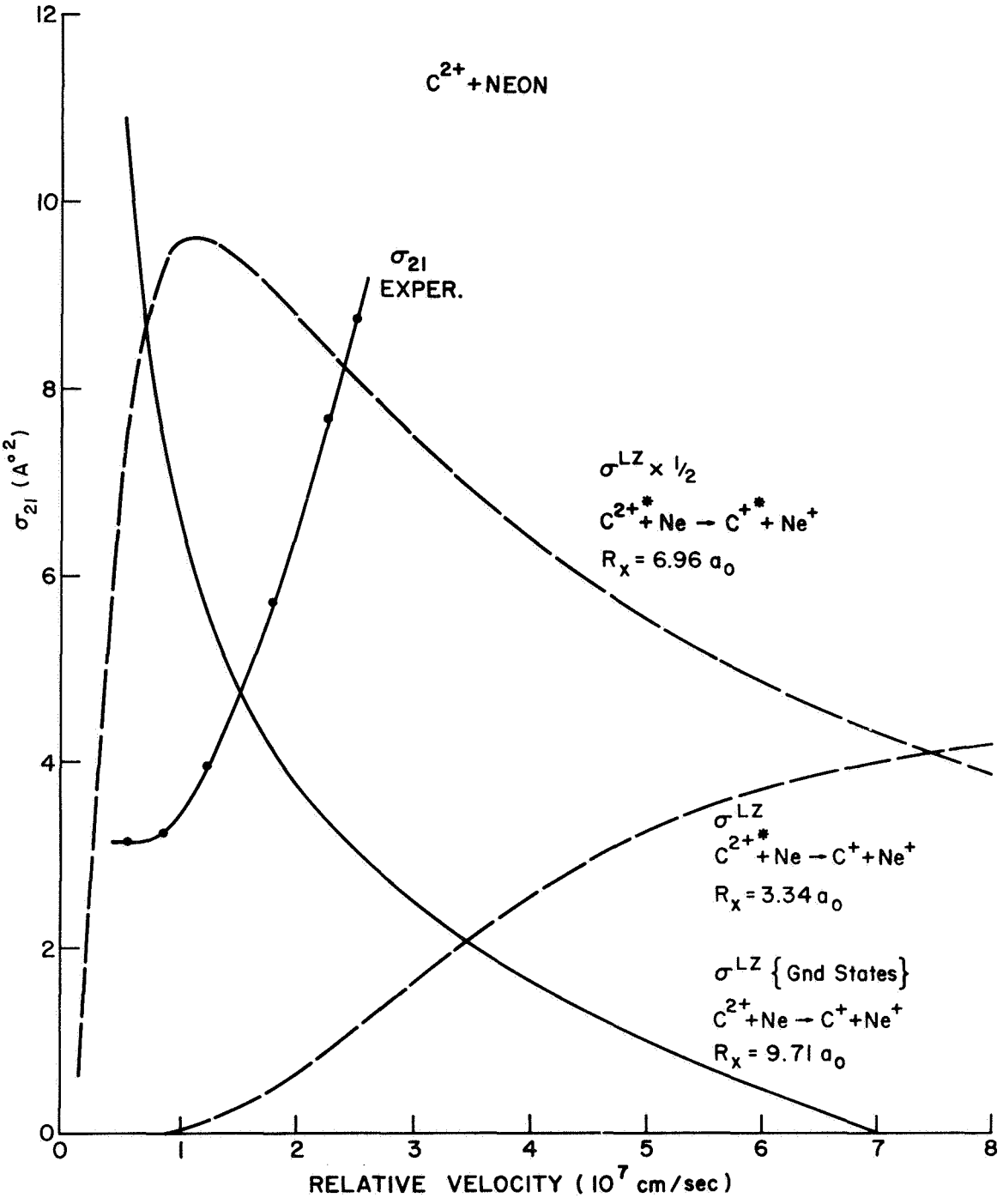

Fig. 6.B.2. Cross Section for C^{2+} + Ne and Empirical Functions σ^{LZ}.

3. Carbon (2+) on Argon

Two pairs of states are exothermic for single-electron capture of C^{2+} from Argon if the projectile C^{2+} ions are in the ground state. The most probable of these two is capture into the ground $(2s^2 2p\ ^2P^o)$ state of C^+ for which the energy defect is $\Delta E = 8.6$ ev and the crossing point is $R_x = \underline{4.14}\ a_o$. The other is capture into the first excited $(2s2p^2\ ^4P)$ state. This excited state probably contributes less to the observed cross section for two reasons: 1) it would be a two-electron process requiring the change of 2s electron of carbon to a 2p state along with capture into the 2p state, 2) since its crossing point is relatively large $(R_x = 8.56\ a_o)$, the empirical σ_{LZ} function has a maximum at very low velocities $(v_R^{max} = .22 \times 10^7$ cm/sec), which is much below the experimental results. Excitation of the target is endothermic by at least 4.9 ev and need not be considered.

The empirical σ^{LZ} function for capture into the ground state is σ^{LZ} $(\Delta E = 8.62$ ev , $R_x = \underline{4.14}\ a_o$, $\Delta U(R_x) = 2.39$ ev) and is plotted in Fig. 2.B.3 along with the experimental results. The experimental curve does not have a maximum in this range of velocities. At this point in a comparison between experiment and the L - Z theory, we should consider the contributions of transitions that occur away from the crossing point. The numerical calculations of BJS for a representative process having a crossing at $5.8\ a_o$ (see Fig. 2.C.2) indicate that the expected cross section might be twice as large as σ^{LZ} and displaced to lower energies. The comparison is subject to the limitation that the theoretical LZ and BJS calculations are restricted to

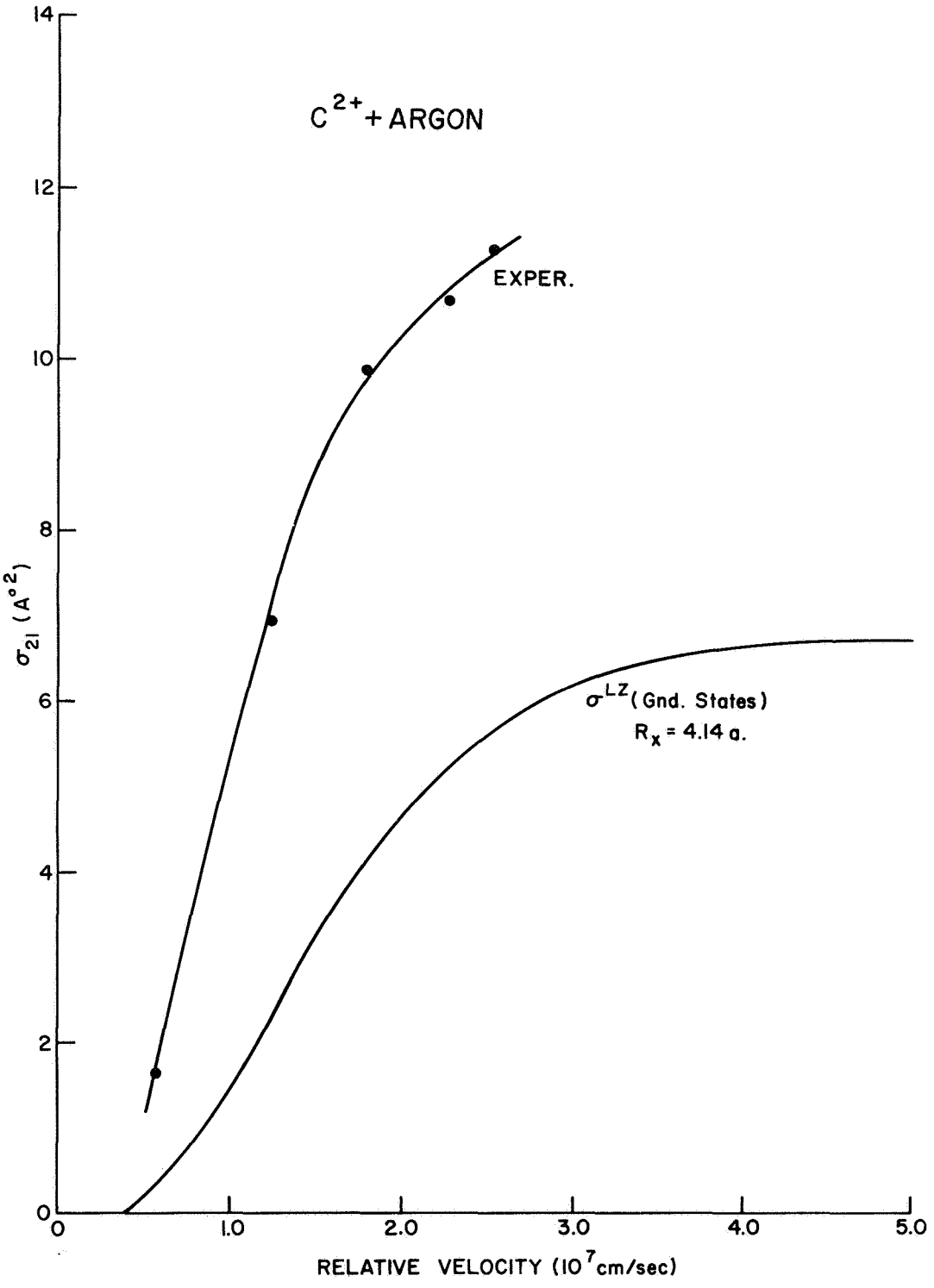

Fig. 6.B.3. Cross Section for C^{2+} + Ar and Empirical Function σ^{LZ}.

spherically symmetric initial and final states, i.e. an $s - s$ transition, whereas the C^{2+} Argon capture process that is being considered is a $p - p$ transition. However, on the basis of this rough comparison the results are not inconsistent with what is theoretically expected for a crossing at this $R_x = \underline{4.14}\ a_o$, but they are not conclusive.

If the fraction of metastable projectiles is significant, then the six excited states for which capture is exothermic must be considered. Although the fraction of metastable projectiles is probably small, the possibility that it is large adds to the uncertainty of the comparison in the previous paragraph.

C. Carbon (4+) on Helium, Neon

The collisions of C^{4+} with Helium and Neon are characterized by a very close crossing of the potential curves for single-electron capture into the ground $(2s\ ^2S_{1/2})$ state and by a very distant crossing for capture into the $3s\ ^2S_{1/2}$ state. On the basis of the L - Z theory the cross section due to a very close crossing is expected to be small and have a maximum at a high (within the near-adiabatic range is implied) velocity; the cross section due to a very distant crossing is expected to be large and have a maximum at a very low velocity on the basis of the L - Z theory with the possibility of a second maximum at a high velocity on the basis of the BJS theory (cf. Chap. 2).

1. Carbon (4+) on Helium

Helium as a target gas has several features that distinguish it from the other rare gases with larger atomic numbers. Both of its electrons are in spherically symmetric orbits (1s), and therefore, if capture is into an s-orbit, the transition is s - s and comparisons with theory are more applicable. The excitation energies of singly ionized Helium are large (> 40.8 ev), so that single-electron capture combined with target excitation is endothermic for $IP_z <$ ~~65.4~~, as it is for capture by C^{4+}; therefore, capture into the ground or excited states of C^{3+} without target excitation are the only exothermic possibilities to be considered.

The presence of excited ions in the projectile beam of C^{4+} ions is unlikely because of their very high excitation energy (> 298 ev). The fourth ionization potential (IP_4) of carbon is 64.5 ev, considerably smaller than IP_5 = 392 ev; the ion-source output of C^{5+} is orders

of magnitude less than the output of C^{4+}. Consequently, since the excitation energy of C^{4+} is almost as large as its ionization energy, it is reasonable to assume that most of the C^{4+} ions are in the ground state.

The states to be considered for single-electron capture of C^{4+} from Helium are listed in Table 6.2 along with their appropriate parameters. Although both the very close crossing, for capture into the 2s (or 2p) orbit, and the distant crossing, for capture into the 3s (or 3p) orbit, are outside the range of applicability of the L - Z theory, the σ^{LZ} cross-section function has been extrapolated and the parameters are listed in the table.

The experimental results for the total cross section for single-electron capture of C^{4+} from Helium are given in Fig. 6.C.1. The error bars shown are the standard deviations of the slope of the linear curve fit to the data for the capture ratio as a function of gas pressure (cf. Chap. 5.A). There is an additional overall limit of error estimated to be $\pm 15\%$. Approximately five data points were taken each day and some of the scatter in the data is due to variations of the detector gain between calibrations. Five of the data points (x) were taken during a period when the detector calibration was not known and these have been normalized to the other points; the same factor of normalization was used for four data points of C^{4+} on Neon (Fig. 6.C.2) that were taken during the same period. The line drawn through the points consists of two linear segments that are least-squares fits to the data, and a smooth curve joining these segments; each point is weighted in the curve-fit in inverse proportion to its deviation.

Table 6.2 States and Parameters for Single Electron Capture by Carbon (4+)

Target	Projectile			Energy Defect & Crossing Pt.			L - Z Parameters			Target Excitation		Target Ionization		Remarks
	Initial State	Final State	Final Excit. Energy (ev)	ΔE (ev)	$\Delta E/(Z-1)$ (ev)	R_x (a_o)	$\Delta U(R_x)$ (ev)	σ^{LZ}_{max} (A^{o2})	$v^{\sigma max}_{REL}$ (10^7 cm/sec)	E_{Ex} (ev)	R^{Ex}_x (a_o)	ΔE_o (ev)	R_{xo} (a_o)	
Helium	$1s^2\ ^1S_o$ of C^{4+} (IP_4 = 64.5 ev)	$2s\ ^2S_{\frac{1}{2}}$	0	39.9	13.3	2.51	6.71	2.5	5.4	≥40.8	--	<0	--	S - S trans.
		$2p\ ^2P_{\frac{1}{2},\frac{3}{2}}$	8.0	31.9	10.6	2.93	5.03	3.4	5.0		--	"	--	
		$3s\ ^2S_{\frac{1}{2}}$	37.5	2.36	.786	34.6	$<10^{-9}$	large	small		--	"	--	S - S trans.
		$3p\ ^2P_{\frac{1}{2},\frac{3}{2}}$	37.7	2.23	.742	36.7	"	"	"		--	"	--	
		$3d\ ^2D_{\frac{3}{2},\frac{5}{2}}$	40.3	- .373	- .124	--	--	--	--		--	"	--	endothermic
Neon	$1s^2\ ^1S_o$ of C^{4+}	$2s\ ^2S_{\frac{1}{2}}$	0	42.9	14.3	2.63	6.17	2.8	3.8	≥26.9	>5.3	1.85	88.	
		$2p\ ^2P_{\frac{1}{2},\frac{3}{2}}$	8.0	34.9	11.6	2.97	4.89	3.5	3.7		≥10.2	<0	--	
		$3s\ ^2S_{\frac{1}{2}}$	37.5	5.38	1.79	15.2	.0003	large	small		--	"	--	
		$3p\ ^2P_{\frac{1}{2},\frac{3}{2}}$	37.7	5.25	1.74	15.6	.0002	"	"		--	"	--	
		$3d\ ^2D_{\frac{3}{2},\frac{5}{2}}$	40.3	2.65	.88	30.8	10^{-9}	"	"		--	"	--	
Argon	$1s^2\ ^1S_o$ of C^{4+}	$2s\ ^2S_{\frac{1}{2}}$	0	48.7	16.2	3.19	4.19	4.1	1.4	≥13.5	≥3.7	21.1	8.0	
		$2p\ ^2P_{\frac{1}{2},\frac{3}{2}}$	8.0	40.7	13.6	3.44	3.55	4.8	1.4		≥4.2	13.1	12.5	
		$3s\ ^2S_{\frac{1}{2}}$	37.5	11.2	3.73	7.76	.29	25	.15		--	<0	--	
		$3p\ ^2P_{\frac{1}{2},\frac{3}{2}}$	37.7	11.1	3.68	7.84	.28	26	.15		--	"	--	
		$3d\ ^2D_{\frac{3}{2},\frac{5}{2}}$	40.3	8.45	2.82	9.95	.061	179	.01		--	"	--	
		$4s\ ^2S$	49.8	- 1.03	- .34	--	--	--	--		--	"	--	

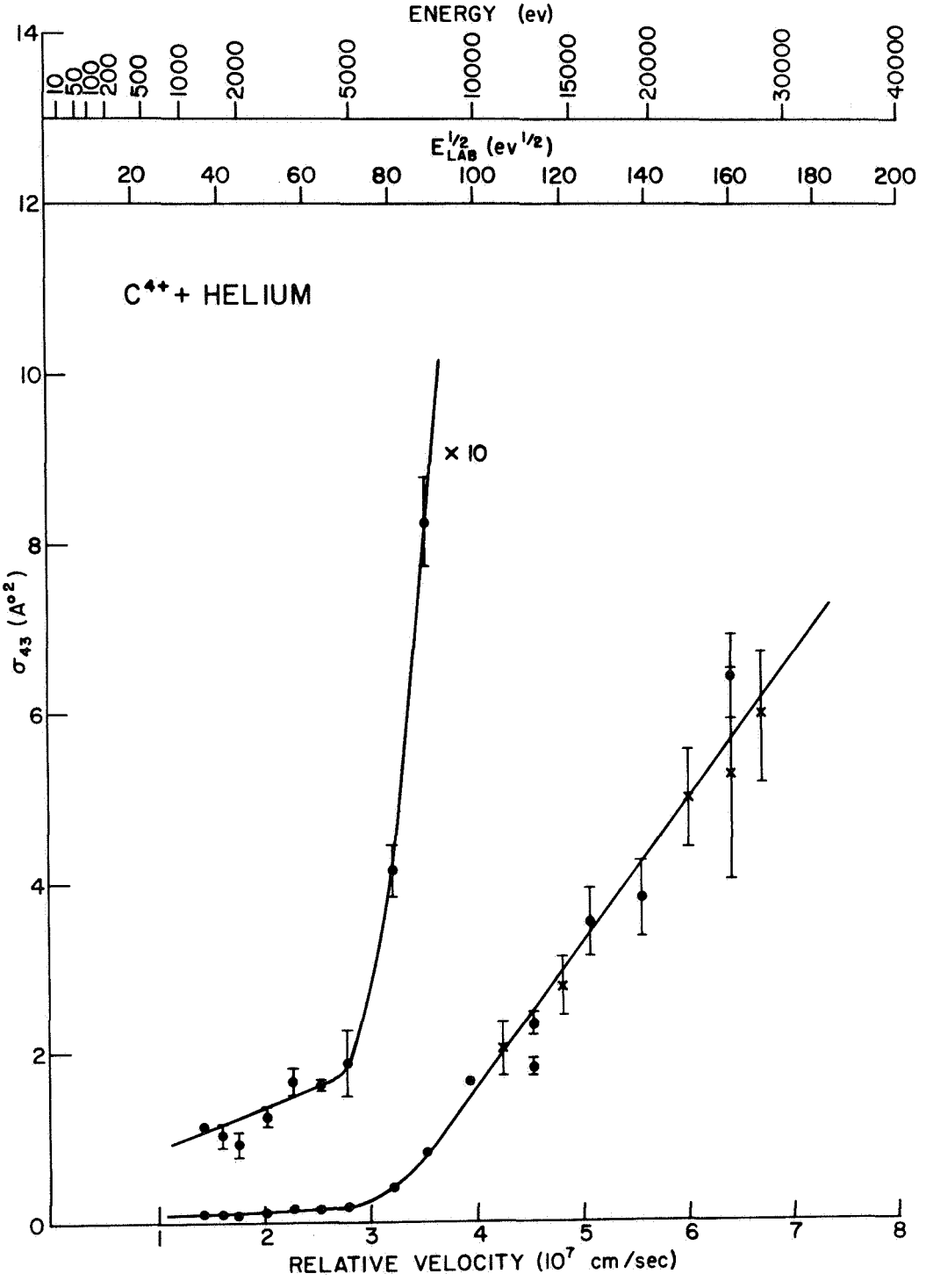

Fig. 6.C.1. Total Single-Electron Capture Cross Section Results for C^{4+} + Helium. (Error bars are standard deviations of the mean.)

The value of the cross section is small below $v_R \gtrsim 3 \times 10^7$ cm/sec ($E_{Lab} \gtrsim 6000$ ev) with a linear increase at higher velocities. There is no evidence of a contribution to the cross section similar to the broad maximum of the $\sigma^{LZ}(\Delta E = 39.9 \text{ ev}, \; R_x = 2.51 \; a_o \; , \; \Delta U(R_x) = 6.7 \text{ ev})$ function which extends through most of this velocity range (cf. Fig. 2.B.2). As previously noted, the L - Z calculations have a very limited validity for this small a crossing distance[24]. A discussion of the increase of the cross section at higher velocities and of the distant crossing at $R_x = 34.6 \; a_o$ is deferred to the next section.

2. Carbon (4+) on Neon

The interactions of C^{4+} with Neon and with Helium are similar in that their respective crossing points for single-electron capture are in the same ranges. The ionization potential of Neon is smaller than that of Helium so that the energy defects are larger and, consequently, the respective crossing points are at somewhat smaller internuclear separations. Since the outer electrons of Neon are in p-orbits, the transitions to be considered are not s - s transitions; comparisons with theoretical calculations that use spherically symmetric initial and final states are therefore less valid.

The states to be considered for single-electron capture of C^{4+} from Neon are also listed in Table 6.2. In addition, the excitation energies of Ne^+ are sufficiently small ($E_{Ex} \gtrsim 26.9$ ev) so that single-electron capture into the 2s (or 2p) state of C^{3+} with target excitation is exothermic; the corresponding crossing points are in (and above) the intermediate range ($R_x^{Ex} \gtrsim 5.3 \; a_o$) . In fact,electron-

capture with ionization (excitation of an additional electron to the continuum) is also exothermic, but the crossing point (cf. Chap. 2.D) is at a very large ($R_{x_o} = 88\ a_o$) separation. The approximate potential curves for capture into the 2s state of C^{3+} are given in Fig. 2.D.3.

The experimental results for the total cross section for single-electron capture of C^{4+} from Neon are shown in Fig. 6.C.2. As discussed in Chap. 1.A, this measured cross section is the sum of the cross section for single-electron capture with no other electrons changing state and of the cross sections for single-electron capture with target excitation or with target ionization. The error bars, limit of error and normalization of four data points are as described in the previous section. The smooth curve is a weighted fit of degree 3 in the velocity.

The main characteristic of this measured cross section is the increase at higher velocities similar to the results for C^{4+} on Helium. Returning to the theoretical considerations of Chap. 2, we note the results of the numerical calculations of Bates, Johnson and Stewart[13] for a representative process ($M_g^{2+} + H \rightarrow M_g^{+} + H^{+}$, $R_x = 18.9\ a_o$); their calculations show, for a crossing at the curves at large separations, a rise to a second maximum at high velocity. BJS point out that this second maximum of the calculated cross section is the result of transitions that occur in the range of internuclear separation of order one-half the curve-crossing distance. For small crossing points this contribution to the cross section from transitions occurring away from the crossing point is merged with the ordinary L - Z type

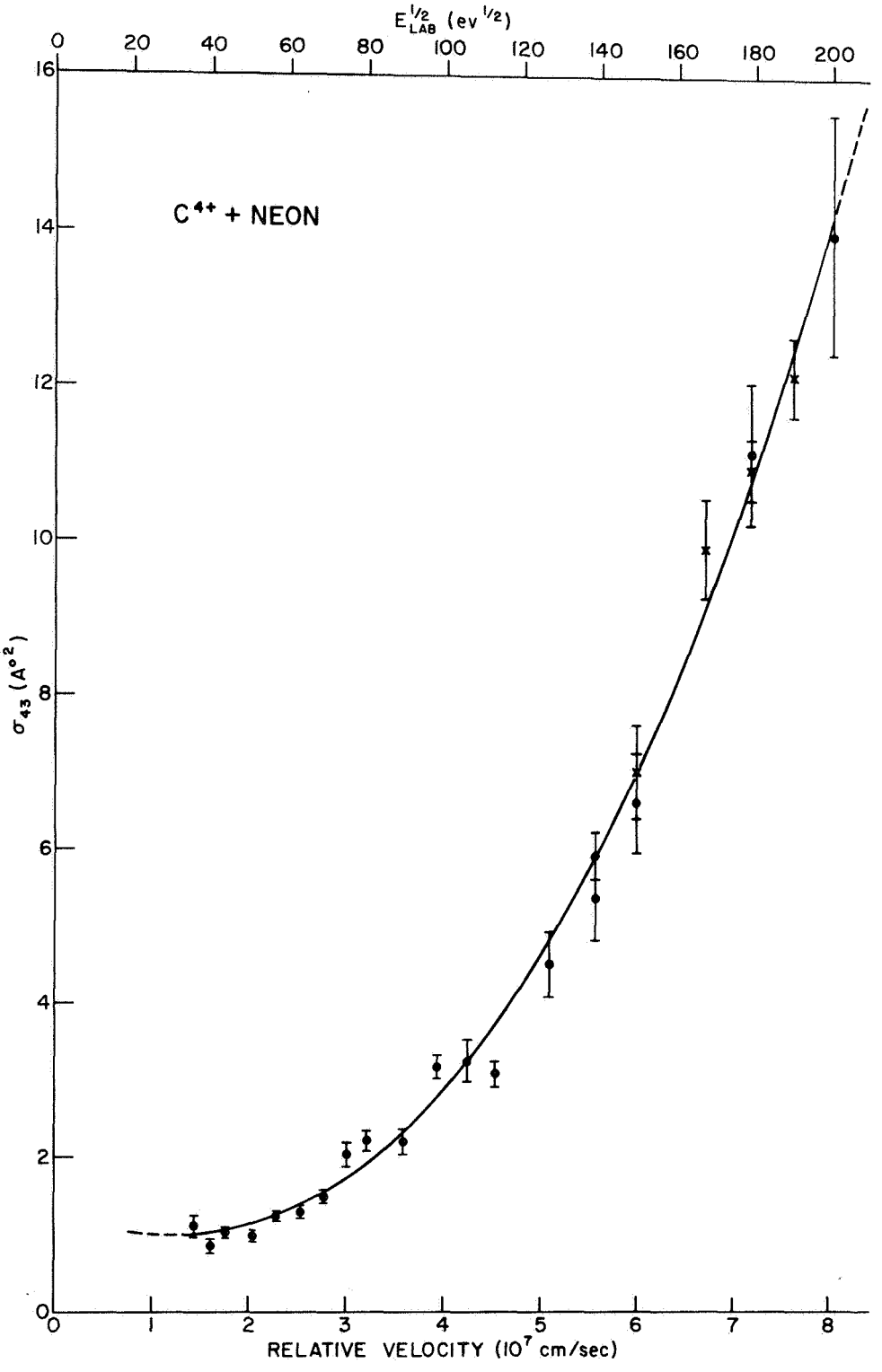

Fig. 6.C.2. Total Single-Electron Capture Cross Section Results for C^{4+} + Neon. (Error bars are standard deviations of the mean.)

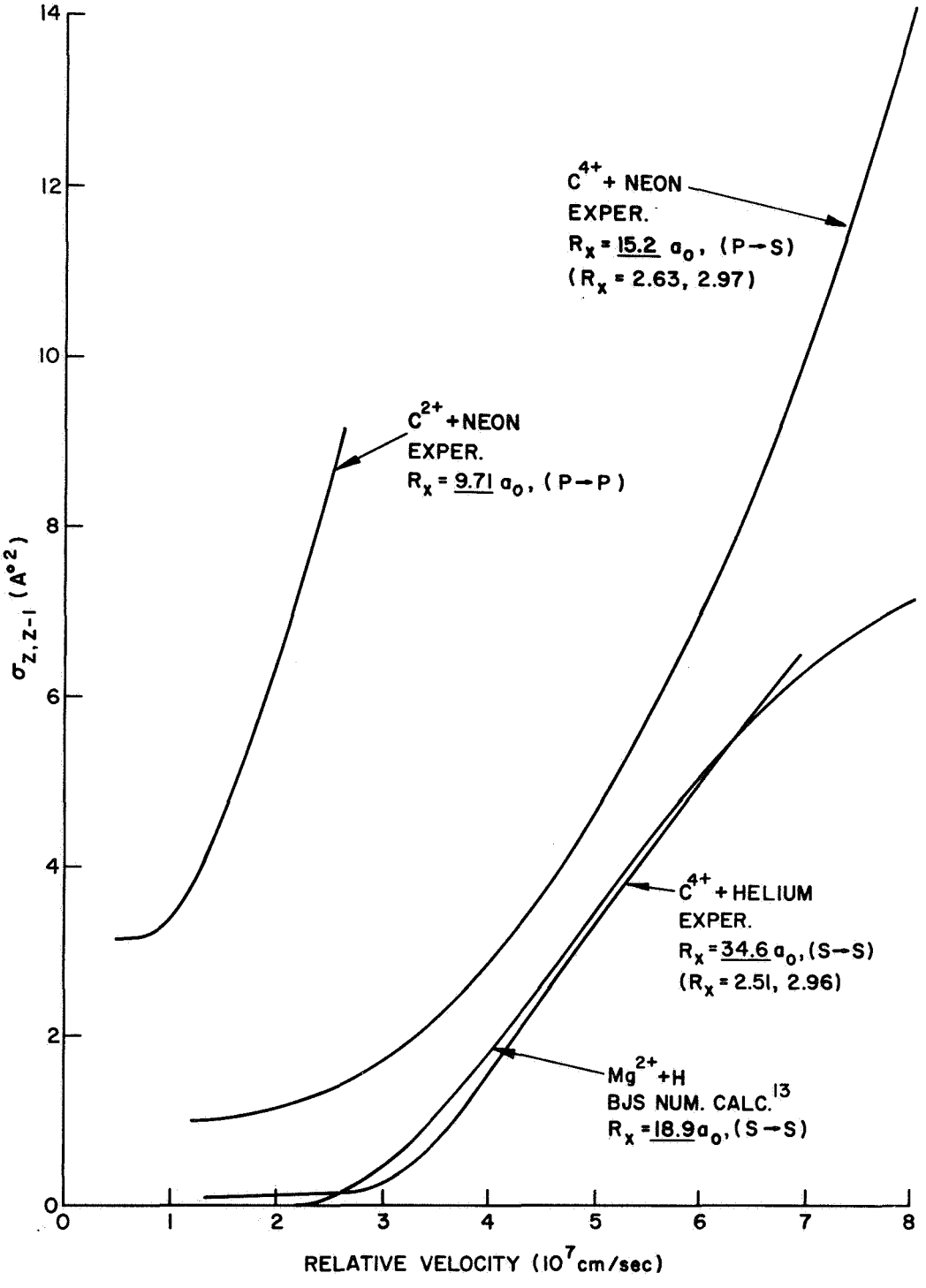

Fig. 6.C.3. Experimental and Theoretical Cross Sections for Processes with Distant Crossings. (Cross sections rise toward a "second maximum.")

contribution from transitions near the crossing point. The theoretical trend of the position of the second maximum is toward higher velocities for larger crossing points.

The calculated results of BJS for $(Mg^{2+} + H)$ are shown in Fig. 6.C.3 along with the experimental results for $(C^{4+} + He)$, $(C^{4+} + Ne)$, and $C^{2+} + Ne)$. The cross sections are plotted as a function of the relative velocity. Considering the limits of error of the $(C^{4+} + He)$ results and the limited extent of the similarity of the $(C^{4+} + He)$ and the $(Mg^{2+} + H)$ processes, the closeness of these two cross-section curves is somewhat accidental. The transition due to the distant crossing of the $(C^{4+} + He)$ process is an s - s transition, and this combination, $(C^{4+} + He)$, seems to be particularly suitable to a numerical calculation. The trend of the increase in the cross section is toward higher velocities for larger crossing distances.

The results shown in Fig. 6.C.3 suggest that the measured cross sections for $(C^{4+} + He)$, $(C^{4+} + Ne)$ and $(C^{2+} + Ne)$ are a result of the second maximum due to relatively distant crossing points. The results of a numerical calculation for $(C^{4+} + He)$ would provide a direct comparison between theory and experiment.

D. Carbon (4+) on Argon

Single-electron capture without target excitation of C^{4+} from Argon is exothermic for the same set of final states (cf. Table 6.2) of C^{3+} as it is for a Helium, of a Neon, target atom. Since the first I P of Argon is smaller than that of Neon or Helium (cf. Appendix B), the energy defects for the respective states are larger and the tendency is toward smaller crossing distances. Therefore,

there is also a very close crossing for Argon (slightly more distant because of the larger polarization term) for capture into the 2s (or 2p) state of C^{3+} ; the crossing point for capture from Argon into the 3s (or 3p) state is not very distant, as it was for Helium and Neon, but it is at a moderate internuclear separation ($R_x = 7.8\ a_o$).

Single-electron capture into the 2s or 2p state of C^{3+} with target excitation is more exothermic for Argon than for Neon; the corresponding crossing points (for Argon, $R_x^{Ex} = 3.7\ a_o$) extend through most of the range of internuclear separations. Capture into the 2s state of C^{3+} with target ionization is exothermic by 21.1 ev and the crossing point, R_{xo} , defined in Chap. 2 (cf. Fig 2.D.4) is at a moderate separation ($R_{xo} = 7.96\ a_o$) . The exothermic states and their parameters are listed in Table 6.2.

The experimental results for the total cross section for single-electron capture of C^{4+} from Argon are shown in Fig. 6.D.1. In comparison to the results for either a Helium or a Neon target, this cross section is considerably larger (at low velocities, 50 times the Neon results) and varies relatively less as a function of the relative velocity. Some of the scatter of the data points is again a result of changes in the gains of the detectors, and the variations of the gains were troublesome during this period of data recording. Approximately five data points were taken each day. The limits of error and the error bars are as described in Section C. The smooth curve is a weighted fit of degree 2 in the velocity.

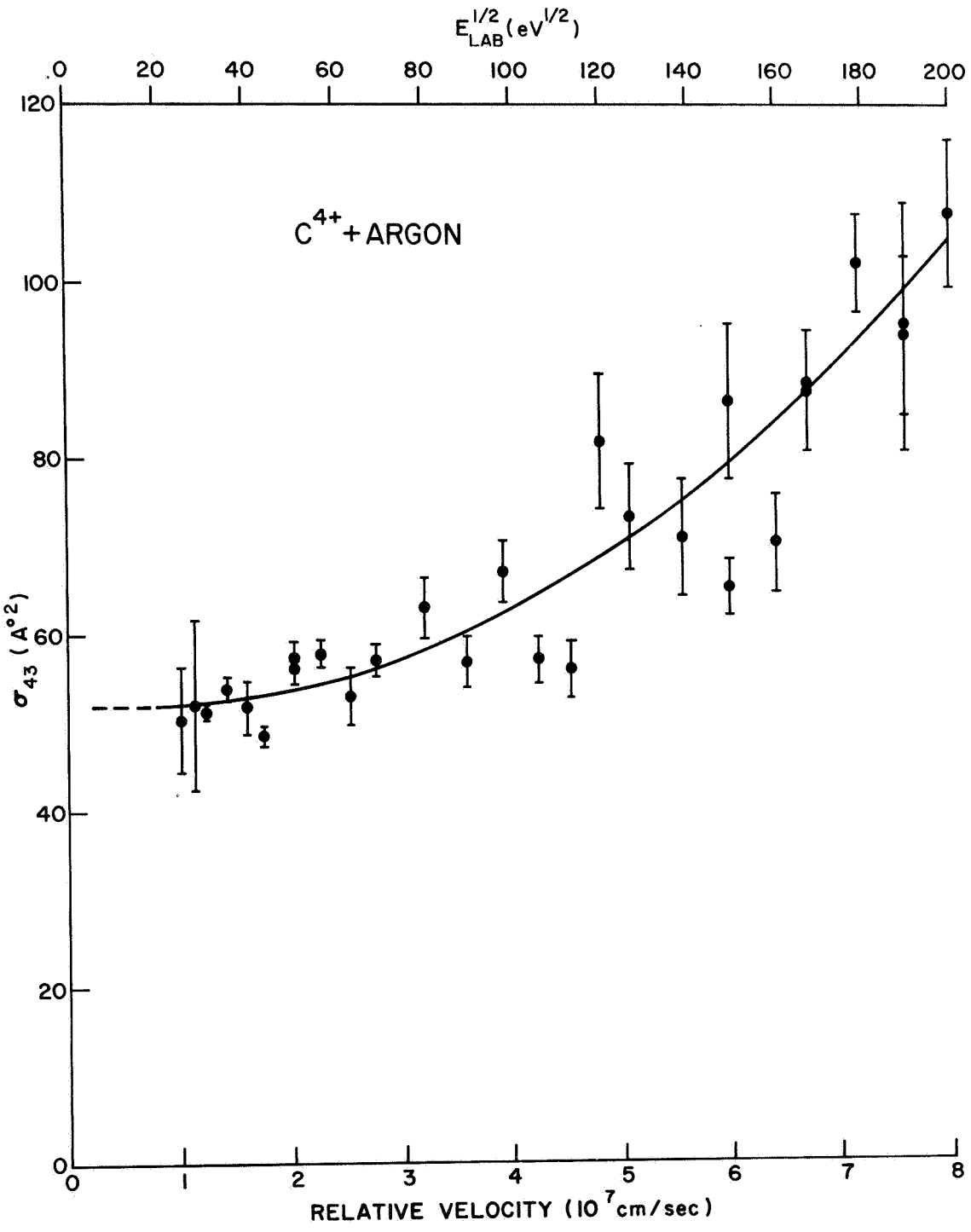

Fig. 6.D.1. Total Single-Electron Capture Cross Section Results for C^{4+} + Argon. (Error bars are standard deviations of the mean.)

The observed cross section may have significant contributions from any or all of the three processes:

(1) electron capture into the 3s (3p) and/or the 2s (2p) state of C^{3+};

(2) electron capture into the 2s (2p) state of C^{3+} with target excitation;

(3) electron capture into the 2s (2p) state of C^{3+} with ionization of the target.

Electron capture into the 3s state with a crossing at $R_x = 7.8\ a_o$, probably contributes at very low velocities due to transitions near the crossing and at somewhat higher velocities due to transitions well away from the crossing. Electron capture with target excitation has many final states with crossings at moderate separations; this contribution is very difficult to assess and might contribute to both the cross section for Argon and that for Neon. As discussed in Chap. 2.D, electron capture with target ionization might be very probable if the crossing point, R_{xo}, is at a moderate separation, as it is for $(C^{4+} + Ar)$. The contribution of capture with ionization should be negligible for $(C^{4+} + Ne)$ and is the probable cause of the large difference between the $(C^{4+} + Ar)$ and the $(C^{4+} + Ne)$ results. Additional experimental analysis would be required to separate these three possible contributions to the $(C^{4+} + Ar)$ cross section.

Some previous experimental results on total ionization cross sections have provided information on the probability of ionization with capture. The results of Flaks, Ogurtsov, and Fedorenko[53] for the total cross section for production of free electrons in the target gas show larger cross sections for $Ne^{Z+} + Xe$ with $Z = 4$ than with smaller Z ; the relative velocities of collision are above $5.5 \quad 10^7$ cm/sec. They attribute this larger cross section to the process of ionization with capture which is exothermic by 63 ev for $N^{4+} + Xe$, and infer from their data that it depends little on the relative velocity. Thus, their results on ionization for $Ne^{4+} + Xe$ and the results of this experiment on capture for $C^{4+} + Ar$ indicate that "capture ionization" is a probable process at low velocities if the process has a large exothermicity.

E. Suggestions for Future Work

The discussion of the results in previous sections indicate that only if the number of pairs of states with probable contributions to the measured cross sections is one or two can conclusions be made about the nature of the cross section for a particular state. Further experimental efforts can proceed in several directions: one direction is to choose simple ion-atom combinations for which only one or two pairs of states need be considered; another direction is to use additional experimental analysis or methods to determine directly the initial and final states of the atoms and ions; also, measurements

of the scattering angle of the fast collision products can be related to the impact parameter, ρ, to give the probability of electron capture as a function of ρ and provide information about the crossing point of the initial and final states as described in reference 54.

The approach of this experiment has been to use relatively simple ion-atom combinations of which the best example is C^{4+} + Helium. The pulsed-discharge ion source may be adaptable to the production of other multiply-charged light ions. Other combinations suitable for experimental study and theoretical calculation can then be selected for experimental measurements.

Additional investigation of the two-electron process of electron-capture with target ionization would be of interest, particularly at low velocities. Not only is it possible that this mechanism greatly enhances the probability of electron capture, but it would also produce free electrons from low velocity collisions between multiply-charged ions and neutral atoms. Measurements of the number and velocity distribution of the free electrons from the target would provide information about the probability and the nature of the capture with ionization process. However, these measurements require a more elaborate experiment and almost certainly a continuous or ac modulated beam of ions. Initially, measurements of just the total electron-capture cross section for combinations of ions and atoms, having a range of exothermicity and a corresponding range of crossing points, would provide more information on the probability of the capture with ionization process.

APPENDIX A

SECONDARY EMISSION ION DETECTORS

The detectors are of the Daly secondary emission type[55] in which ions are accelerated into an aluminum know maintained at a potential of -30 kilovolts relative to the external surfaces of the detector. The resulting secondary electrons, emitted from the aluminum, are then accelerated and focused by the same field into a Pilot B plastic scintillator on the face of a RCA 8575 Photomultiplier tube. The detectors have been designed to operate in either a counting mode (the arrival of the individual ions being sufficiently separated in time) or a pulsed mode (closely spaced arrival of ions during a short interval of time).

1. High Voltage Knob Housing

A cross-sectional view of the detector is shown in Fig. A.1. The relative locations of the ion entrance, HV knob, and scintillator are slightly different than that described in reference 56, for which a plot of the ion and electron trajectories was made. The detector counting rate is constant (see Fig. 4.C.2) as an ion beam is swept across the $\frac{1}{2}$ inch-wide entrance, demonstrating the effectiveness of the ion and electron focusing. Fig. A.1 also shows how two of these detectors have been placed to accept ions that have been separated by $2\ \frac{3}{8}$ inches in the 45° separator.

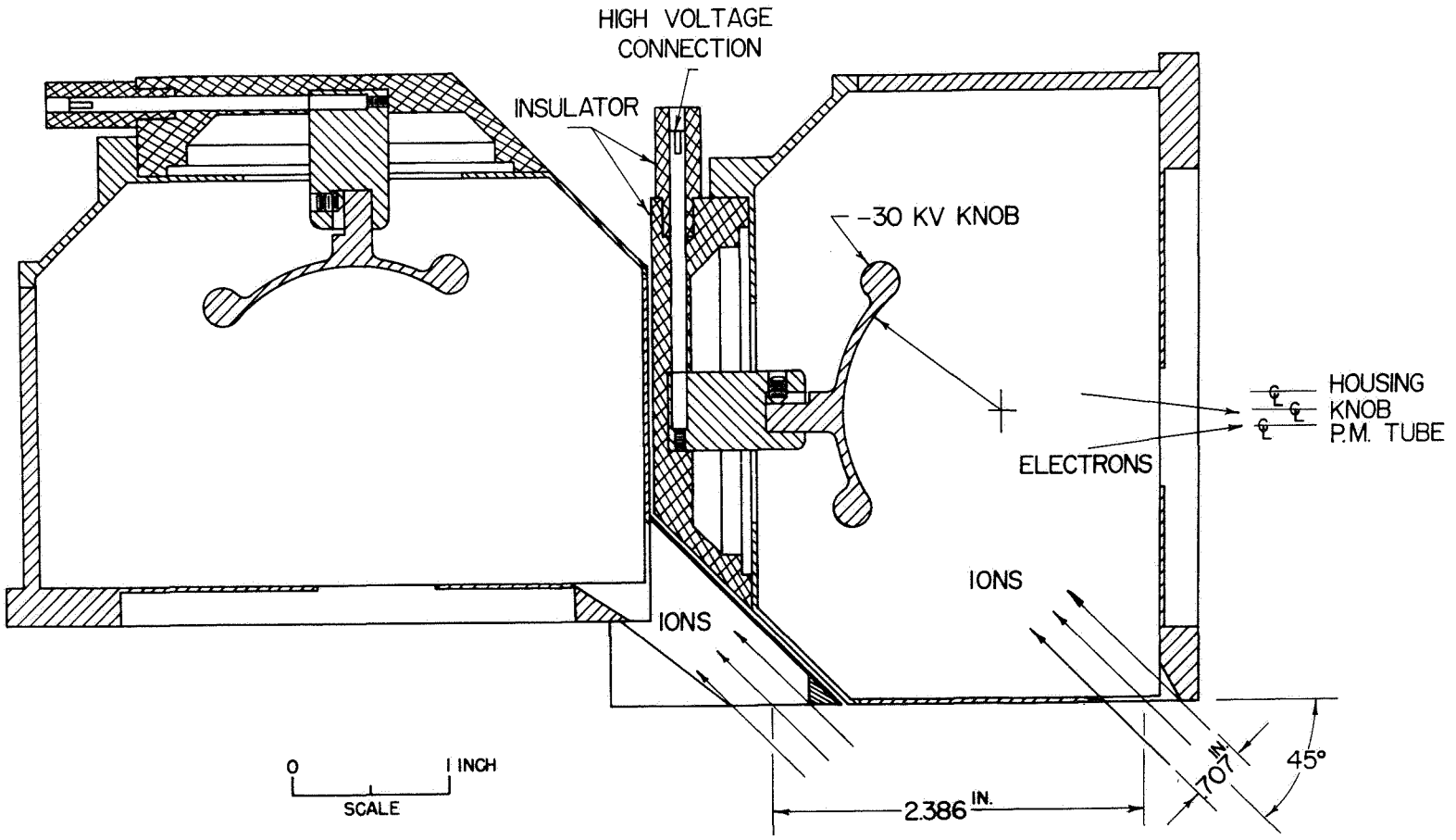

Fig. A.1. Cross-Sectional View of HV Knob Housing of Secondary Emission Ion Detectors.

2. Photomultiplier-Scintillator Assembly

The photomultiplier with its scintillator is mounted on the housing at an angle of 31.5° to allow clearance for the ion beam and the gas cell at the entrance of the 45° separator (cf. Chapter IV) Fig. A.2 is a scale drawing of the photomultiplier housing. The inside of this housing remains at atmospheric pressure. The voltage divider circuitry is contained in the housing. Cables for the voltage supply and for the output signals go through a tube and vacuum bellows to the outside of the vacuum chamber. Hence, only the exterior surfaces of the stainless steel housing and the aluminum-coated scintillator are exposed to the high vacuum.

The aluminum coating on the scintillator is required for grounding and also serves as a reflector to reduce the loss of photons emitted in directions away from the photocathode. The electrons lose energy in the coating,and consequently the number of photons produced by each electron is reduced as the thickness of the coating is increased. However, the efficiency of reflection increases with the thickness of the coating. In order to maximize the illumination of the photocathode, a 1200 A° thick coating is used[57]. The electrons lose an average of 2.5 Kev in the coating[57]. The Pilot-B scintillator is $\frac{1}{16}$ inch thick[58,59] and is mounted on the face with silicon grease[60].

The RCA 8575 tube was chosen for its high quantum efficiency, spectral response suitable for plastic scintillators, and 50 ohm output impedance.[61] The voltage divider circuit is shown in

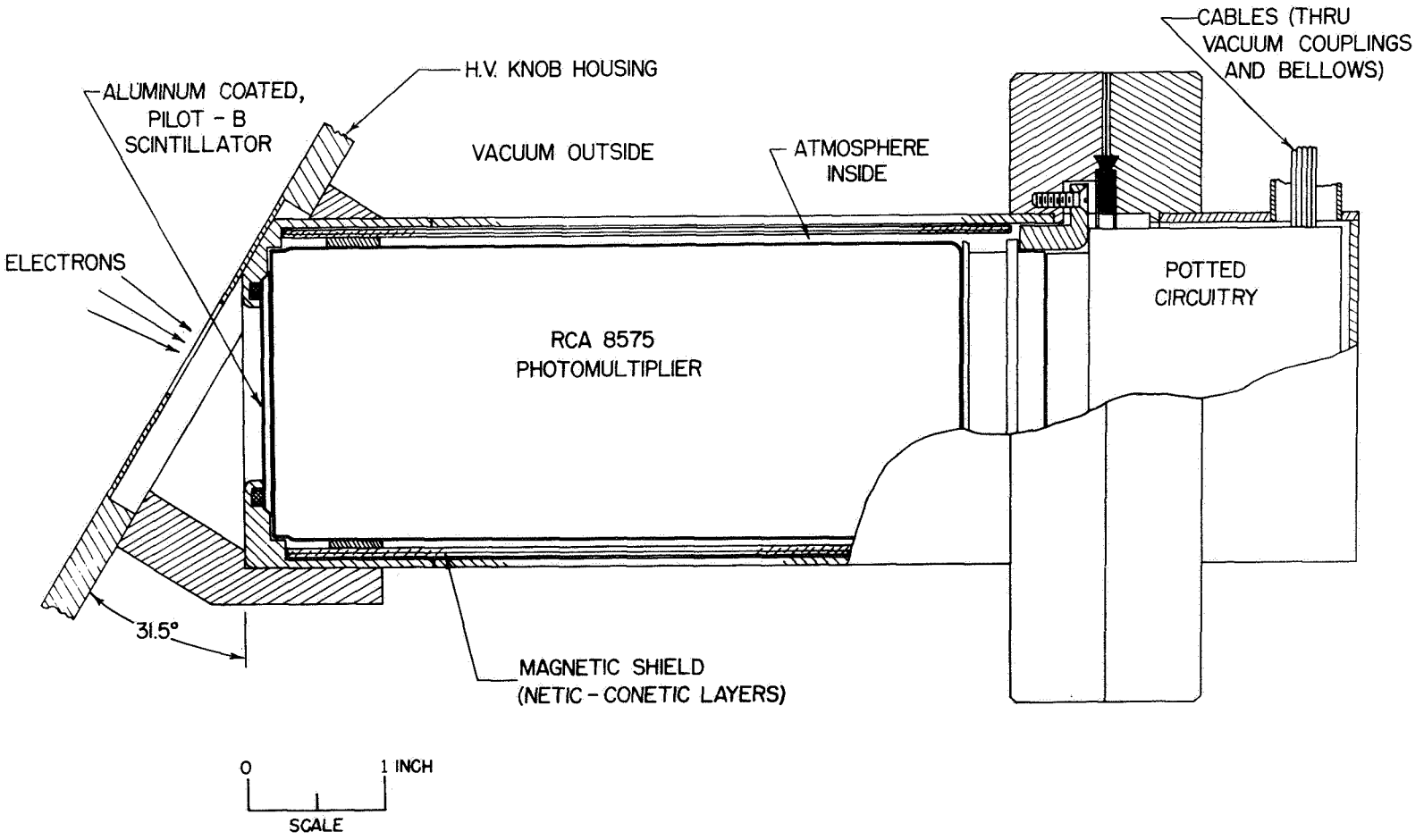

Fig. A.2. Cross-Section View of Photomultiplier-Scintillator Assembly.

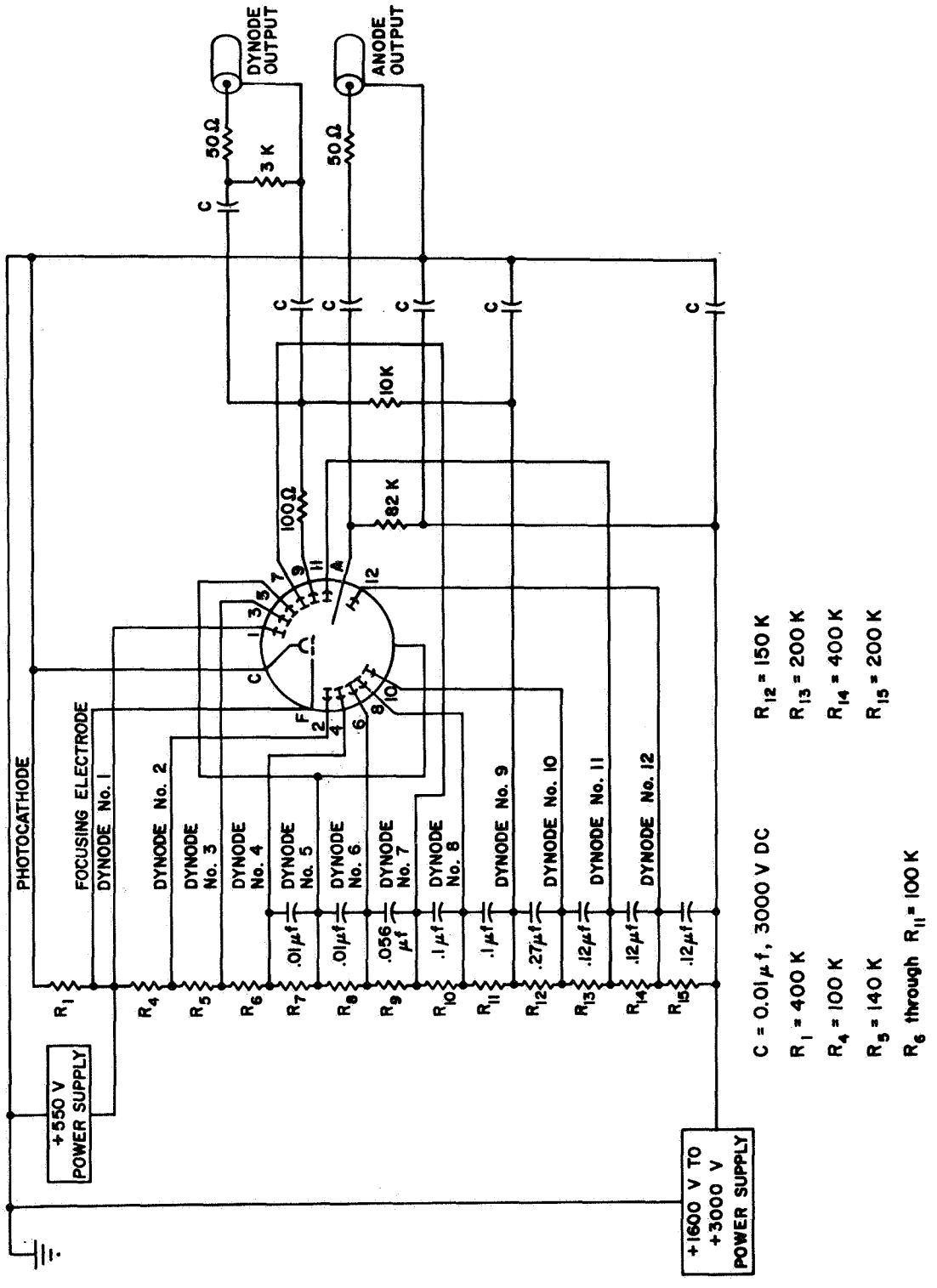

Fig. A.3. Photomultiplier Voltage Supply and Signal Circuitry.

Fig. A.3. The voltage arrangement is per RCA's distribution II, except that the first dynode voltage is maintained at 550 volts when the anode voltage is changed from the maximum of 3 kilovolts. This higher dynode voltage maintains a high first stage gain and reduces the sensitivity to defocusing by external magnetic fields. The magnetic shield (Perfection Mica Co.) around the tube reduces the stray magnetic fields to a permissable level.

3. Output Pulses

Impedance matching of the anode output is simplified by the 50 ohm output impedance of the photomultiplier, and fast pulses are easily obtained. The anode pulse caused by light incident on the tube is displayed (Fig. A.4) on an oscilloscope that has a 3.5 nanosecond rise time. The Pilot B scintillator has a light decay time of 1.7 nanoseconds, and the total width of an anode pulse alone, caused by an ion entering the detector, is about 6 nanoseconds at $\frac{1}{2}$ maximum. Therefore, randomly spaced pulses can be counted to rates above 10 megacycles with high efficiency.

The dynode pulse circuit is designed to produce a much slower pulse, in which the effects of the individual ions are masked. The circuit integrates the net charge removed from the ninth dynode during an interval short compared to its RC decay time of 75 microseconds. Fig. A.5 illustrates the dynode signal caused by two ions several microseconds apart. The height of a dynode signal due to many closely spaced ions is proportional to the number of ions.

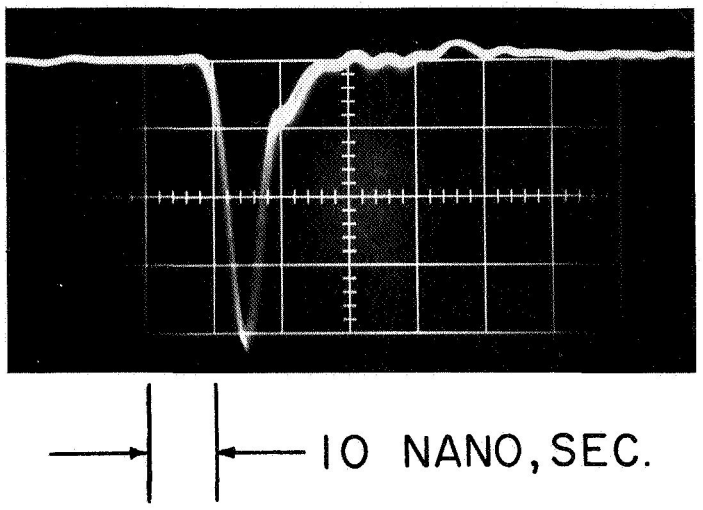

Fig. A.4. Anode Pulse Caused by Incident Light.

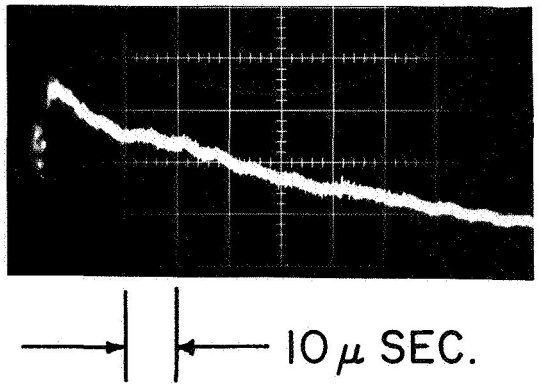

Fig. A.5. Dynode Signal caused by two Ions Separated by Several microseconds.

4. Pulse Height Distributions

The voltage height of an anode pulse (due to an individual ion) across 50 ohms can be estimated with the equation,

$$V \sim 8 \times 10^{-9} \frac{N}{T} \quad \text{(volts)} \tag{A.1}$$

where, T = pulse width ($\sim$ 5 nanoseconds)

$$N = \delta \times \frac{E}{p} \times \varepsilon_1 \times \varepsilon_2 \times G = \# \text{ of electrons deposited on the anode} \tag{A.2}$$

δ = secondary electrons from aluminum per incident ion ($\sim$ 5)

E = energy of electrons at scintillator ($\sim$ 28 Kev)

p = average energy loss per photon produced ($\sim$ 70 ev)

ε_1 = efficiency of light collection ($\sim$ .5)

ε_2 = quantum efficiency of photo cathode ($\sim$ .1)

G = photomultiplier gain ($\sim 5 \times 10^7$ at 2600 anode volts)

hence, $N \sim 100\ G$ electrons

and $V \sim 8$ volts.

An integral pulse height (PH) distribution is obtained by varying the input discriminator level of the counter, and by changing a variable attenuator in the pulse line (cf. Fig. A.6). This PH

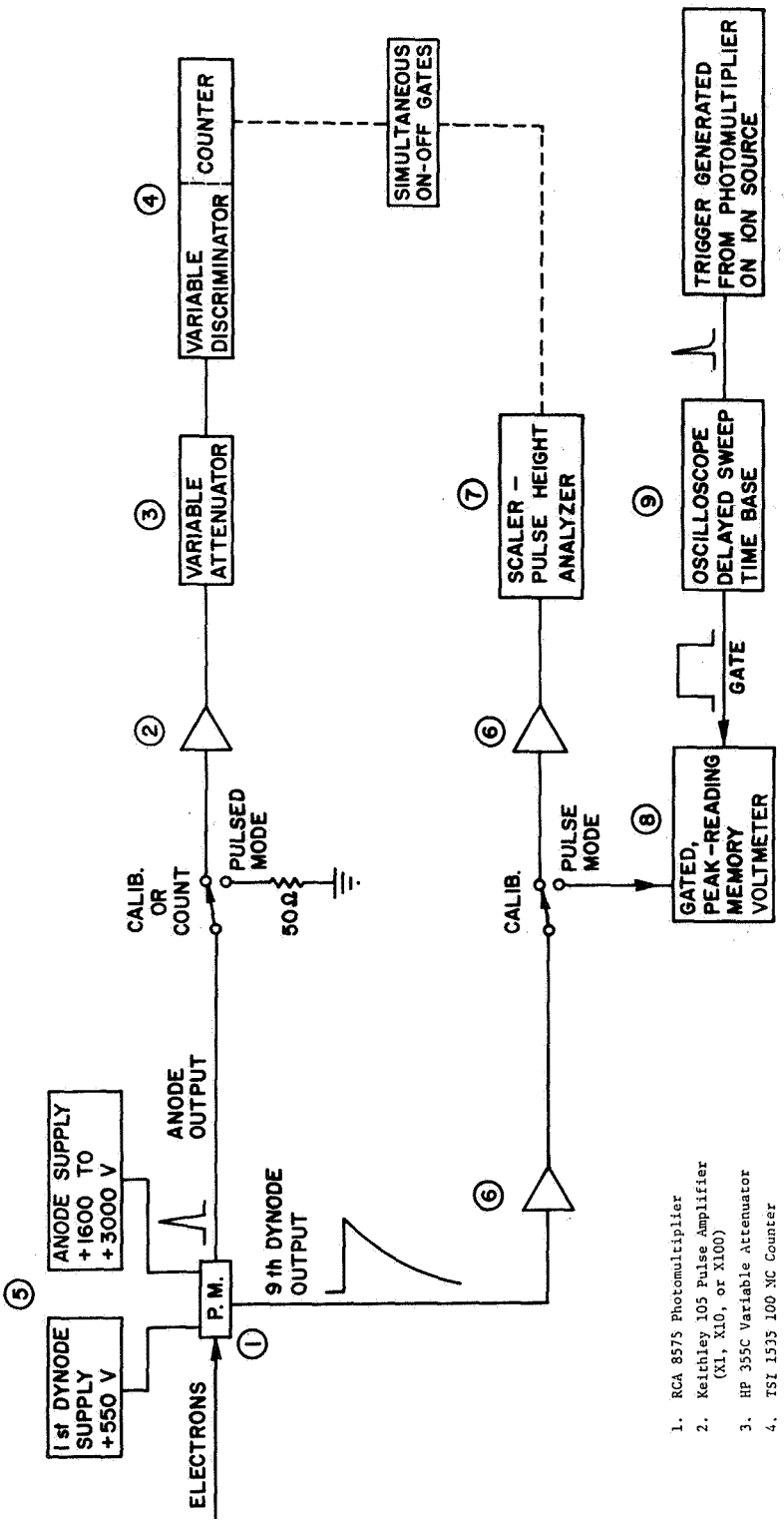

Fig. A.6. Block Diagram of Calibration System.

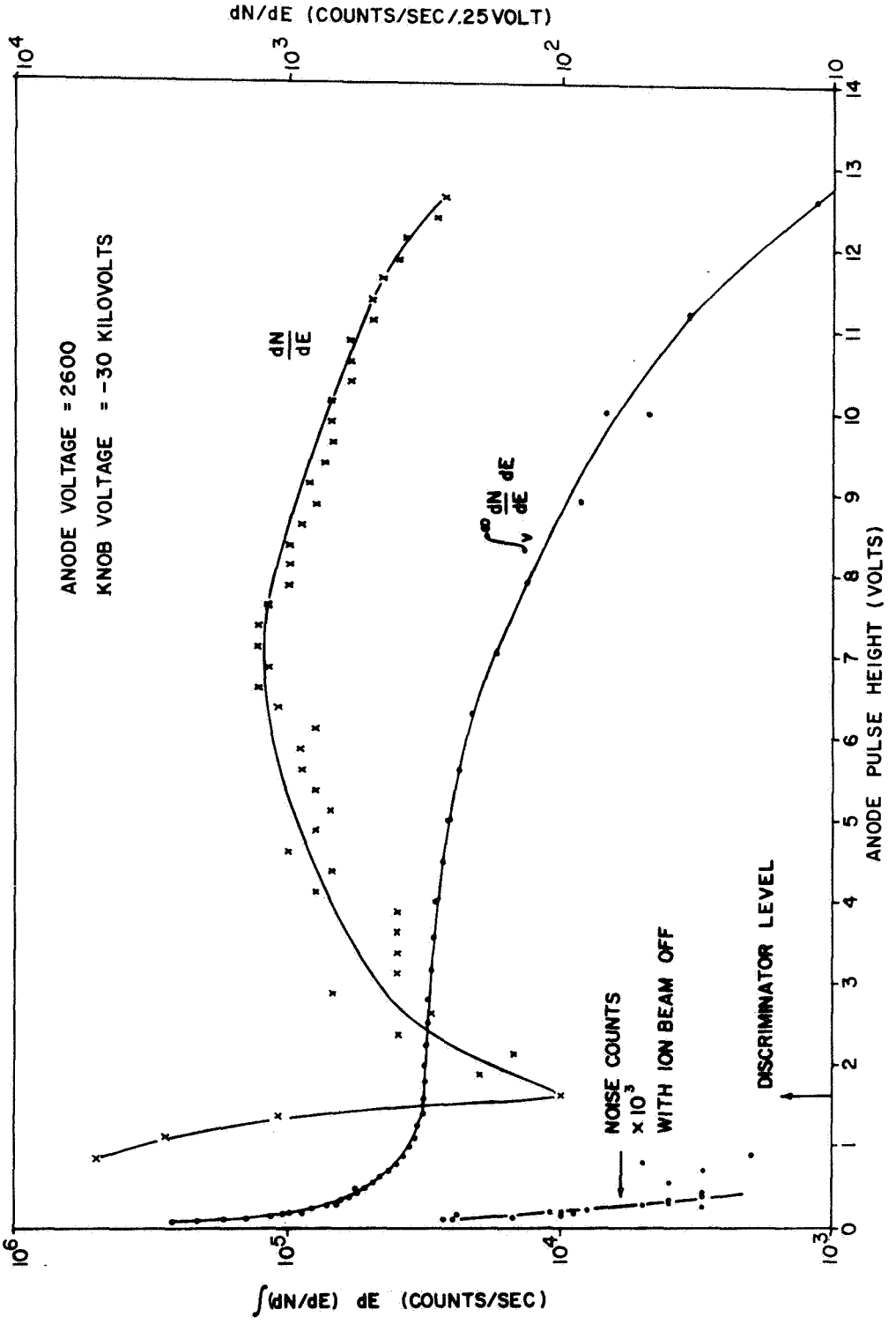

Fig. A.7. Integral and Differential Anode Pulse Height Distributions.

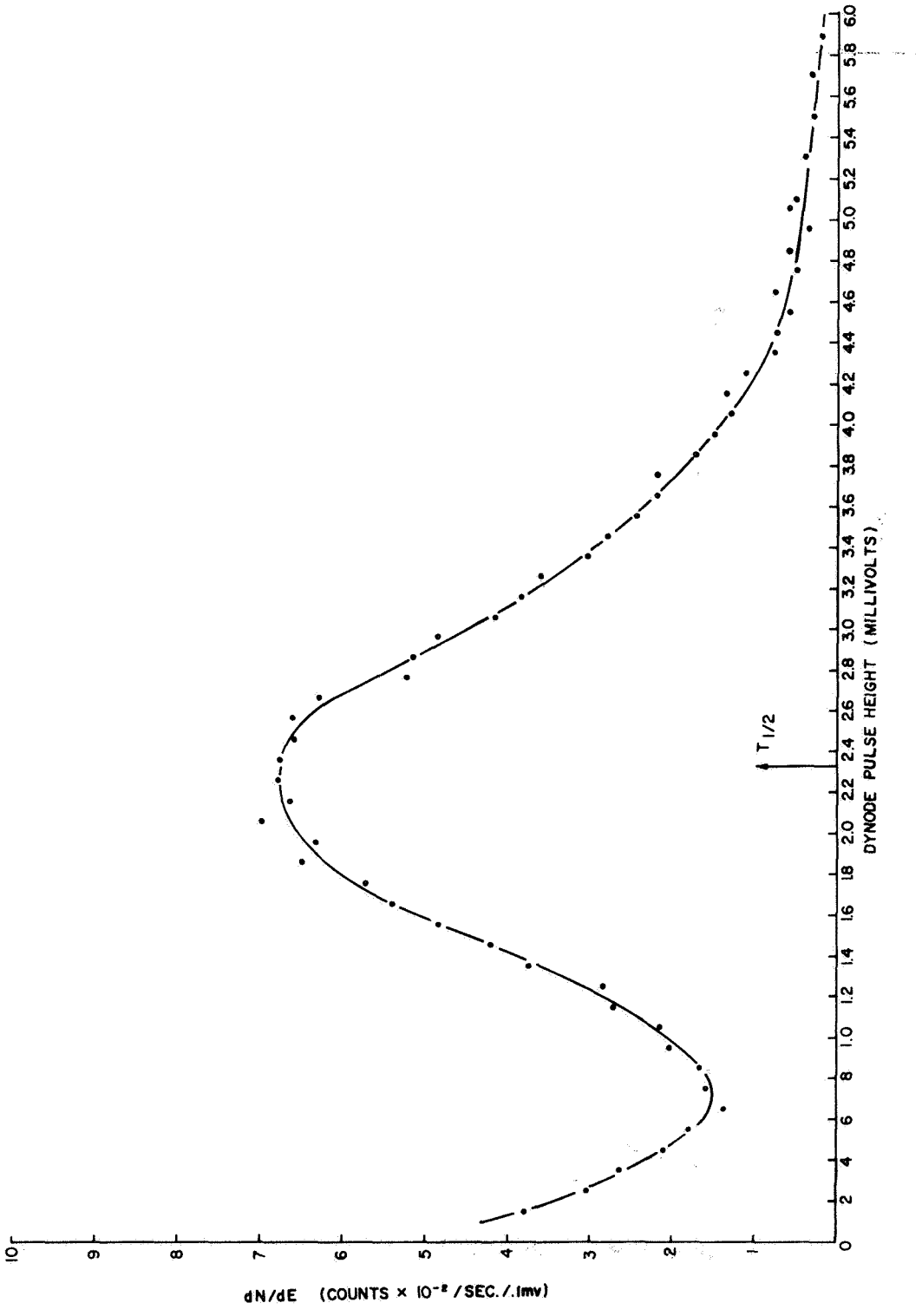

Fig. A.8. Differential Dynode Pulse Height Distribution.

distribution and its derivative are shown in Fig. A.7 and the appropriate discriminator level to be used in the counting mode is indicated.

The distribution of the ninth dynode pulse heights is obtained directly by using the PH analyzer in the dynode counter and is shown in Fig. A.8. The mean dynode PH ($T_{\frac{1}{2}}$) is only several millivolts, and 10^3 nearly simultaneous ions produce a single pulse of several volts.

5. Counting Efficiency and Noise

The secondary emission coefficient for ions is a slowly increasing function of their incident kinetic energy at energies greater than about 20 kilovolts and is of order 5 electrons per incident ion[62] on aluminum. Therefore, as the voltage on the aluminum knob is increased, more secondary electrons are produced per ion and the probability of an ion producing no secondary electrons is reduced. In turn, more electrons with greater energy produce more scintillation and a larger anode pulse. Hence, the counting efficiency should be a monotonically increasing function of the voltage on the knob.

A test of this assumption was made by directing a beam of ions into the detector and then measuring the counting rate as a function of the voltage on the knob. The anode discriminator level was set at the appropriate level to eliminate counts not due to ions. The results shown in Fig. A.9 demonstrate that the efficiency is approximately constant above 20 kilovolts. This test, and the

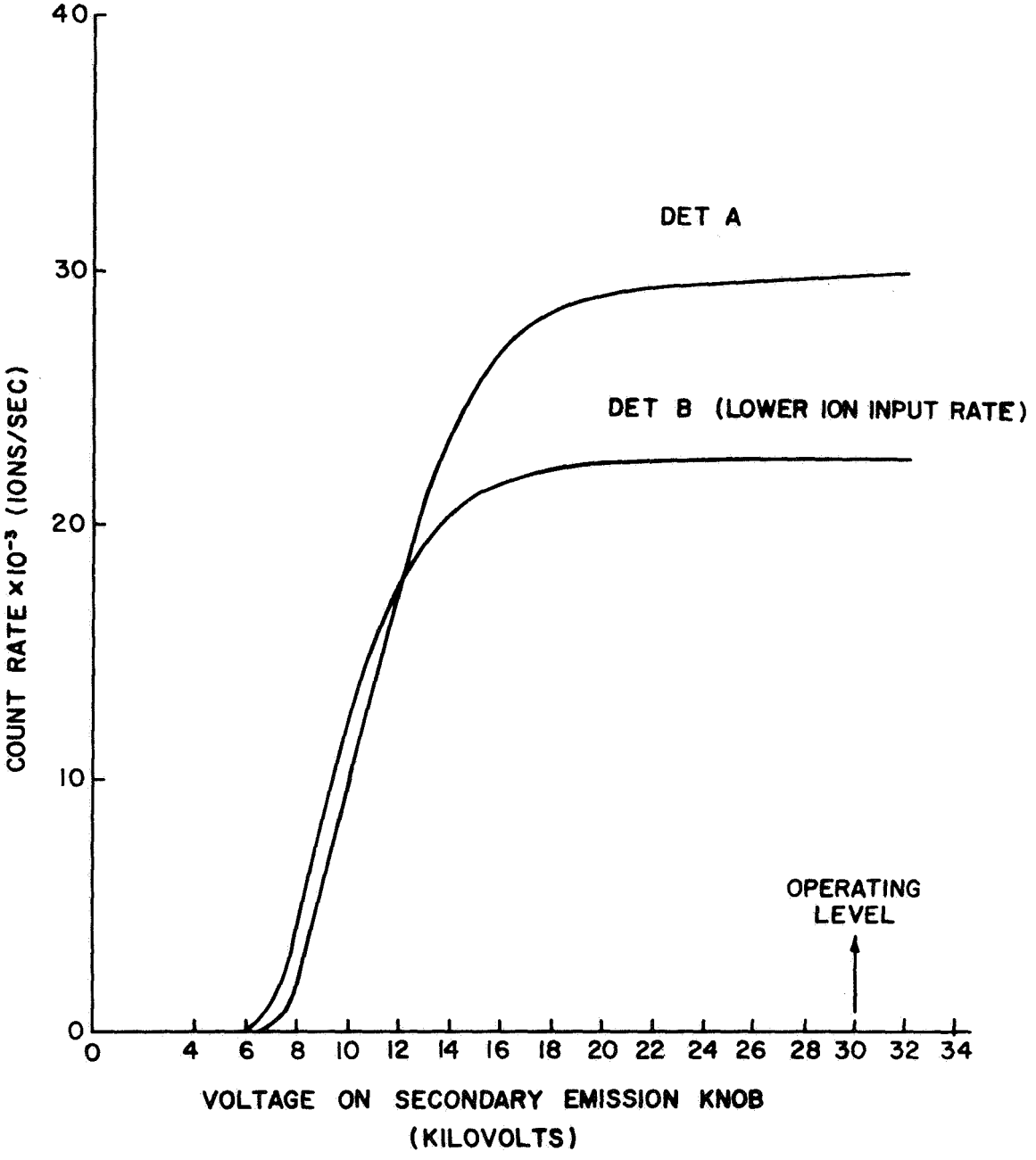

Fig. A.9. Demonstration of Monotonicity of Counting Efficiency as Function of Voltage on Knob.

pulse-height analysis of the previous section, indicate that the counting efficiency is probably very close to 100%. When an ion beam is switched from one detector to the other, the counting rates agree to about 2%.

The background noise due to electron emission or negative ion emission from the knob has been reduced to less than 1 count per second by a glow-discharge cleaning as suggested by Daly. Typical discharge conditions are: 250 microns pressure of dry nitrogen, negative polarity on the knob, and 1 milliamp. of discharge current for 15 minutes. Another source of noise seems to be the insulator between the HV knob and the surfaces at ground potential. Especially after the discharge process, this noise is very high but can be eliminated by returning the system briefly to atmospheric pressure. Also, to obtain a low noise level, this insulator should have a long surface path to ground, and not be in direct view of the photomultiplier. The overall noise rate is usally less than 3 per second.

6. Calibration of Dynode Signal

A calibration method has been devised to relate the voltage height of the integrated dynode signal caused by the nearly simultaneous arrival of a group of ions, to the number of ions. The calibration procedure is to measure the mean dynode pulse height per individual ion. The calibration is then absolute to the extent that the mean pulse height per ion is equal to the average pulse height per ion. The calibration has relative accuracy

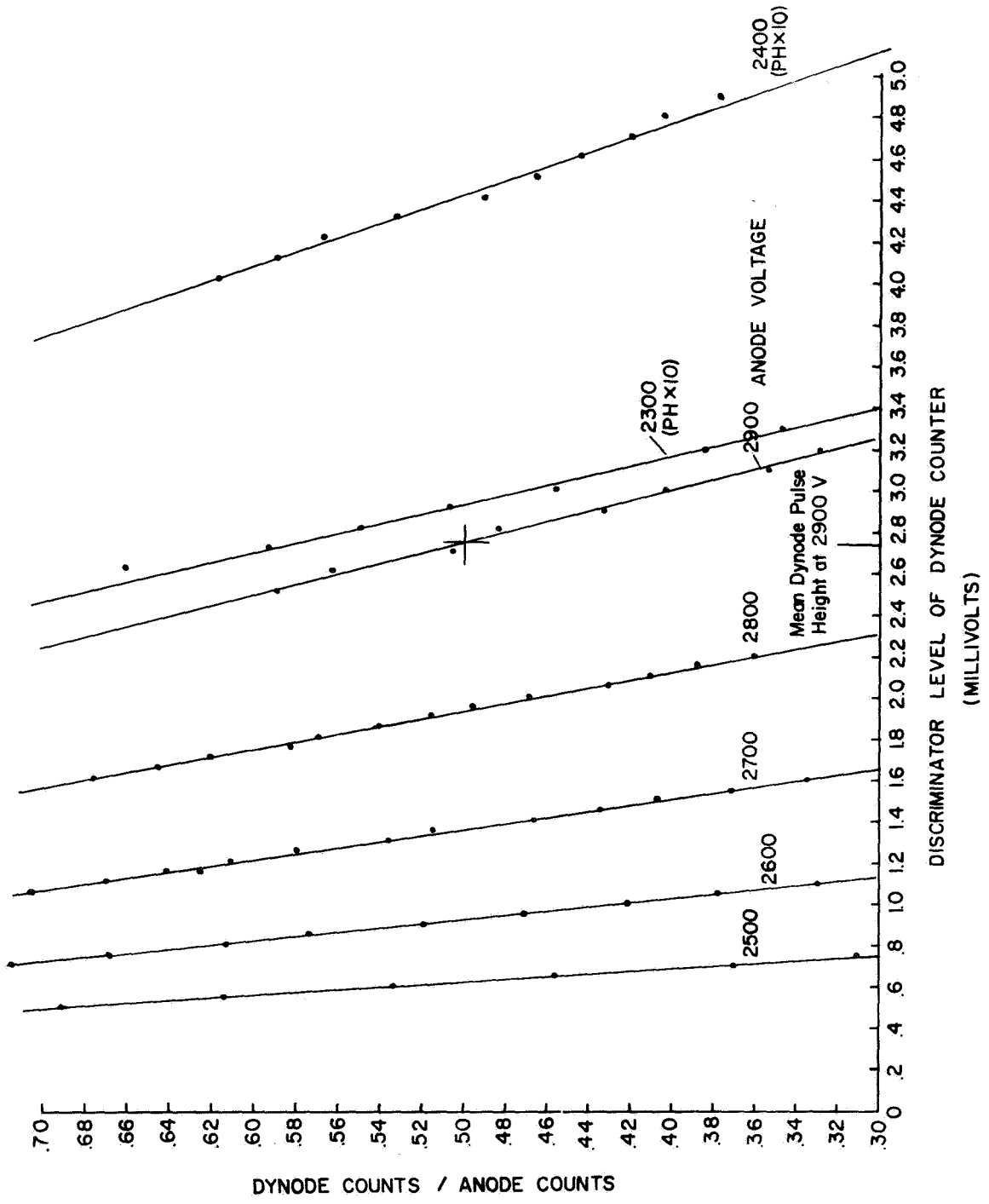

Fig. A.10. Ratio of Dynode to Anode Counting Rates Versus Discriminator Level of Dynode Counter. (Valve of mean dynode pulse height is shown.)

to the extent that the relation between the mean pulse height and the average pulse height is the same for each detector. It is assumed that the relation between the mean and the average is identical for all detectors,and hence the only relative inaccuracy lies in the determination of the mean dynode pulse height for each ion species. The dependence of the mean dynode pulse height on ion species is determined (cf. section A.7) to about ± 2%. Adding this to the error in the determination of the mean dynode pulse height for any species, the overall relative accuracy for two detectors accepting different ion species is then about ±7%. Also it is assumed that the average pulse height is equal to the mean pulse height within ±25%, hence the calibration is absolute to within ±32%. (Absolute cross section values in this experiment depend on the relative accuracy, ±7%).

A block diagram for the calibration is given in Fig. A.6. A beam of ions of selected species is directed into the detector at a low rate (1000/sec), so that the dynode pulses are due to individual ions. All the ions are counted on the anode counter, however the discriminator on the dynode counter is set so that 35% to 65% of the ions are counted. Fig. A.10 shows the ratio of dynode to anode counts versus the discriminator level of the dynode counter. The line through the points is nearly linear because the mean dynode PH is near the maximum of the PH distribution (cf. Fig. A.8). The mean dynode PH is defined as the discriminator level for which the ratio of dynode to anode counts is equal to 0.50.

In order to improve the accuracy of the calibration and

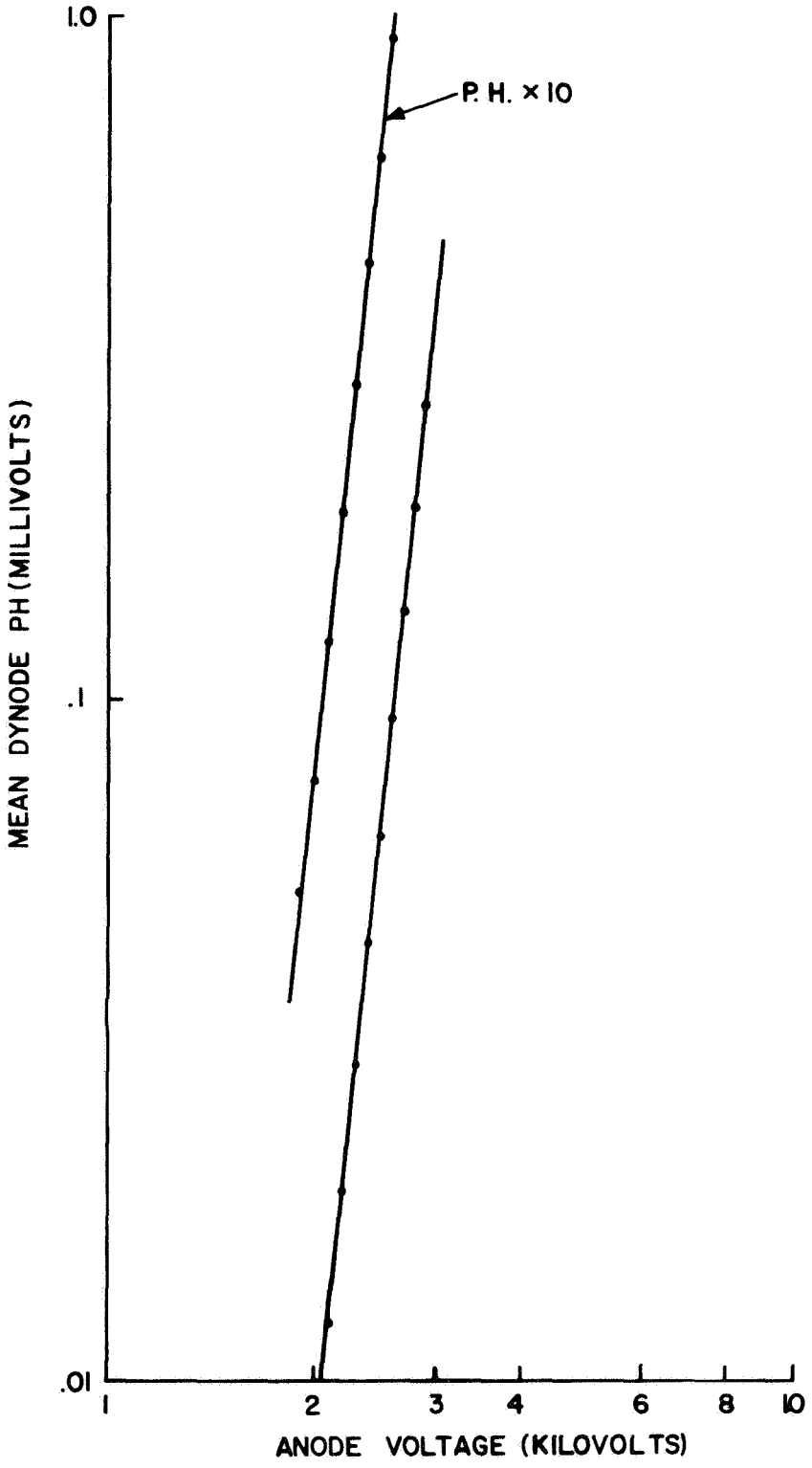

Fig. A.11. Mean Dynode Pulse Height versus Anode Voltage.

to permit operation at various gains of the photomultiplier tube, the calibration is done as a function of anode voltage. First the appropriate anode discriminator level is determined by a series of anode PH measurements. Both the anode discriminator level and the mean anode PH fit well to the curve

$$T = B \times V^{K} \quad , \tag{A.3}$$

where T is the voltage height, V is the anode voltage, B and K are constants, and K is approximately equal to 12.2. The dynode PH fits well to a curve of the same form with k approximately equal to 10. Each data point is then within several percent of the computed curve. The curve fittings are performed with a computer routine. The accuracy of the mean dynode PH, calculated from Eq. (A.3) for anode voltages between 1500 and 3000 volts, is estimated to be $\pm$5%. The range of the mean dynode PH typically extends from .005 millivolt/ion at 1500 anode volts to 4 millivolts/ion at 3000 anode volts, as shown in Fig. A.11.

For the dynode signal to remain linear, its height must be small compared to the interstage voltage of the tube. For example, at an anode voltage of 1500, 2×10^5 ions change the ninth dynode voltage by 1.9%. Therefore, 2×10^5 is approximately the maximum number of ions that will produce a linear signal at 1500 anode volts. With appropriate amplification, the range of measurement in the pulsed mode is therefore from 1 ion per pulse to approximately 2×10^5 ions per pulse.

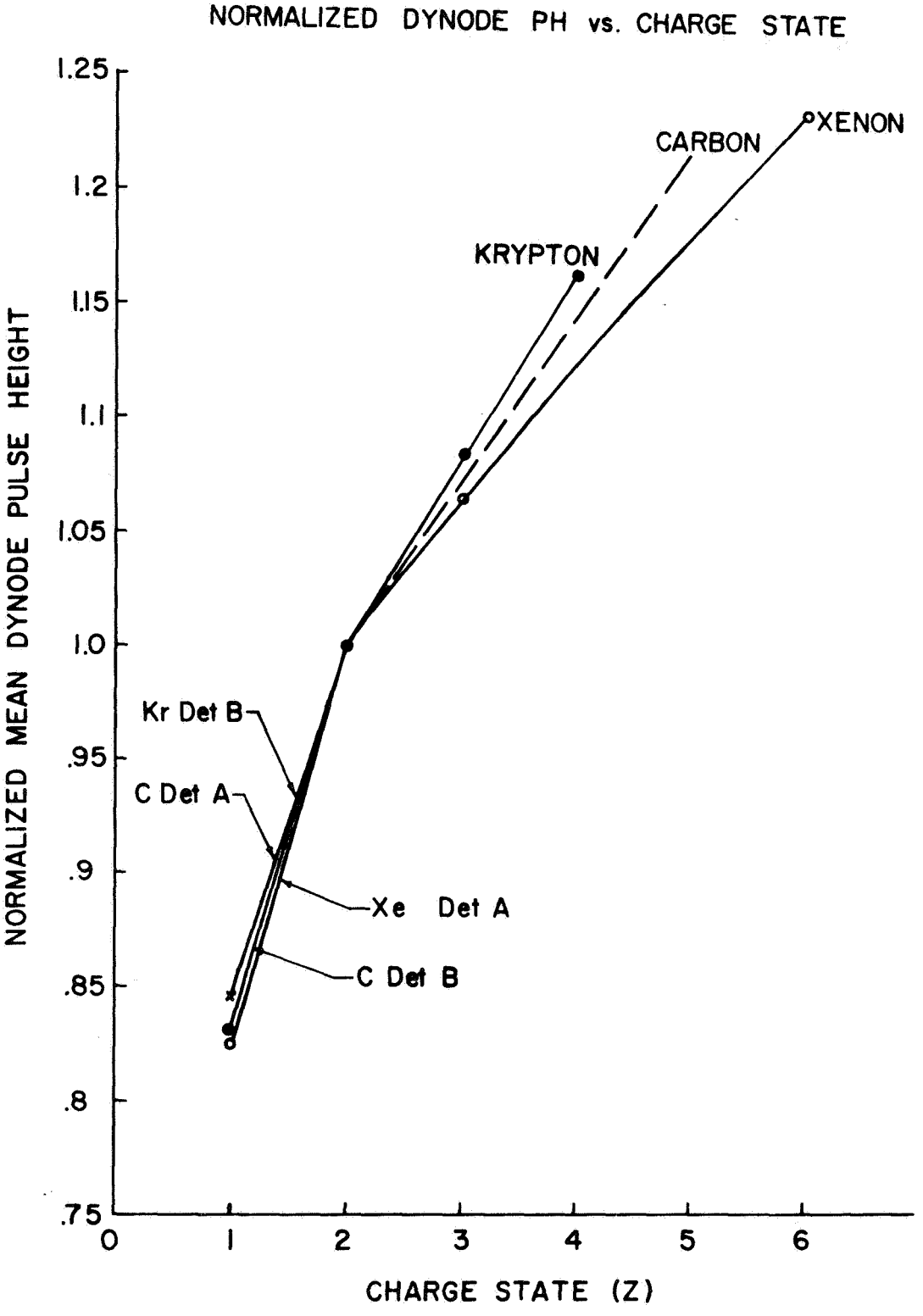

Fig. A.12. Mean Dynode Pulse Height versus Charge State.

7. Dependence of Pulse Height on Ion Species

The electron secondary emission coefficient is not the same for all incident ions, and therefore the PH is a function of the incident ion species. The mean dynode PH is calibrated for those ions that can be produced in an electron bombardment ion source, and this information is then extrapolated to other ions. The secondary emission is mainly due to the kinetic type of ejection and for a given energy per unit charge is primarily a function of ion mass, charge state, and, for molecular ions, the number of atoms per molecule[63].

For multiply-charged ions the incident kinetic energy is proportional to the charge (the incident kinetic energy is Z times 30 Kev). Therefore, the charge state has a large effect on the kinetic ejection. The variation of emission as a function of Z is approximately the same for the several elements measured, as expected. The mean dynode pulse heights for krypton up to $Z = 4$, Xenon to $Z = 6$, and carbon to $Z = 2$ are normalized at $Z = 2$ and plotted in Fig. A.12. In the present experiment the relative factor required is, for example, $PH(Z = 3)/PH(Z = 4) = .94$, since C^{4+} enters one detector and C^{3+} enters the other. The accuracy of this extrapolation is estimated to be $\pm 2\%$.

Data for the mean dynode PH of various ions relative to C^{2+} are given in Table A.1.

Table A.1

Ion	Relative Mean Pulse Height
C^+	.84
C^{2+}	1.00
Kr^{2+}	.88
Xe^{2+}	.98
H^+	.56
H_2^+	.72
HO^+	.98
H_2O^+	.98
N^+	.83
N^{2+}	1.01
N_2^+	1.05
O^+	.87
O^{2+}	1.02
O_2^+	1.11
CO_2^+	1.24
CO_2^{2+}	1.43

Appendix B

Ionization Potentials

Element	IP_1	IP_2	IP_3	IP_4	IP_5	$IP_1 + IP_2$
Carbon	11.27	24.38	47.88	64.49	392.1	
Helium	24.59	54.41				79.0
Neon	21.56	41.08	63.70	97.18	126.5	62.6
Argon	15.76	27.62	40.91	59.81	75.0	43.4
Krypton	14.00	24.57	36.95	(68)		38.6
Xenon	12.13	21.21	32.12	(46)		34.3
Hydrogen	13.60					
Beryllium	9.32	18.21	217.7			
Magnesium	7.65	15.03	80.13	109.3	141.3	

The values in this table are from Charlotte Moore's tabulation[64]. They have been converted to ev using the factor 8066.03 cm^{-1}/ev.

LIST OF FIGURES

Figure Page

LIST OF TABLES

REFERENCES

1. "Applications of Atomic Collision Physics to Other Fields," in The Physics of Electronic and Atomic Collisions: Invited Papers from Fifth Intern. Conf., L. M. Branscomb Ed., JILA, Univ. of Colorado (1968).

2. D. Rapp and W. E. Francis, J. Chem. Phys. 37, 2631(1962).

3. D. R. Bates and H. S. W. Massey, Phil. Mag. 45, 12(1954).

4. J. C. Y. Chen and K. W. Watson, Phys. Rev. 174, 152(1968).

5. C. Zener, Proc. Roy. Soc. A, 137, 696(1932).

6. W. Lichten, Phys. Rev. 131, 229(1962).

7. J. B. Hasted and A. R. Lee, Proc. Phys. Soc., 79, 702(1962).

8. G. F. Drukarev, Abst. from Fifth Intern. Conf. on Phys. of Electronic a. Atomic Collisions, p. 10 (Nauka, Leningrad, USSR, 1967).

9. N. F. Mott and H. S. W. Massey, The Theory of Atomic Collisions 3rd ed, p. 353, Oxford Clarendon Press (1965).

10. J. V. Neumann and E. Wigner, Phys. Z. 30, 467(1929).

11. E. C. G. Steuckelberg, Helv. Phys. Acta, 5, 369(1932).

12. L. Landau, Z. Phys. Sowjet, 2, 46(1932).

13. D. R. Bates, H. C. Johnson, and L. Stewart, Proc. Phys. Soc., 84, 517(1964).

14. J. B. Hasted, Physics of Atomic Collisions, Sec. 11.2 and 11.3, London Butterworths (1964).

15. I. P. Flaks and L. G. Filippenko, Sov. Phys. Tech. Phy. 4, 1005(1960).

16. H. B. Hasted and A. Y. J. Chong, Proc. Phys. Soc. 80, 441(1962).

17. G. N. Ogurtsov and I. P. Flaks, Sov. Phys. JETP 15, 502(1962).

18. J. B. Hasted and M. Hussain, Proc. Phys. Soc. 83, 911(1964).

19. D. R. Bates, Proc. Roy. Soc. A, 257, 141(1960), see also D. R. Bates in Atomic and Molecular Processes, ed. by D. R. Bates, Academic, New York (1962).

20. W. D. Ellison and S. Borowitz, Atomic Collision Processes, ed. by M. R. C. McDowell, North Holland-Amsterdam, p. 790 (1964).

21. Yu. P. Morduinov and O. B. Firsov, Sov. Phy. JETP 12, 301(1960).

22. C. A. Coulsen and K. Zelewski, Proc. Roy. Soc. A, 268, 437, (1962).

23. V. K. Bykhovskii and E. E. Nikitin, Sov. Phys. JETP 21, 1003(1965).

24. D. R. Bates and B. L. Moeseiwitsch, Proc. Phys. Soc. A, 67, 805(1954).

25. G. L. Moiseiwitsch, J. Atmos. Terr. Phys. 23, Supplement, Vol. 2, Meteors,ed. T. R. Kaiser (1955).

26. J. B. Hasted, A. R. Lee and M. Hussain, Atomic Collision Processes ed. by M. R. C. McDowell, North Holland-Amsterdam, p. 802(1964).

27. A. Dalgarno, Proc. Phy. Soc. A, 67, 1010(1954).

28. T. J. M. Boyd and B. L. Moiseiwitsch, Proc. Phys. Soc. A, 70, 809(1957).

29. D. R. Bates and J. T. Lewis, Proc. Phys. Soc. A, 68, 173(1955).

30. D. R. Bates and T. J. M. Boyd, Proc. Phys. Soc. A, 69, 910(1956).

31. J. B. Hasted and R. A. Smith, Proc. Roy. Soc. A, 235, 354(1955).

32. Yu. N. Demkov and I. V. Komarov, Sov. Phys. JETP 23, 189(1966).

33. B. M. Smirnov, Sov. Phys. JETP, 26, 812(1968).

34. J. C. Y. Chen and J. L. Peacher, Phys. Rev. 167, 30(1968).

35. L. M. Kishenevsky and E. S. Parilis, Abst. from Fifth Inter. Conf. on Phys. of Electronic and Atomic Collisions, p. 100 (Nauka, Leningrad, USSR, 1967).

36. J. B. Hasted, Physics of Atomic Collisions, Sec. 3.6, London Butterworths (1964).

37. K. W. Ehlers, J. D. Gow, L. Ruby, and J. M. Wilcox, Rev. Sci. Instr. 29, 614(1958).

38. H. Eubank and T. D. Wilkerson, Rev. Sci. Instr. 34, 12(1963).

39. H. J. Zwally, U. of Md. Tech. Note (in preparation).

40. J. Mattauch, Phys. Rev. 50, 617(1936).

41. Varian Associates, Palo Alto, Calif.

42. Millitorr Gauge, Varian Associates, Palo Alto, Calif.

43. L. G. Fillippenko, Sov. Phys. Tech. Phys 5, 52(1960).

44. MKS Instrument Inc., Burlington, Mass.

45. W. C. Lineberger, J. W. Hooper, E. W. McDaniel, Phys. Rev. 141, 151(1966).

46. S. K. Allison and M. Garcia-Munoz, in Atomic and Molecular Processes, ed. by D. R. Bates, Academic, New York (1962).

47. J. W. Stearns, K. H. Berkner, V. J. Honey, and R. V. Pyle, Phys. Rev. 166, 40(1968).

48. M. Fisz, Prob. Theory and Math. Statistics, John Wiley (1963).

49. Y. Beers, Theory of Error, Addison-Wesley (1957).

50. Micro Instrument Co., Gardena, Calif.

51. N. G. Utterback and T. Griffith Jr., Rev. Sc. Inst. 37, 866(1966).

52. D. W. Koopman, Phys. Rev. 154, 79(1967).

53. I. P. Flaks, G. N. Ogurtsov, and N. V. Fedorenko, Sov. Phys. JETP 14, 1027(1962).

54. G. D. Alan, D. K. Bohme, J. B. Hasted, P. P. Ong., Abst. from Fifth Intern. Conf. on Phys. of Electronic and Atomic Collisions, p. 100 (Nauka, Leningrad, USSR, 1967).

55. N. R. Daly, Rev. Sci. Instr. 31, 264(1960).

56. K. W. Ogilvie, N. McIlwraith, H. J. Zwally and T.D. Wilkerson, NASA Tech. Note, NASA Tn D-2111 (1964).

57. J. L. Young, J. Appl. Phys. 27, 1(1956).

58. F. T. Porter, M. S. Freedman, F. Wagner Jr. and I. S. Sherman, Nuc. Inst. and Methods 39, 35(1966).

59. Pilot Chemical Co., Watertown, Mass.

60. Dow Corning C-2-0057.

61. H. R. Krall, IEEE Trans. on Nuc. Sc., 39 (Feb. 1965).

62. H. C. Bourne Jr., R. W. Cloud, and J. G. Trump, J. of App. Phys. 26, 596(1955).

63. M. Kaminsky, Atomic and Ionic Impact Phenomena on Metal Surfaces, Academic Press (1965).

64. Charlotte E. Moore, Circular of NBS 467, (1949 and 1952), U.S. GPO, Wash. D. C.

65. Omnitab , NBS Handbook 101, U.S. GPO, Wash. D. C.